Improvements to Solar Thermoelectric Generators through Device Design

by

Lee A. Weinstein

Submitted to the Department of Mechanical Engineering
in partial fulfillment of the requirements for the degree of

Master of Science in Mechanical Engineering

at the

MASSACHUSETTS INSTITUTE OF TECHNOLOGY

September 2013

Author .....
Department of Mechanical Engineering
August 9, 2013

Certified by ....
.....
Gang Chen
Carl Richard Soderberg Professor of Power Engineering
Thesis Supervisor

Accepted by .....
Prof. David E. Hardt
Chairman, Committee for Graduate Students

Improvements to Solar Thermoelectric Generators through Device Design

by

Lee A. Weinstein

Submitted to the Department of Mechanical Engineering
on August 9, 2013, in partial fulfillment of the
requirements for the degree of
Master of Science in Mechanical Engineering

Abstract

A solar thermoelectric generator (STEG) is a device which converts sunlight into electricity through the thermoelectric effect. A STEG is nominally formed when a thermoelectric generator (TEG), a type of solid state heat engine, is placed between a solar absorber and a heat sink. When the solar absorber is illuminated by sunlight, it heats up and the TEG is subjected to a temperature gradient. Heat flows through the TEG, some of which is converted to electricity. Recent advancements have improved STEG efficiency considerably, however more work is required before STEGs will be able to compete commercially with other solar to electricity conversion technologies. This thesis explores two device level improvements to STEG systems. First, thin-film STEGs are explored as a method to potentially reduce the manufacturing costs of STEG systems. It is shown through modeling that thin-film STEGs have only a slight degradation in performance compared to bulk STEGs when identical materials properties are used. Two parameters are found which can guide device design for thin-film STEGs regardless of system size. Second, an optical cavity is investigated which can improve opto-thermal efficiency for STEGs or any other solar-thermal system. The cavity improves performance by specularly reflecting radiation from the absorber back to itself, reducing radiative losses. It is shown through modeling and with some preliminary experimental results that such a cavity has the potential to significantly improve the opto-thermal efficiency of solar-thermal systems and operate efficiently at high absorber temperatures without the use of extremely high optical concentration ratios.

Thesis Supervisor: Gang Chen
Title: Carl Richard Soderberg Professor of Power Engineering

Acknowledgements

There is no question that my work at MIT thus far which has culminated in this thesis, significant or insignificant as it may be, would not have been possible without the support of many other individuals. I am greatly indebted to Prof. Gang Chen for his guidance and am extremely thankful that I had the good fortune to be accepted into his group back when I didn't even know what a phonon was (not that I could say with confidence that I know what a phonon is now). I would also like to thank the NanoEngineering group as a whole, I am lucky to be able to work with such a welcoming, caring and helpful group of people. I am especially grateful to Ken McEnaney and Dan Kraemer, without whom I'm not sure I would know anything about STEGs or heat transfer measurements. I hope your willingness to drop your own work in order to assist me has not delayed your graduations by any significant amount of time. I would also like to acknowledge Dr. Michael Wing, Prof. Oliver O'Reilly and Prof. Paul Wright, without whose mentorship I might not have the good fortune to be at MIT today.

I must express gratitude to my parents and my sister, the most compassionate, caring, understanding people I know. I am constantly reminded of how lucky I am to have them as family, and I hope they know that all of my accomplishments are thanks to their support throughout the years. Finally, I would like to thank the friends who have helped keep me sane over the years, especially my friends in Boston who have been with me for the occasionally trying times at MIT. I would thank them all by name, but I think this thesis is long enough already. Instead, I will just say that I am glad to have met all of you; you have made the last two years a beautiful experience.

Contents

List of Figures

List of Tables

Chapter 1 Introduction

The human population is growing rapidly, and populous nations are quickly becoming more developed. Society's demand for electrical power is thus rising sharply, and maintaining our current fossil fuel dominated energy consumption pattern will lead to two large problems: global climate change [1] and depletion of fossil fuel resources [2]. Diversification of our energy portfolio is likely one of the greatest challenges we will face in the coming years, as most renewable sources have trouble competing with non-renewables economically [3].

1.1 Solar energy

Solar energy is the most promising source for renewable energy in terms of the sheer amount available. The amount of solar power that is incident on the surface of Earth is about four orders of magnitude greater than current global total energy demand [4]. Covering a sufficient surface area of the Earth to satisfy global demand would be no easy feat, but given the abundance of the supply of solar energy, investigating solar technologies is an important task as solar energy could potentially provide power sufficient for human demand. There are a number of different ways to convert solar energy to electricity. The most prevalent method used currently is photovoltaic cells [5, 6].

Another broad category of solar energy conversion technologies is solar-thermal systems. These systems heat up a solar receiver with sunlight, and then use that heat to generate electricity [7]. The specific physics involved in generating electricity can vary broadly within these systems, but they all share the hot solar absorber feature. Examples of such systems include using a traditional heat engine [8], solar thermoelectric generator (STEG) [9], a

thermophotovoltaic conversion system [10, 11], or thermionic generator [12]. This thesis focuses on solar thermoelectric generators (STEGs).

1.2 Thermoelectric effects

A STEG is a solar-thermal energy conversion device which uses a thermoelectric (TE) generator to convert heat to electricity. Before understanding the operation of a STEG, specifically how a TE generator converts heat to electricity, one must have some knowledge of the thermoelectric effects. There are three separate thermodynamically reversible thermoelectric effects: the Seebeck effect, the Peltier effect and the Thomson effect [13].

The Seebeck effect, discovered in 1821 by Thomas Johann Seebeck, describes the electric field resulting from a temperature gradient across a thermoelectric material. This occurs because the majority carriers (electrons for n-type materials and holes for p-type materials) in the heated part of the material have more energy, and thus diffuse away from the hot side towards the cold side. As majority carriers diffuse to the cold side, an internal electric field forms due to the higher concentration of majority carriers on the cold side. The diffusion of majority carriers away from the hot side is balanced by this electric field, and the voltage drop across the material is called the Seebeck voltage. Figure 1.1 shows the Seebeck effect in an n-type and p-type material.

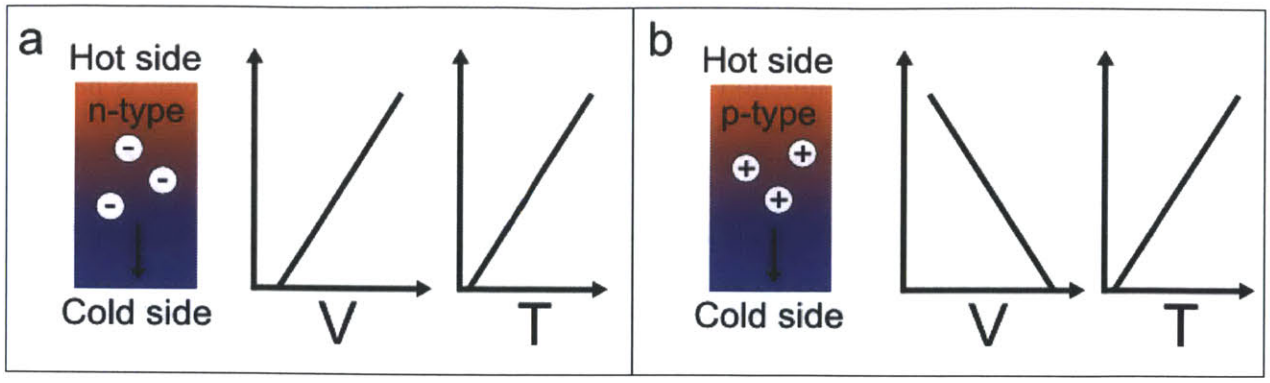

Figure 1.1 The Seebeck effect in a) an n-type material and b) a p-type material. Higher energy majority carriers diffuse from the hot to cold side of the material until this diffusion is balanced by the newly formed electric field. Voltage (V) and temperature (T) are plotted as a function of position within the material

For a thermoelectric material with Seebeck coefficient S (a material property with units volts per Kelvin, typically in the range of hundreds of microvolts per Kelvin for a good thermoelectric material) subjected to a temperature difference ΔT, the voltage drop ΔV across the thermoelectric material (with no current flowing through it) is given by the simple relationship:

$$\Delta V = -S\Delta T \tag{1.1}$$

The reason for the minus sign in Eq. (1.1) is that by convention n-type materials are typically assigned negative Seebeck coefficients while p-type materials are typically assigned positive Seebeck coefficients. This is reflected in the behavior of n-type and p-type thermoelectric materials as shown in Fig. 1.1. The value of a material's Seebeck coefficient depends on the asymmetry of electron transport (e.g., due to slope in the electron density of states) near the Fermi level of the material.

The Peltier effect, discovered by Jean Charles Athanase Peltier in 1834, describes the heat generated or removed at the junction of two dissimilar conductors when current is passed through it. In different materials the heat carried per charge varies, and the heat carried per charge is given by the Peltier coefficient Π (generally if Π is positive, it is the heat carried per hole and if Π is negative, then |Π| is the heat carried per electron). Charge conservation dictates that charge flowing into a junction must be equal to charge flowing out of a junction. If current flows through a junction of materials with different values of Π, a Peltier heat must be generated at the junction in order to satisfy conservation of energy (i.e., if the charge carriers flowing into a junction carry more heat than the charge carriers flowing out of that junction, the junction will heat up). The Peltier effect is illustrated in Fig. 1.2.

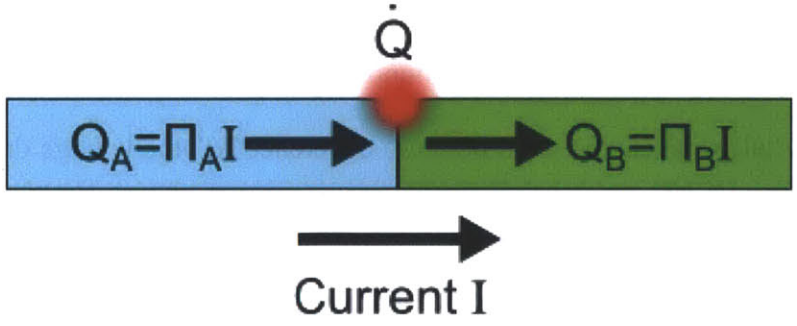

Figure 1.2 The Peltier effect. Heat carried by the current is given by ΠI. If Π is not equal across the interface, a Peltier heat $\dot{Q}$ is generated such that energy is conserved at the junction.

The Peltier heat $\dot{Q}$ generated at the junction between conductors A and B is given by

$$\dot{Q} = (\Pi_A - \Pi_B)I \tag{1.2}$$

where Π_A and Π_B are the Peltier coefficients of materials A and B, respectively, and I is the electrical current flowing from A to B. Note that heat can be removed (i.e., $\dot{Q}$ can be negative) if

the quantity $\Pi_A - \Pi_B$ is negative, or if current is pumped from B to A while $\Pi_A - \Pi_B$ is positive. The Kelvin relations, which were discovered by Lord Kelvin in 1854, define the relationships between different thermoelectric coefficients. The Seebeck coefficient and Peltier coefficients are related in a material by:

$$\Pi = TS \tag{1.3}$$

and this relationship follows from the Onsager relations [14]. Thus the Peltier heat generated can be written equivalently:

$$\dot{Q} = T(S_A - S_B)I \tag{1.4}$$

The Thomson effect arises due to the fact that for many materials, thermoelectric properties vary with material temperature, and was discovered by Lord Kelvin in 1851. When the material properties vary with temperature in a thermoelectric material which has current being passed through it, the Peltier effect is occurring all through the material, due to the temperature gradient creating junctions of "dissimilar conductors" within the material. This continuous Peltier effect resulting in additional volumetric cooling or heating along the material is called the Thomson effect. The equation describing the Thomson effect thus naturally follows from the equation for the Peltier effect. In considering the Thomson effect, a volumetric heat generation or cooling rate $\dot{q}$ is given by

$$\dot{q} = -K\vec{J} \cdot \nabla T \tag{1.5}$$

where K is the Thomson coefficient, $\vec{J}$ is the current density, and ∇T is the temperature gradient. The relationship between Thomson coefficient and Seebeck coefficient is:

$$\mathrm{K} = T\frac{dS}{dT} \tag{1.6}$$

so the equation for volumetric heating given by the Thomson effect can be rewritten:

$$\dot{q} = -T\frac{dS}{dT}\vec{J}\cdot\nabla T \tag{1.7}$$

With knowledge of the thermoelectric effects, one can use TE materials to build useful devices. Consider the case where a pair of n-type and p-type TE legs is connected electrically in series but thermally in parallel. If this thermoelectric pair is placed between a heat source and heat sink and an electrical load is attached, current will pass through the load and the TE pair acts as a heat engine (Fig. 1.3a). This device is the previously mentioned TE generator. If current is pushed through the pair, heat will be absorbed from one side of the pair and rejected at the other, so the pair acts as a heat pump (Fig 1.3b).

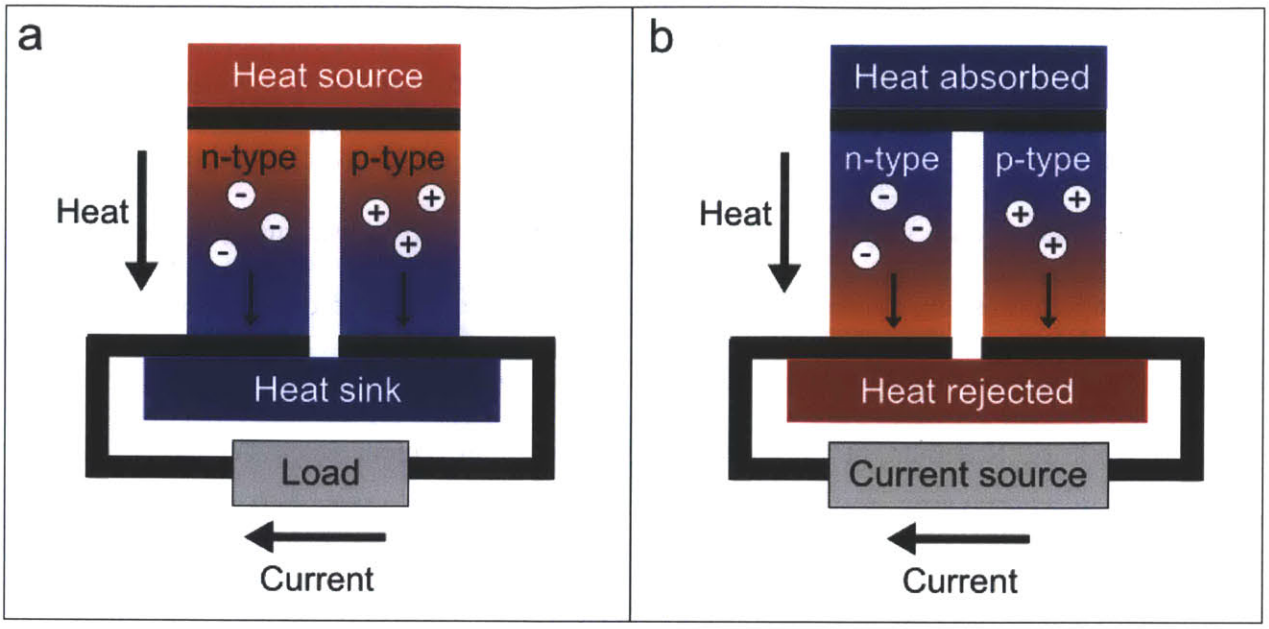

Figure 1.3 Operation of TE devices: a) A p-n pair of TE legs operating as a heat engine (TE generator) and b) A p-n pair of TE legs operating as a heat pump.

1.3 Solar Thermoelectric Generators (STEGs)

A STEG is a device which uses sunlight and thermoelectric materials to generate electricity [9]. The idea is very old [15], although it has not been until recent advances that STEGs have become an exciting technology with reasonable potential to offset demand for fossil fuels [16, 17]. At the simplest level, a STEG needs only three elements: a solar absorber, a thermoelectric generator (TEG), and a heat sink. The STEG is formed by placing the TEG between the solar absorber and the heat sink. When the solar absorber is illuminated, it absorbs sunlight which causes an increase in temperature. The side of the TEG attached to the absorber heats up, while the heat sink side stays cold. This subjects the TEG to a temperature gradient, and subsequently a voltage gradient is developed. If the TEG is connected to a load, current can run and thus electricity is generated from sunlight.

STEGs were investigated by Maria Telkes in the 1950s, and efficiencies of 0.63% and 3.35% were observed for the cases without optical concentration and with a concentrating lens (50x concentration ratio), respectively [9]. More experimental work has followed, however little progress was made until very recent developments. Even with newer materials and higher operating temperatures, experiments failed to result in a significant improvement over the work of Telkes, despite modeling efforts showing that improvement was possible [18–20]. It was not until the work of Kraemer, et al. that a significant improvement over Telkes' work was demonstrated experimentally [16].

The STEGs used by Kraemer, et al. have a few additional components which are responsible for their greatly improved performance. First, they are kept in an evacuated enclosure. While there are small reflective losses when the sunlight is transmitted through the glass (or whatever transparent material is used) enclosure, this eliminates convective heat losses from the absorber and TEG. Modern solar absorbers also use wavelength selective surfaces, which are highly absorptive in the solar spectrum, but have low emittance in the infrared spectrum. This reduces radiative losses from the absorber. Finally, high performing nano-structured thermoelectric materials can be used for the TEG. Having effective TE materials is always important for the performance of a TEG. A simple diagram of a STEG is shown in Figure 1.4.

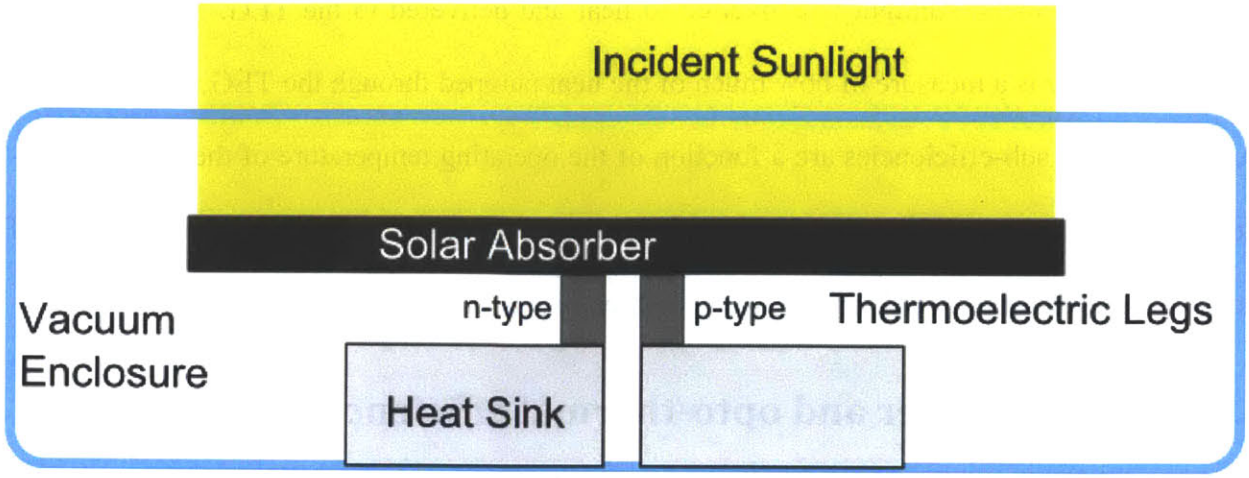

Figure 1.4 Diagram of STEG: TEG (pair of n-type and p-type thermoelectric legs) sandwiched between a solar absorber and heat sink within a vacuum enclosure

These improvements have allowed an observed efficiency of 4.6% under AM1.5G illumination without any optical concentration [16]. While this represents a huge advancement from previous experimental results, further improvement will be needed before STEGs can compete with other solar energy conversion technologies commercially. Current approaches to improve STEG performance mainly focus on improvements to thermoelectric materials (which will be discussed further in section 1.5) and the use of higher optical concentration [17, 21, 22]. In this thesis, a different approach is used, and modifications in device design are explored which offer potential performance improvements or manufacturing cost reductions. Improvements on all of these fronts will be needed in order for STEGs to be able to compete commercially with other energy conversion technologies.

When analyzing a STEG, the primary figure of merit is efficiency. Efficiency in this context is defined by electrical energy output divided by a given solar insolation incident on the device. In analyzing STEGs, this efficiency can be divided into a product of two sub-efficiencies: opto-thermal efficiency and thermoelectric device efficiency [23]. Opto-thermal efficiency is a

measure of how much sunlight is converted to heat and delivered to the TEG. Thermoelectric device efficiency is a measure of how much of the heat pumped through the TEG is converted to electricity. Both sub-efficiencies are a function of the operating temperature of the STEG. Opto-thermal efficiency depends on the solar absorber, and TE efficiency depends on the properties of the material used for the TEG, both of which will be discussed in depth below.

1.4 Solar absorber and opto-thermal efficiency

The first stage of a successful STEG is an effective way to convert sunlight into heat. The figure of merit here is opto-thermal efficiency. As stated previously, opto-thermal efficiency is the ratio of heat delivered to the TEG to solar power incident on the device. For a high opto-thermal efficiency, the device should absorb as much of the incident sunlight as possible, and avoid thermal losses (i.e. heat that goes anywhere besides the TEG). For the STEG setup described earlier, a wavelength selective surface in an evacuated transparent enclosure, calculating opto-thermal efficiency is relatively simple. There are only two large sources of loss: solar insolation incident on the device that fails to be absorbed by the selective surface, and radiative losses from the selective surface while it is at its operating temperature. Thus, opto-thermal efficiency η_{ot} can be given by

$$\eta_{ot} = \frac{CG\alpha\tau - \epsilon\sigma(T_H^4 - T_A^4)}{CG} \tag{1.8}$$

where C is the optical concentration ratio of sunlight striking the absorber (taken as unity, i.e., non-concentrated light, for chapters 1 and 2 of this thesis), G is the solar insolation incident on the device, α is the absorptance of the selective surface in the solar spectrum, τ is the transmittance of the enclosure in the solar spectrum (and can include the transmittance of the

concentrating optics in the case where concentration is used), ϵ is the emittance of the selective surface in the infrared spectrum, σ is the Stefan-Boltzmann constant, T_H is the operating hot-side temperature of the STEG, and T_A is the ambient temperature. Note that the units of each of the terms in this equation are watts per square meter, as the area of the device (assumed to be the same as the area of the selective surface) is common to each term. Also note that this treatment assumes that the absorber is isothermal at T_H, and each point on the surface radiates energy away with the same intensity.

A more complicated treatment might consider reflections and radiation exchange between the absorber and the enclosure surface, but as a first order approximation these contributions can be ignored, since the enclosure will typically be highly absorptive in the spectrum that the absorber emits. In cases with very high absorber temperatures such that the enclosure is no longer close to ambient temperature (such cases are not explored in this thesis) the model would need to be updated in order to reflect this, otherwise efficiency would be underestimated. A more sizeable loss comes from back-side losses from the absorber, that is: radiative losses directly from the back side of the absorber to the heat sink. In the worst case, this would double the radiative losses, as it provides double the area from which to radiate heat away, but this effect can be minimized through device design. For modeling purposes, this can be dealt with by replacing emittance ϵ with effective emittance ϵ^* where $\epsilon^* > \epsilon$ and takes into account back side losses.

It is perhaps easier to inspect equation (1.8) if it is rearranged as

$$\eta_{ot} = \alpha\tau - \frac{\epsilon\sigma(T_H^4 - T_A^4)}{CG} \tag{1.9}$$

Examining equation (1.9) one can see that the first mode of loss (insolation that fails to be absorbed) is treated in the first term, where absorptances and transmittances less than one will have a starting efficiency below unity. The second mode of loss (radiation from the absorber) is treated in the second term of equation (1.9) , as radiation given by the Stefan-Boltzmann law will be lost to the surroundings [24]. It is clear in selecting materials for a device, in order to maximize η_{ot}, one should maximize absorptance and transmittance, while minimizing emittance. Lowering hot side temperature will also improve opto-thermal efficiency, but this may have negative effects on overall performance, so selecting an operational hot-side temperature requires consideration of the device as a whole.

Maximizing transmittance is conceptually straightforward. Here an optically transparent material should be used for the vacuum enclosure which ideally has minimum reflectance at the interface between the material and air. If glass is used as the material a transmittance above 0.9 is achievable [25], and using anti-reflective coatings can push transmittance above 0.95 [26, 27]. Since unity is the maximum possible transmittance, there is not substantial room for improvement of opto-thermal efficiency via materials better than glass with anti-reflective coatings.

Maximizing absorptance while minimizing emittance is conceptually more complex due to Kirchhoff's law of thermal radiation which states that absorptance and emittance must be equal for a given surface at a specific temperature when considering a specific wavelength and direction [28]:

$$\alpha'_\lambda = \epsilon'_\lambda \tag{1.10}$$

Here λ denotes a spectral property and the apostrophe denotes a directional property. These distinctions are important as some materials will have very different radiative properties at different wavelengths or directions. This law can be derived from a thought experiment of a body inside a black cavity. Surfaces that could violate this law would be able to violate the second law of thermodynamics [28]. At first glance, Kirchoff's law might make it seem like it is impossible to have a surface with both high absorptance and low emittance, since they must be equal. However using clever manipulation of spectrally or directionally specific properties, the effective absorptance can be high while the effective emittance is low for solar-thermal applications. Directionally selective surfaces [29, 30] have not been investigated as thoroughly at this point, and will be further addressed in chapter 3.

Spectrally selective surfaces are effective for solar-thermal applications due to the difference in the spectrum of solar radiation and infrared radiation. This can be seen quickly from Wien's displacement law [28]:

$$\lambda_{max} T = 2898\, \mu m\, K \tag{1.11}$$

where T is the temperature of a blackbody, and λ_{max} is the peak wavelength emitted by that body. Wien's displacement law tells us that the sun ($T_{sun} \approx 5800\, K$) emits a peak radiation with wavelength of about 500 nm (green light), while a solar absorber ($T_{abs} \approx 600\, K$) emits a peak radiation with wavelength near 5 μm. These radiation peaks are separated by an order of magnitude, so if a surface absorbs radiation around 500 nm while reflecting radiation around 5 μm, it will achieve our desired properties of high solar absorption and low infrared emission. If

we focus on spectral selectivity and assume a surface is Lambertian (it is not directionally selective) the total hemispherical emissivity can be calculated by [28]

$$\epsilon(T) = \frac{1}{E_b(T)} \int_0^\infty \epsilon_\lambda(T,\lambda) E_{b\lambda}(T,\lambda) d\lambda \tag{1.12}$$

where E_b is the blackbody emissive power (energy emitted by a blackbody surface per time per surface area) and $E_{b\lambda}$ is the spectral blackbody emissive power (energy emitted by a blackbody surface per time per surface area per wavelength). From inspection, we can see that total hemispherical emissivity is weighted by the spectral emissivity at wavelengths that are relevant at the given surface temperature. Therefore, to get a more detailed picture of exactly how well a surface will perform, we need to consider not just the peak radiation for bodies at a given temperature, but also the distribution as a whole. This distribution is given by Planck's Law [28]:

$$E_{b\lambda}(T,\lambda) = \frac{2\pi hc^2}{\lambda^5 (e^{hc/\lambda k_B T} - 1)} \tag{1.13}$$

where $E_{b\lambda}$ is the spectral blackbody emissive power, T is the temperature of the body, λ is the emitted wavelength of interest, h is Planck's constant, c is the speed of light in the surrounding medium, and k_B is Boltzmann's constant. Two plots of spectral emissive power versus wavelength are shown in Fig. 1.5 for T_{sun} and a typical absorber temperature, with spectral emissive power normalized.

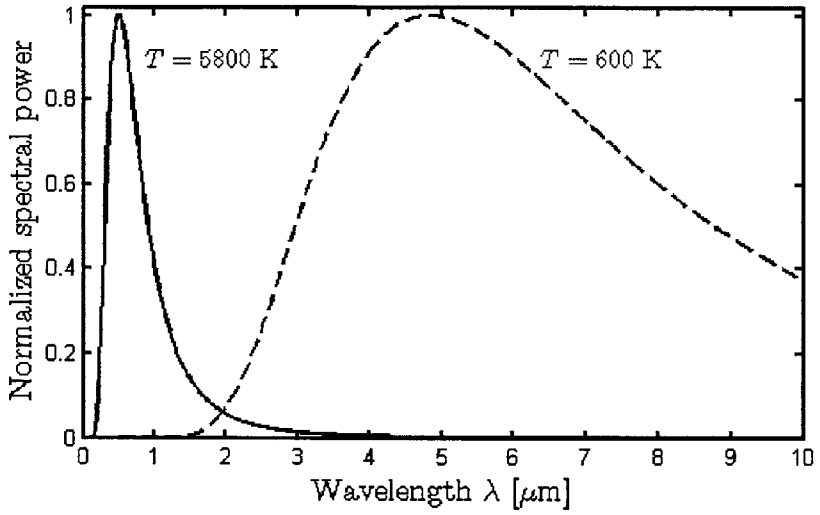

Figure 1.5 Normalized power spectra: solid blue curve for T = 5800 K, dashed green curve for T = 600 K

Since the two curves have a portion of overlap (near 2 μm for typical absorber temperatures, as seen in Fig. 1.5), we cannot design a material that will absorb the entire solar spectrum without emitting some of the infrared spectrum. The ideal surface would have a sharp cutoff wavelength, with perfect absorption at shorter wavelengths and perfect reflection at longer wavelengths. The cutoff wavelength is chosen based on what point the spectral emissive power of the absorber overtakes the incoming spectral power of solar radiation (and in this case, actual spectral power should be used, not normalized curves as in Fig. 1.5) [31]. In practice, the cutoff will not be perfectly sharp, and there will not be perfect absorption below the cutoff or perfect reflection above it. Despite this, very effective selective surfaces have been developed, with solar absorptances of around 95% and emittances of around 5% at 200°C and 20% at 500°C [32].

This covers the basic idea of how wavelength selective surfaces achieve the desired properties for absorbers in solar-thermal systems. Many details have been skipped over,

including the entire topic of how surfaces with these properties can be designed. Design of spectrally selective surfaces could be the topic of an entire thesis on their own [33], and as such exploring the topic in depth is beyond the scope of this work.

1.5 Thermoelectric figure of merit and TE efficiency

The second stage of a high performance STEG is efficiently converting the heat delivered to the thermoelectric generator into electricity. It should be noted that the following treatment assumes that the TE legs are insulated on the sides (that is, there is no heat transferred through the side walls). In reality, for high temperatures (300 °C and greater) radiative losses from the sides of the legs become significant. Such high temperatures are not considered in this thesis as ideal operating points however, and as such ignoring radiative losses from the TE legs should yield reasonably accurate results. The heat flow into a thermoelectric leg from the heat source modeled in one dimension and assuming constant material properties is given by [13]

$$Q_H = T_H S I + \frac{\Delta T}{R_T} - \frac{I^2 R_E}{2} \tag{1.14}$$

where Q_H is the heat flow into the leg, S is the Seebeck coefficient of the TE leg, I is the electrical current flowing through the leg, ΔT is the temperature drop across the leg (hot side temperature T_H minus cold side temperature T_C), R_T is the thermal resistance of the leg and R_E is the electrical resistance of the leg. As shown in Eq. (1.14) the total heat flow through the leg is the sum of heat flow from the Peltier effect (the first term on the right hand side (RHS) of Eq. (1.14)) and Fourier conduction (the second term on the RHS) minus half the heat generated in the elements from Joule heating (the third term on the RHS). It should be noted that this

treatment neglects the Thomson Effect, as the Seebeck coefficient is assumed to be constant as a function of temperature. The thermal and electrical resistances of the TE leg are given by

$$R_T = \frac{L_{te}}{k_{te}A_{te}} \tag{1.15}$$

$$R_E = \frac{L_{te}}{\sigma_e A_{te}} \tag{1.16}$$

where L_{te} is the length of the leg, A_{te} is the cross-sectional area of the leg, k_{te} is the thermal conductivity of the TE material and σ_e is the electrical conductivity of the TE material. The current through the TE leg I can be calculated as the voltage induced by the Seebeck effect divided by the total resistance of the circuit as in

$$I = \frac{S\Delta T}{R_E + R_L} \tag{1.17}$$

with R_L being the load resistance that the TE leg is connected in series with. The voltage drop V across the TE leg is given by the induced voltage minus the voltage lost by driving the current through the TE leg as given by Ohm's law (or can simply be given with Ohm's law by voltage drop across the load):

$$V = S\Delta T - IR_E = IR_L \tag{1.18}$$

The power P delivered to the load is simply the product of the current and voltage:

$$P = IV = \frac{S^2\Delta T^2 R_L}{(R_E + R_L)^2} \tag{1.19}$$

There are two conditions one may be interested in achieving when choosing a load resistance for

a given thermoelectric generator and temperature drop. The first is maximum power, which can be found easily by taking the derivative of the power (Eq. (1.19)) with respect to load resistance and setting to zero. This yields the load matching condition $R_L = R_E$ and gives the maximum power output P_{max} as:

$$P_{max} = \frac{S^2 \Delta T^2}{4R_E} \tag{1.20}$$

The other condition of interest, which is much more relevant to STEGs, is maximizing efficiency. Here the thermoelectric efficiency η_{te} is defined as the electrical power delivered to the load divided by the heat flow through the thermoelectric leg:

$$\eta_{te} = \frac{P}{Q_H} = \frac{I^2 R_L}{T_H S I + \frac{\Delta T}{R_T} - \frac{I^2 R_E}{2}} \tag{1.21}$$

We would like to take the derivative of efficiency with respect to load resistance and set this to zero in order to find the correct load matching condition (a more convenient form for doing this is given in Eq. (1.22)).

$$\eta_{te} = \frac{S^2 \Delta T R_L}{T_H S^2 (R_E + R_L) - \frac{1}{2} S^2 \Delta T R_E + \frac{(R_E + R_L)^2}{R_T}} \tag{1.22}$$

After taking the derivative, setting it equal to zero and working through a bit of algebra, the resulting expression for the optimal load resistance is given by

$$R_L^2 = R_E^2 + R_E R_T S^2 T_M \tag{1.23}$$

where T_M is the mean temperature of the TE leg defined by $T_M = (T_H + T_C)/2$. If we define a thermoelectric figure of merit Z by

$$Z = \frac{S^2 \sigma_e}{k_{TE}} \tag{1.24}$$

with units of inverse Kelvin (the significance of this quantity will be discussed in more detail shortly) and rearrange the equation, what is left is the simple ideal load matching condition:

$$R_L = R_E \sqrt{1 + ZT_M} \tag{1.25}$$

Plugging this ideal load matching condition into the equation for thermoelectric efficiency yields the result:

$$\eta_{te} = \frac{(T_H - T_C)}{T_H} \frac{\sqrt{1 + ZT_M} - 1}{\sqrt{1 + ZT_M} + T_C/T_H} \tag{1.26}$$

For STEGs, maximum power generation and maximum efficiency occur for the same load matching condition, as a flux (incident solar radiation) is the hot-side boundary condition rather than a heat reservoir. In this case, the load matching condition is given by Eq. (1.25) and the resulting efficiency is still given by Eq. (1.26) [23].

The thermoelectric efficiency is often thought of as the product of Carnot efficiency and a thermoelectric factor less than unity which is a function of the dimensionless thermoelectric figure of merit ZT. As ZT approaches infinity, the thermoelectric efficiency approaches Carnot. Thus the importance of the thermoelectric figure of merit ZT becomes clear. Improved ZT leads

to more efficient thermoelectric generator operation, and in thermoelectric cooler applications (which will not be explored in this thesis) higher ZT leads to a better coefficient of performance. Therefore, when looking for or designing a thermoelectric material, high ZT in the intended operating temperature range is the primary concern for performance.

Designing good thermoelectric materials (i.e., those with high ZT) is a huge area of research [34–36], and will only be discussed briefly in this thesis. As mentioned previously, there are three material properties important to thermoelectric performance which all appear in the expression for ZT (see Eq. (1.24)): the Seebeck coefficient, electrical conductivity and thermal conductivity. Seebeck coefficient should be large as a high Seebeck coefficient represents strong coupling between heat and electrons, which is the principle behind the thermoelectric effect in the first place. High electrical conductivity is desirable because it allows higher electrical currents to flow and reduces Joule heating. Low thermal conductivity is desirable because heat flowing through the thermoelectric leg via normal Fourier means can be thought of as "leaking" through and not contributing to influencing electrons. The numerator of the figure of merit $S^2\sigma_e$ is referred to as the power factor, and attempts at improving it are usually through manipulating the electron density of states at the Fermi level of the material [37, 38]. Most efforts at reducing thermal conductivity are through nanostructuring the material and introducing interfaces which scatter the thermally induced heat carrying lattice vibrations (phonons) but have a small effect on electrons [39, 40].

1.6 Overall STEG efficiency and $C_{th}L_{te}$

The overall STEG efficiency η is simply a product of the opto-thermal and thermoelectric efficiencies. This means that with a few reasonable assumptions (those made in the derivation of

the previous two sections) we can use the expressions for the sub-efficiencies found above to find the overall STEG efficiency:

$$\eta = \eta_{ot}\eta_{te} = \left(\alpha\tau - \frac{\epsilon\sigma(T_H^4 - T_C^4)}{CG}\right)\frac{(T_H - T_C)}{T_H}\frac{\sqrt{1+ZT_M}-1}{\sqrt{1+ZT_M}+T_C/T_H} \tag{1.27}$$

For simplicity the ambient temperature T_A is now assumed to be the same as the device cold side temperature T_C. Given a constant thermoelectric figure of merit ZT_M and constant radiative properties on the absorber side of the device, optimization becomes a simple matter of selecting the ideal hot-side temperature. The optimal hot side temperature arises from a balance between thermoelectric efficiency (which increases with increasing hot side temperature) and opto-thermal efficiency (which decreases with increasing hot side temperature). An example curve with ZT = 1, T_C = 30 °C, G = 1000 W/m^2, ϵ = 0.08 and $\alpha = \tau$ = 0.95 is shown in Fig. 1.6. For these conditions, a maximum efficiency of 5.3% is achieved at a hot side temperature of 232 °C.

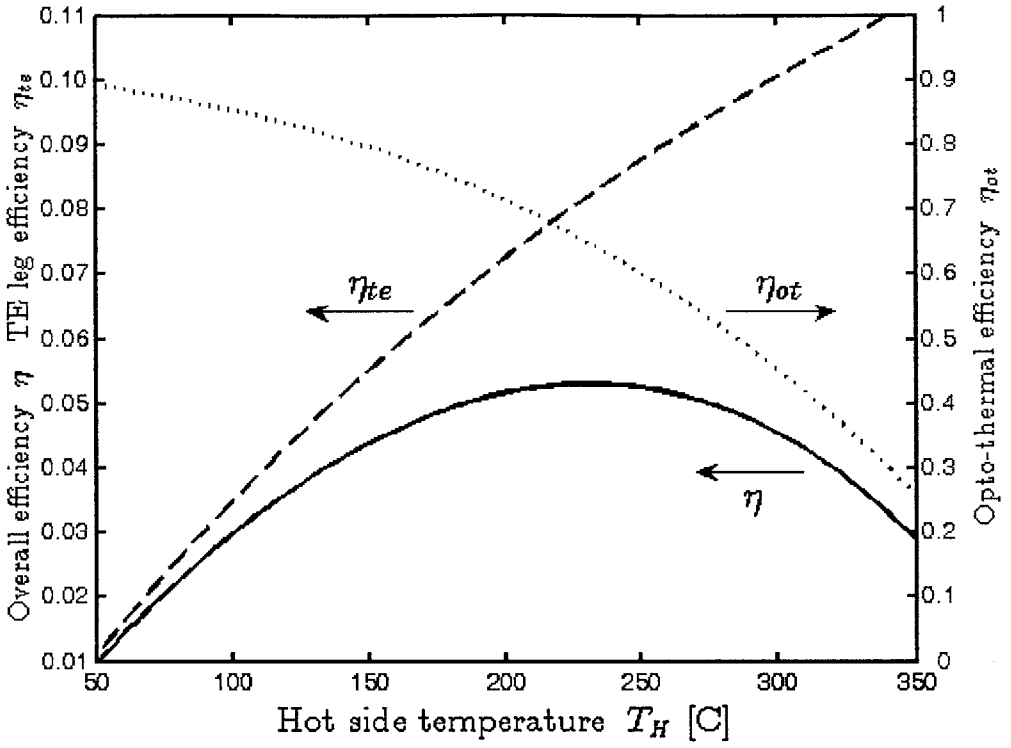

Figure 1.6 STEG efficiencies as a function of hot side temperature: solid black curve for overall efficiency and dashed blue curve for TE efficiency on the left axis, dotted green curve for opto-thermal efficiency on the right axis

The hot side temperature of the device can be calculated through a balance between heat flow into the absorber given by the radiative heat transfer modeling:

$$Q_H = A_{abs}[G\alpha\tau - \epsilon\sigma(T_H^4 - T_C^4)] \tag{1.28}$$

with A_{abs} being total absorber area, and heat flow through the TE leg given by Eq. (1.14) . This yields the balance

$$A_{abs}\left(G\alpha\tau - \epsilon\sigma(T_H^4 - T_C^4)\right) = T_H SI + \frac{\Delta T}{R_T} - \frac{I^2 R_E}{2} \tag{1.29}$$

a quartic function of T_H which is non-trivial but solvable. In practice, the hot-side temperature is set by the geometry of the device (L_{te}, A_{te}, and so on) if the properties of the thermoelectric material and the radiative properties of the absorber are treated as given.

Exploring the full space of possible geometries for thermoelectric generator designs would be quite a tedious undertaking. Fortunately, previous work [23, 41] has shown that under reasonable assumptions, the effect of device geometry can be distilled into a single parameter $C_{th}L_{te}$, which is the length weighted thermal concentration. The thermal concentration C_{th} is a measure of how much solar radiation striking and "thermally concentrated" by the absorber through the TE legs of the device, and is defined by:

$$C_{th} = \frac{A_{abs}}{A_{te}} \tag{1.30}$$

The assumptions used in this analysis are an isothermal absorber and negligible thermal and electrical contact resistances. Temperature independent thermoelectric properties make demonstrating the sole importance of $C_{th}L_{te}$ easier, but temperature independence is not explicitly necessary.

The interested reader is encouraged to find details for the derivation of the dependence of hot side temperature and therefore device efficiency on $C_{th}L_{te}$ in work by Chen [23] and Kraemer et. al [41]. Only an intuitive understanding will be explored in this thesis. We expect that the temperature drop across the leg (which would consequently give hot side temperature) should be equal to the product of the heat flow through the leg and the thermal resistance of the leg:

$$\Delta T = Q_H R_T = A_{abs}[G\alpha\tau - \epsilon\sigma(T_H^4 - T_C^4)]\frac{L_{te}}{k_{te}A_{te}} \tag{1.31}$$

Some algebra yields results which clearly show the importance of $C_{th}L_{te}$ to the temperature drop across the TE leg:

$$\Delta T = C_{th}L_{te}\frac{[G\alpha\tau - \epsilon\sigma(T_H^4 - T_C^4)]}{k_{te}} \tag{1.32}$$

$$\Delta T = C_{th}L_{te}\frac{G\alpha\tau}{1 + \epsilon\sigma(T_H^2 + T_C^2)(T_H + T_C)} \tag{1.33}$$

At first glance it might appear that Eqns. (1.32) and (1.33) show a proportional relationship between ΔT and $C_{th}L_{te}$, however the T_H dependence on the RHS means that the relationship is more complex. Temperature drop increases with increasing $C_{th}L_{te}$, but T_H asymptotically reaches some maximum value, rather than increasing unbounded. This maximum temperature is given by the case when the absorber is insulated from its surroundings besides radiative exchange:

$$0 = G\alpha\tau - \epsilon\sigma(T_{H,max}^4 - T_C^4) \tag{1.34}$$

$$T_{H,max} = \sqrt[4]{\frac{G\alpha\tau}{\epsilon\sigma} + T_C^4} \tag{1.35}$$

It makes intuitive sense that T_H should increase with $C_{th}L_{te}$ as heat flow through the TE leg should increase with C_{th} and thermal resistance of the TE leg increases with L_{te}. While Eqns. (1.32) and (1.33) are not sufficient to show the exact relationship between T_H and $C_{th}L_{te}$, it is enough to show that $C_{th}L_{te}$ is the only geometric parameter important to determining hot side temperature.

Previous work offers a strong foundation on which to analyze the performance of STEG systems [16, 17, 23, 41]. The performance of the opto-thermal and thermoelectric sides of the device can be investigated separately, and combined in the end. Additionally, specifics of geometry are not important for traditional STEGs in the majority of operating regimes, the only important geometric parameter is $C_{th}L_{te}$.

1.7 Thesis outline

This thesis explores potential improvements to STEGs through improvements in device design. There are two improvements which are investigated: the potential of thin-film STEGs and the use of an optical cavity for the STEG solar receiver. Thin-film STEGs are investigated in chapter 2, which is a reprinted article from the Journal of Applied Physics (authored by the author of this thesis). Chapter 3 concerns the optical cavity, which can improve STEG performance by improving opto-thermal efficiency of the system. The optical cavity investigated can improve STEG performance, but could also conceivably improve the performance of any solar-thermal system, it is not limited to solely thermoelectric energy conversion technologies.

Chapter 2 Modeling of Thin-Film Solar Thermoelectric Generators

2.1 Introduction

The recent experimental demonstration of high performance STEGs by Kraemer et al. was based on bulk thermoelectric materials [16]. Unlike the conventional application of thermoelectric conversion of heat into electricity that requires physical contacts between the heat source and the thermoelectric generator, solar photons do not exert much force on the STEG. This leads to the possibility that thin-film thermoelectric materials, which have seen some progress in the past [35, 42, 43] can be used in STEGs. This would seem reasonable, as thin-film thermopile infrared detectors are commercially available [44, 45] and thin-film photovoltaic devices have seen commercial success [46]. Previous studies have considered thin-film thermoelectric coolers and generators [47–49]. A recent study has investigated thin-film STEGs, however the performance found was significantly lower than bulk material STEG performance [50]. Thin-film STEGs operate at higher temperatures than thermopiles, and have special considerations regarding the area occupied by the thermoelectric legs and the heat sink.

This chapter presents a modeling study on the performance of thin-film STEGs. In section 2.2, the device geometry is described and models with progressive sophistication are

presented, starting from an isothermal absorber, followed by a model considering the temperature non-uniformity in the absorber, and numerical simulation including other non-idealities. Two key lumped parameters are derived which allow general discussion of the efficiency of thin-film STEGs of different geometries. In section 2.3, results based on typical materials properties are discussed. It is found that thin-film STEGs can have similar performance as bulk materials-based STEGs.

2.2 Model

Figures 2.1a and 2.1b show schematics for the planar thin-film STEG being investigated. Solar insolation heats up the solar absorber and the hot side of the thermoelectric generator, and the surroundings keep the cold side of the thermoelectric generator cool so that a temperature gradient is developed. In this configuration the solar absorber, thermoelectric legs and heat sink all lie in the same plane (with p-type legs on the left and n-type legs on the right). Benefits of this configuration are the potential for easier manufacturing and reduced material costs, as microfabrication techniques could allow for batch processing as well as extremely low material usage. The main disadvantage of this design is that intercepted sunlight is incident on the thermoelectric material and the heat sink, in addition to the solar absorber. Another disadvantage is that electrical current flows through the solar absorber, leading to resistance losses, although this can be avoided by placing p-n TE pairs on each side of the absorber. In this study, we will focus on the device configuration in Fig. 2.1 and investigate the performance of this configuration for comparison to that of existing designs.

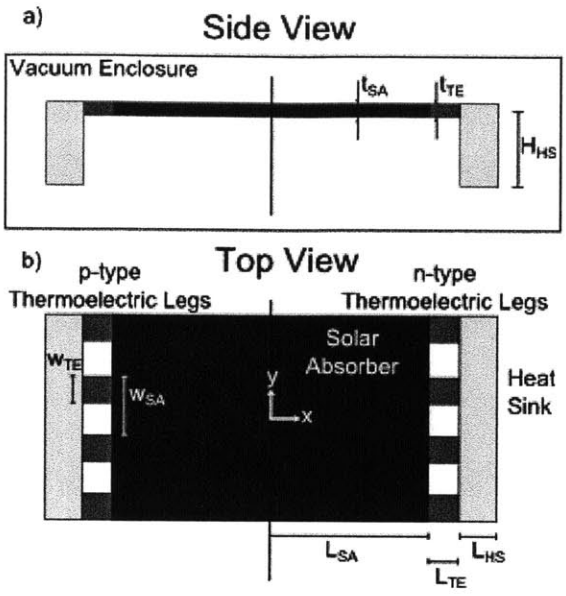

Figure 2.1 a) side view and b) top view of thin-film STEG geometry, with relevant lengths labeled

Approximations used throughout the entirety of the chapter are:

- The dimensionless thermoelectric figure of merit ZT_M is assumed constant,
- All other properties (e.g. absorber emissivity, absorptivity, conductivity, etc.) are assumed to be temperature independent,
- The far end of the heat sink is always maintained at ambient temperature,
- While in reality n and p-type thermoelectric materials have different properties, here they are assumed to be identical except for the sign of the Seebeck coefficient. This allows for symmetry across the midplane of the STEG, so that one half can be analyzed and the results will match those of the full device.
- All convective losses from the solar absorber are ignored, as they are assumed to be negligibly small due to the device being in an evacuated enclosure.

For the majority of this study the device is treated as one-dimensional, in the sense that temperature variations are only considered in the x-direction for the solar absorber. The validity of this approximation is verified in later sections. It should also be noted that the 1-D nature of the analysis leads to some areas being better represented by lengths. In these situations it can be assumed that the area in question is the length noted multiplied by a unit length in the y-direction.

We will first discuss the thin-film STEG performance under the ideal case, for which the absorber is treated as isothermal with no radiative losses from the TE legs, no electrical resistance in the solar absorber, and no plan area (area in the x-y plane) dedicated to the heat sink. This ideal case will provide an upper limit for the device efficiency. Following this, temperature variation in the absorber will be considered based on a differential analysis of the absorber. The bulk of the chapter is based on a 1-D approximation. Additionally, brief treatments on the effects of manufacturing limitations, heat sink plan area, radiative losses from the TE legs, electrical resistance in the solar absorber, and 2-D temperature distributions in the absorber will be provided. We show that with proper design, thin-film STEGs can achieve similar performance as STEGs using bulk materials.

The operation of the thermoelectric elements is given by the following equations [13]:

$$Q_H = T_H SI + \frac{\Delta T}{R_T} - \frac{I^2 R_E}{2} \tag{2.1}$$

$$R_T = \frac{L_{TE}}{k_{TE} t_{TE} PF} \tag{2.2}$$

$$R_E = \frac{L_{TE}}{\sigma_e t_{TE} PF} \tag{2.3}$$

Q_H is the heat flowing through the thermoelectric elements, which is the sum of heat flow from

the Peltier effect (the first term on the right hand side (RHS) of Eq. (2.1)) and Fourier conduction (the second term on the RHS) minus half the heat generated in the elements from Joule heating (the third term on the RHS). T_H is the hot side temperature, ΔT is the temperature drop across the thermoelectric, S is the Seebeck coefficient of the TE element, and I is the electrical current through the TE element. R_T and R_E are the thermal and electrical resistances per unit depth of the TE leg, respectively. L_{TE} is the length of the thermoelectric element, t_{TE} is the thickness, and PF is the packing fraction, or the proportion of total space in the y direction occupied by thermoelectric legs. k_{TE} is the thermal conductivity of the TE and σ_e is its electrical conductivity.

For STEGs, operation at maximum power generation corresponds to operation at maximum efficiency since a constant flux (incident solar radiation), not a heat reservoir with constant temperature, is the hot-side boundary condition [23]. The load matching condition to achieve maximum efficiency in STEGs is $R_L/R_E = \sqrt{1+ZT_M}$ and accordingly this load matching condition is used for the entirety of the analysis [23], where Z is the thermoelectric figure of merit $S^2\sigma_e/k_{TE}$ and T_M is the mean TE temperature. The efficiency is given as simply the ratio of electrical power generated to solar radiation incident on the device:

$$\eta = \frac{P}{G(L_{SA} + L_{TE} + L_{HS})} \tag{2.4}$$

with G being solar insolation. It can also be shown that efficiency can be found as a product of three sub efficiencies:

$$\eta = \eta_{geom}\eta_{ot}\eta_{te} \tag{2.5}$$

$$\eta_{geom} = \frac{L_{SA}}{L_{SA} + L_{TE} + L_{HS}} \tag{2.6}$$

$$\eta_{ot} = \frac{Q_H}{L_{SA}G} \tag{2.7}$$

$$\eta_{te} = \frac{(T_H - T_C)}{T_H} \frac{\sqrt{1 + ZT_M} - 1}{\sqrt{1 + ZT_M} + T_C/T_H} \tag{2.8}$$

η_{geom} is a geometric efficiency which arises from light not striking the solar absorber being ignored, as the non-absorber plan area should be small and has not been optimized for absorbing sunlight. η_{ot} is the opto-thermal efficiency, which is the ratio of heat flow into the thermoelectric leg compared to sunlight intercepted by the absorber. Finally, η_{te} is the TE leg efficiency, which is simply the efficiency of a thermoelectric generator operating between a hot and cold temperature [13]. The inclusion of η_{geom} is what differentiates planar STEG performance from previous designs [23].

2.2.1 Isothermal absorber

In the simplest and most ideal model for the planar STEG the solar absorber is isothermal (equivalent to having infinite thermal conductivity), the thermoelectric legs are insulated except at the junctions (no radiative losses) the solar absorber is treated as having infinite electrical conductivity (no Joule heating in the absorber) and the cold side of the TE legs are assumed to be at T_C without the use of any device plan area for a heat sink ($L_{HS} = 0$). In this model, hot side temperature can be found from a steady-state energy balance in the solar absorber:

$$L_{SA}G\tau\alpha - L_{SA}\epsilon^*\sigma\left(T_H^4 - T_C^4\right) - Q_H = 0 \tag{2.9}$$

with ϵ^* being effective emittance (accounting for both front and backside heat losses). Here, absorbed solar insolation (the first term on the left hand side (LHS)) must match radiation losses

(the second term on the LHS) and heat flow through the thermoelectric legs Q_H. With device parameters and geometry set, Eqs. (2.1) and (2.9) are sufficient to find T_H, which then yields ΔT and therefore power and efficiency.

Using this equation, η_{ot} can be found as a simple function of hot side temperature [23]:

$$\eta_{ot} = \tau\alpha - \frac{\epsilon'\sigma(T_H^4 - T_C^4)}{G} \tag{2.10}$$

while the other efficiencies remain simple to calculate with a given geometry and hot side temperature. In practice, the hot side temperature is set by modifying device geometry.

2.2.2 1-D Absorber temperature distribution

The previous analysis does not consider that radiative losses along the absorber will influence the temperature profile. This section considers a one-dimensional temperature distribution that arises in the absorber from radiative losses and finite absorber conduction. This reduces performance, as the TE elements see a reduced T_H and therefore a reduced ΔT. In reality there will also be radiative losses from the TE legs, however this is ignored now because the TE leg area should be small enough as to render those losses negligible, and this would introduce unnecessary complications into the modeling. Thus, only radiative losses from the absorber are considered. Joule heating in the absorber is still ignored in this section, as we expect it to be negligible due to the absorber likely being composed of a highly electrically conductive metal (e.g. copper).

The temperature distribution in the absorber can be described by

$$\frac{d^2T}{dx^2} = \frac{\sigma\epsilon'(T^4 - T_C^4) - G\tau\alpha}{k_{SA}t_{SA}} \tag{2.11}$$

which is derived by taking a differential element of the absorber. The boundary condition for this differential equation at $x = 0$ (assigned to the center of the absorber) is no temperature gradient, which arises from symmetry. The boundary condition at the far end is that the heat flow out of the absorber

$$Q_H = -k_{SA} t_{SA} \left.\frac{dT}{dx}\right|_{L_{SA}} \tag{2.12}$$

must match the heat flow through the TE legs. This equation and boundary condition can be expressed as follows:

$$\frac{d^2T}{dx^{*2}} = \phi(\sigma\epsilon' T^4 - C) \tag{2.13}$$

$$Q_H = -\frac{k_{SA} t_{SA}}{L_{SA}} \left.\frac{dT}{dx^*}\right|_{x^*=1} \tag{2.14}$$

with:

$$x^* = x/L_{SA} \tag{2.15}$$

$$\phi = \frac{L_{SA}^2}{k_{SA} t_{SA}} \tag{2.16}$$

$$C = \sigma\epsilon' T_C^4 + G\tau\alpha \tag{2.17}$$

where x^* is a non-dimensional length along the solar absorber, ϕ determines the curvature of the temperature distribution in the absorber and C is a constant assuming the constitutive parameters are given. The significance of ϕ will be shown in later sections.

Once the temperature distribution has been solved with the boundary conditions met, electrical power output and efficiency can be solved for as before, where ΔT now depends on the temperature at the edge of the solar absorber.

2.2.3 Consideration of heat sink

In addition to the hot side of the TE leg seeing a reduced temperature from the theoretical maximum absorber temperature, the cold side will see an elevated temperature from the environmental temperature due to thermal resistance of the STEG heat sink. This also reduces performance, as the true ΔT that the TE elements are operating under is reduced. The cold side temperature of the TE leg is given by

$$T_{C,TE} = \frac{Q_C H_{HS}}{k_{HS} L_{HS}} + T_C \tag{2.18}$$

where the temperature increase (first term on right hand side of the equation) is the heat flow through the heat sink (heat flow into the TE leg minus electrical power generated) multiplied by the thermal resistivity of the heat sink. In choosing the heat sink size, there is a balance between making the heat sink too small (as this will cause too considerable a cold side temperature increase, reducing power output) and too large (as this will have too much plan area dedicated to the heat sink, reducing efficiency).

2.2.4 Numerical Simulation

In addition to the mathematical models developed, we used the commercial software package COMSOL to run simulations for verification of the model's accuracy. Previous analysis considered only a one-dimensional temperature distribution in the absorber, whereas with COMSOL we simulated the more realistic two-dimensional distribution. COMSOL simulations

also allowed the addition of more complicated features, such as finite electrical conductivity in the solar absorber and solar absorption and radiative losses in the TE legs, which were not included in the simplified mathematical models. In the COMSOL model, standard Fourier conduction was used for the absorber and heat sink sections (with radiative boundary conditions at the free surfaces), while a TE model using conservation of charge and thermal energy which accounted for the Seebeck and Peltier effects was used for the TE domain. Power output was calculated by multiplying current through the TE leg and voltage drop across the device (TE leg and solar absorber).

2.2.5 Scaling considerations

With some manipulation of the temperature distribution equation (2.13) and boundary conditions it can be shown that there are a few parameters which determine performance regardless of scale. It is clear that ϕ is an important parameter which arises from the mathematics of the model. ϕ is the absorber length multiplied by its thermal resistance, which one would expect to have significant impact on the absorber temperature distribution. There is another important parameter that arises naturally from the mathematics as well. The temperature drop across the TE legs can be described by:

$$\Delta T = \frac{L_{TE}}{k'_{TE} t_{TE} PF} Q_H \tag{2.19}$$

where k'_{TE} is the effective thermal conductivity of the thermoelectric legs considering Fourier conduction as well as Peltier and Joule heating (whereas the standard thermal conductivity only accounts for Fourier conduction). The effective thermal conductivity is given in the ideal load matching case by:

$$\frac{k'_{TE}}{k_{TE}} = 1 + ZT_M \left(\frac{1 + \frac{T_H}{T_M}\sqrt{1 + ZT_M}}{\left(1 + \sqrt{1 + ZT_M}\right)^2} \right) \tag{2.20}$$

which can be derived by equating

$$Q_H = \Delta T \frac{k'_{TE} PF t_{TE}}{L_{TE}} \tag{2.21}$$

to the expression for Q_H given in Eq. (2.1) . Substituting Q_H from Eq. (2.14) into Eq. (2.19) yields:

$$\Delta T = \frac{L_{TE}}{k'_{TE} t_{TE} PF} \frac{k_{SA} t_{SA}}{L_{SA}} \left(-\left. \frac{dT}{dx^*} \right|_1 \right) \tag{2.22}$$

Here the non-dimensional term preceding the temperature gradient is the ratio between the thermal resistance of the TE legs and the solar absorber, which will be designated γ', and can be expressed as follows:

$$\gamma' = \frac{L_{TE}}{L_{SA}} \frac{k_{SA} t_{SA}}{PF k'_{TE} t_{TE}} \tag{2.23}$$

It can be shown that if ϕ, defined by Eq. (2.16) , and γ' are maintained, despite changing other parameters (thicknesses, packing fraction, and absorber conductivity), the non-dimensional temperature distribution for Eq. (2.13) and the associated boundary conditions are still met. Configurations with identical temperature distributions will have the same values for η_{ot} and η_{te}, and overall performance will only differ if η_{geom} changes. In the case of t_{SA} and t_{TE} being scaled equally (with ϕ and γ' held constant), it can be shown that η remains the same.

An important derived parameter is the product of ϕ and γ', which is the strongest determining factor of the hot side temperature. We will label this parameter β':

$$\beta' = \frac{L_{SA} L_{TE}}{PF k'_{TE} t_{TE}} \tag{2.24}$$

This is the product of solar absorber length and TE leg thermal resistance, with units of K m^2/W, so it makes sense that it would be related to temperature difference for a given solar insolation and that it would have a significant impact on hot side temperature. This grouping can be related to the quantity $C_{th}L$ (geometric concentration ratio times TE leg length) that has been explored previously [23, 41], with the main differences being the inclusion of k'_{TE} and that since this analysis includes temperature drop in the absorber, the hot side temperature is not only a function of β'.

It should be noted that because k'_{TE} is a function of temperature, some problems arise if one attempts to evaluate a configuration with a given β' or γ', since the hot side junction temperature is unknown, which adds unneeded iterative steps. k'_{TE}/k_{TE} is relatively constant for the range of temperatures with which we are concerned (less than 2% change for $ZT_M = 1$ from T_M = 450 K to 550 K or 177 °C to 277 °C). If k'_{TE}/k_{TE} is treated as constant, then k'_{TE} and k_{TE} can be interchanged in β' and γ', as their absolute values are somewhat arbitrary. Thus, the following expressions (note lack of k'_{TE}) are used for the remainder of the analysis:

$$\beta = \frac{L_{SA} L_{TE}}{PF k_{TE} t_{TE}} \tag{2.25}$$

$$\gamma = \frac{L_{TE}}{L_{SA}} \frac{k_{SA} t_{SA}}{PF k_{TE} t_{TE}} \tag{2.26}$$

It should be noted however that the treatment of exchanging k_{TE} and k'_{TE} is not necessarily acceptable for other thermoelectric materials or temperature ranges.

These parameters give more direct expressions for geometric and opto-thermal efficiencies (the expression for geometric efficiency assumes $L_{HS} = 0$):

$$\eta_{geom} = \frac{1}{1 + \gamma \frac{PF k_{TE} t_{TE}}{k_{SA} t_{SA}}} \tag{2.27}$$

$$\eta_{ot} = \frac{-1}{\phi G} \frac{dT}{dx^*}\Big|_{x^*=1} \tag{2.28}$$

The TE leg efficiency is still a simple function of T_H and ZT_M (Eq. (2.8)).

2.3 Results and Discussion

Table 2.1 shows the parameter values used for numerical simulations.

Table 2.1 Parameters used in simulation

Parameter	Symbol	Value
Solar insolation	G	1000 W/m2
Cold side and ambient temperature	T_C	300 K
Enclosure transmittance	τ	0.95
Absorber effective absorptance	α	0.95
Absorber effective emittance	ϵ^*	0.075
Absorber thermal conductivity	k_{SA}	400 W/m/K
Absorber electrical conductivity	$\sigma_{e,SA}$	$6*10^7$ S/m
TE dimensionless figure of merit	ZT_M	1
TE thermal conductivity	k_{TE}	1.6 W/m/K
TE leg packing fraction	PF	0.5
Heat sink thermal conductivity	k_{HS}	150 W/m/K

The solar insolation value is standard for AM 1.5G solar spectrum specifications [51]. Insolation affects the temperature distribution (Eqs.(2.13) and (2.17)) and opto-thermal efficiency (Eq. (2.28)), with higher values leading to better overall performance. The transmittance value is taken as reasonable for a glass enclosure. The absorber properties are commercially achievable (the emittance takes into account losses from both the front and back sides), with thermal and electrical conductivity values typical for copper, which would easily be used as a heat spreader beneath the selective surface. The dimensionless thermoelectric figure of merit is taken to be constant for simplicity, and is typical of bismuth telluride [52, 53]. The TE thermal conductivity is given explicitly as it arises in determining η_{geom} (Eq. (2.27)). A conservative packing fraction is used, which also influences η_{geom} (lower packing fractions lead to better performance). The heat sink thermal conductivity value is typical of crystalline silicon, as the planar STEG was imagined to take advantage of MEMS fabrication techniques. As long as ϕ and γ remain constant, the thickness of the absorber and TE elements can be scaled without a loss in efficiency, and they were always taken to be the same thickness.

Parametric studies varying β and γ as defined by Eqs. (2.25) and (2.26) were performed using the property values provided in Table 2.1. Results from these parametric studies are provided below, with a focus on values of β and γ which led to the highest efficiency given the property values used.

2.3.1 Isothermal absorber

In the isothermal absorber case, thermoelectric and opto-thermal efficiencies are solely a function of absorber temperature. While β was derived working through mathematics of the 1-D temperature distribution case, it is still relevant here, as geometry determines hot side

temperature and β has a one-to-one mapping with the hot side temperature (as it is equivalent to $C_{th}L$ investigated previously [23, 41]).

With the isothermal absorber approximation, the same value of β can be maintained while varying the relative lengths L_{SA} and L_{TE} in Eq. (2.25) . This means that L_{SA} can be made arbitrarily large and L_{TE} can be made arbitrarily small, leading to a geometric efficiency of 1. Therefore in the isothermal absorber case, performance of the planar STEG is indiscernible from the performance of traditional STEG configurations. As an example, for a TE leg thickness of 500 nm and packing fraction of 0.5, if L_{SA} is set at 5 cm, the corresponding L_{TE} for optimal performance is about 4 μm, four orders of magnitude smaller. While this particular device would be almost impossible to fabricate, it demonstrates that in the isothermal approximation TE leg plan area can be made negligibly small as long as contact resistance is ignored.

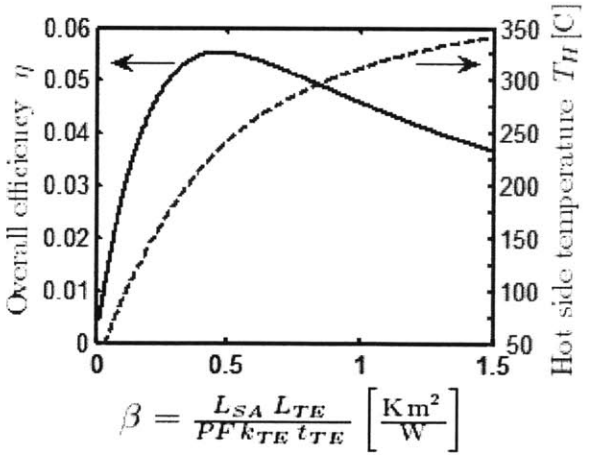

Figure 2.2 Efficiency (left axis, solid line) and absorber temperature (right axis, dashed line) for varying β in isothermal absorber approximation

Figure 2.2 shows hot side temperature and corresponding efficiency for a range of β. The maximum efficiency is slightly over 5.5% at a hot side temperature of 235 °C, which

corresponds to a β of about 0.47 K m^2/W. As with previous work, higher temperatures lead to better thermoelectric efficiencies but worse opto-thermal efficiencies, resulting in an optimal hot side temperature [16]. Larger values of β lead to higher temperatures, so the optimal hot side temperature is achieved with a corresponding optimal β. This result provides a decent starting point for selecting β when finite absorber conduction is considered, as will be shown later.

2.3.2 1-D Absorber temperature distribution

A noticeable drop in efficiency is observed when the temperature distribution within the absorber is accounted for. A typical temperature distribution is shown in Fig. 2.3, in this case for $\beta = 0.45$ K m^2/W and $\gamma = 14$.

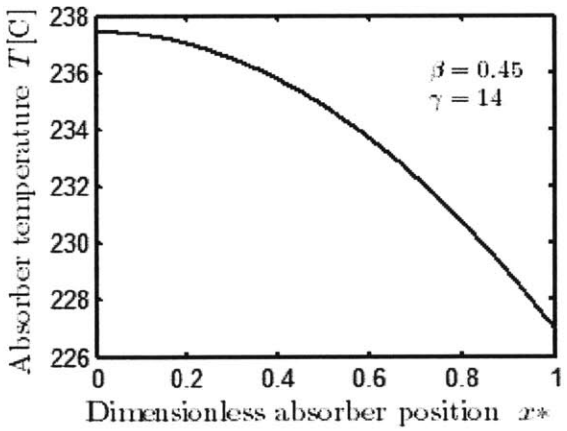

Figure 2.3 Temperature distribution along absorber for $\beta = 0.45$ and $\gamma = 14$

The temperature drop from the center of the absorber to the junction with the TE leg is about 11 °C . This temperature drop is responsible for the reduced efficiency, and adds some complexity to the device design. Efficiency is no longer solely a function of a uniform hot side temperature, but rather a function of both the parameters β and γ, which were defined earlier. β

affects the overall absorber temperature, and γ affects the slope of the temperature distribution, which is demonstrated in Fig. 2.4.

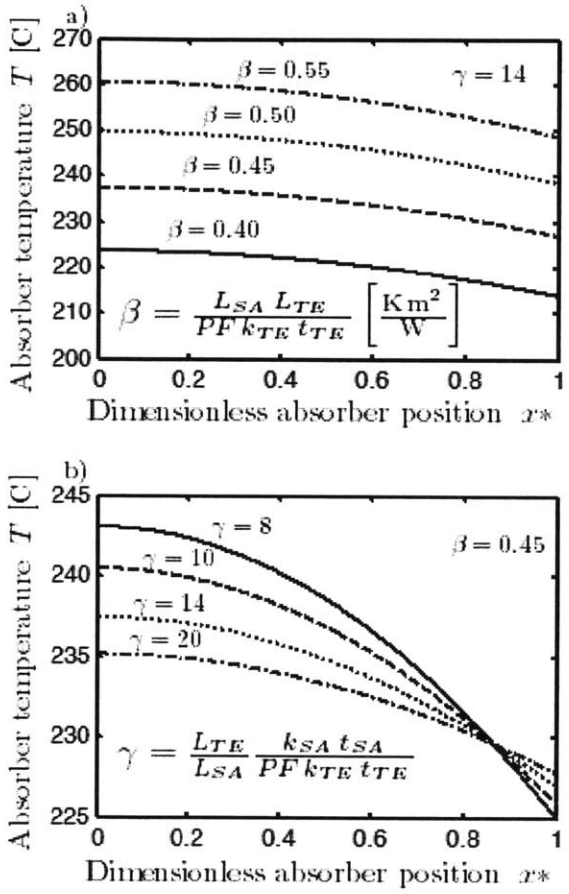

Figure 2.4 Temperature distributions in absorber for a) varying β with constant γ and b) varying γ with constant β

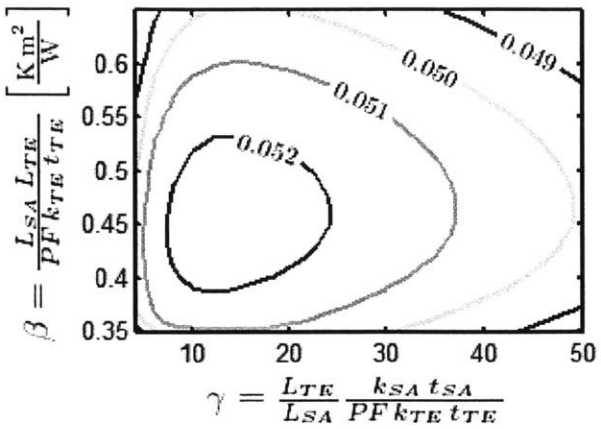

Figure 2.5 Efficiency contour plots for varying β and γ

It is important to find a suitable value of both β and γ to achieve a high efficiency. Figure 2.5 shows efficiency contours plotted against β and γ. The maximum efficiency in this case is about 5.25% with a β of 0.46 K m^2/W and a γ of 14. For an absorber and TE leg thickness of 500 nm with a packing fraction of 0.5, these values correspond to an absorber length of 2.6 mm and a TE leg length of 72 μm. Efficiency is very sensitive to β as this is the main determinant of absorber temperature, which heavily affects η_{te} and η_{ot}. There is also an optimal γ, which arises from the competition of two modes of efficiency loss. When γ is small, there is a large temperature drop in the absorber (operation is far from the isothermal absorber case), so the TE legs see a reduced temperature and η_{te} and η_{ot} are lowered. It is readily apparent that the lower ΔT will lead to a reduced η_{te}, but it is important to note that the lower ΔT also leads to a lower Q_H and therefore η_{ot}, which is contrary to the behavior of η_{ot} in the isothermal absorber case. When γ is large, the TE legs are relatively long, and η_{geom} is lowered.

The optimal value of β appears mostly constant near 0.45 K m^2/W, even for different packing fractions and absorber conductivities, however the optimal value of γ varies. Lower

packing fractions result in better overall efficiency, because the reduced thermoelectric leg length minimizes the geometric efficiency loss from sunlight incident on non-absorber surfaces. However, the benefit predicted from the 1-D model will overstate reality, as it does not consider temperature gradients in the y-direction that would occur for low packing fractions (in later sections it will be shown that this is of negligible concern). It also ignores contact resistance, which would lead to a large performance reduction for very short TE legs in practice. Increasing absorber thermal conductivity naturally increases efficiency, as it drives operation closer to the isothermal absorber case.

It was found that while the optimal γ varied for different configurations, the product of the optimal γ and the length ratio L_{TE}/L_{SA}, given by $(L_{TE}/L_{SA})^2\, k_{SA}t_{SA}/(PFk_{TE}t_{TE})$, stayed approximately constant at 0.35 for the range of packing fractions and absorber conductivities investigated. This result is very useful, as it gives a strong starting point for which values of γ to consider when looking at a new device configuration (however it is important to note that this value will not hold for different TE properties). Keeping this product constant accounts for the effect of changing parameters which maintain the same temperature distribution (i.e. γ and β held constant) and therefore η_{ot} and η_{te} but modify η_{geom}. When η_{geom} is improved (e.g. by decreased packing fraction or increased absorber conductivity), a higher γ value will be preferred for optimal performance, and this is accounted for by keeping $(L_{TE}/L_{SA})^2\, k_{SA}t_{SA}/(PFk_{TE}t_{TE})$ constant.

In some cases, the values of β and γ called for to maximize efficiency might not be feasible to achieve for structural or other reasons, as the proposed planar STEG involves very long, thin, suspended structures.

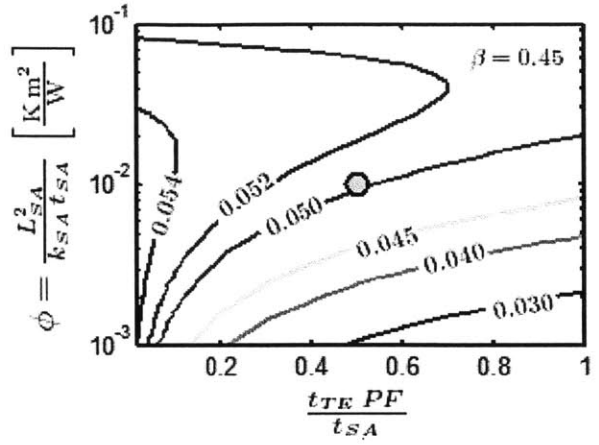

Figure 2.6 Efficiency with β = 0.45 K m2/W for varying "manufacturing" parameters, with a sample operating point marked. Note ϕ is log scale

Figure 2.6 shows contour plots of efficiency for two parameters that would feasibly be limited from a manufacturing perspective. ϕ, if very large, corresponds to an extremely long and thin solar absorber, which might not be practically achievable. The other parameter, $t_{TE}PF/t_{SA}$, is a ratio of TE to solar absorber cross sectional area, which one would like to minimize, but in practice would be difficult as a small value corresponds to sparse, thin TE legs supporting a thick solar absorber. In this plot, β is held constant at 0.45 K m^2/W, so the efficiencies should be near optimal for the corresponding manufacturing parameters. A point for $t_{TE}PF/t_{SA} = 0.5$, $\phi = 0.01$ K m^2/W is marked in Fig. 2.6. This corresponds to a sample case using 10 μm thick TE elements and solar absorber with an absorber length of 6.3 mm, a TE leg length of 0.6 mm and a packing fraction of 0.5, which would limit performance to around 5.0% efficiency.

It is also of interest to examine the effect of varying the effective emittance (emittance accounting for front and back side losses) of the solar absorber. When the emittance is modified, the β corresponding to ideal performance changes, as changing the emittance alters the balance

between η_{ot} and η_{te}. Figure 2.7 shows the maximum efficiencies that can be achieved for different values of ε^* and the corresponding values of β for a γ of 14.

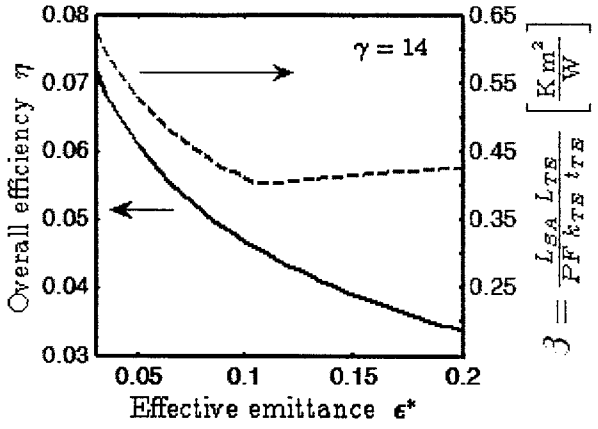

Figure 2.7 Efficiency (left axis, solid line) and β (right axis, dashed line) for varying ε^*

For low emittances, high values of β are preferred, since the lower emittance allows for high opto-thermal efficiency even at high temperature. For high emittances, β remains relatively constant, as it becomes more important to maintain an elevated temperature for a reasonable thermoelectric efficiency.

2.3.3 Consideration of heat sink

There is another drop in efficiency when some device area must be dedicated to a heat sink, in order to maintain the cold side temperature of the thermoelectric legs near the ambient temperature. In adding a heat sink, there are two competing factors which reduce efficiency. If the heat sink is large, there is a similar geometrical loss to having long thermoelectric legs, as any incident light striking the heat sink is wasted. If the heat sink is small, the temperature rise from ambient to the cold side of the thermoelectric legs is large, which reduces ΔT and consequently generator efficiency.

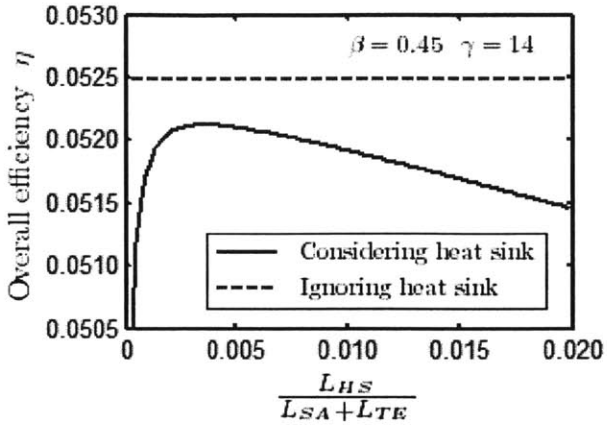

Figure 2.8 Efficiency for varying plan area dedicated to heat sink (solid line), compared to the ideal case (dashed line)

Figure 2.8 shows the device efficiency for various values of L_{HS} for a packing fraction of 0.5 with a β value of 0.45 K m^2/W and γ value of 14. The best performance when considering heat sink losses occurs with $L_{HS}/(L_{SA} + L_{TE}) = 0.0035$, and achieves an efficiency of 5.21%. This is a small drop from the value of 5.25% computed without consideration of the heat sink. For other β values and γ values the relative drop in efficiency is similar, and so consideration of heat sink effects on performance is not particularly important. The ideal value of $L_{HS}/(L_{SA} + L_{TE})$ is typical of other operating points as well. This suggests that in practice the heat sink width would be limited by fabrication and not by thermal considerations, as this analysis calls for absorbers millimeters long being supported by heat sinks which are micrometers wide.

2.3.4 Numerical Simulation Results

Results from COMSOL showed good agreement with results from the mathematical model, with typical errors less than 2%. This was found to be true for packing fractions down to 0.05, indicating that the 1-D assumption (no temperature distribution in the y direction) is an

acceptable approximation for the parameter values used in this study. When the effect of finite electrical conductivity (Joule heating) in the solar absorber was considered with copper properties, performance dropped a small amount (typically less than 0.1% absolute efficiency drop), indicating that the perfect electrical conduction approximation in the absorber is reasonable.

COMSOL simulations were also performed to evaluate the effect of a more realistic treatment of radiative absorption and emission in the thermoelectric legs. When the thermoelectric legs were modeled with an emissivity (and absorptivity) of 0.5 (typical of bismuth telluride), the drop in efficiency was on the order of 0.1% for large packing fractions (0.8) and almost negligible for low packing fractions (0.2). With the consideration of radiation in the TE legs, there was also a preference for lower values of γ, so optimal performance occurred with slightly smaller TE leg lengths.

2.4 Summary

A mathematical model was developed to investigate the performance of a novel configuration for STEGs. In the ideal case, using characteristic material properties, the planar STEG has performance virtually identical to traditional STEG configurations. With the added considerations of temperature drop in the absorber and area taken up by a heat sink, the efficiency of the device drops slightly. This is in agreement with results from COMSOL simulations of the device. Potential advantages in manufacturing thin-film STEGs make it a very appealing option, as the loss in efficiency from switching to this configuration is minimal.

Chapter 3 An Optical Cavity to Reduce Solar Absorber Radiative Losses

3.1 Introduction

The importance of solar absorbers to the efficient operation of STEGs was discussed in section 1.4, however the performance of solar absorbers is important to the overall operation of any solar-thermal system, not just STEGs. As mentioned previously, a solar absorber should absorb sunlight effectively, while having minimal radiative losses itself. This goal is complicated by Kirchoff's radiation law [28],

$$\alpha'_{\lambda} = \epsilon'_{\lambda} \tag{3.1}$$

which states that directional and spectral emissivity and absorptivity must be equal in observance of the second law of thermodynamics. Despite this limitation, it is still possible to achieve high absorptance and low emittance through clever manipulation of spectral and directional properties. Section 1.4 covered spectrally selective absorbers but did not consider directional selectivity. This chapter will discuss directionally selective absorbers, which see less use in practice today than spectrally selective absorbers. Theoretical investigations have shown significant improvements in performance of solar thermal systems which take advantage of directionally selective absorbers, so realizing them in practice is of paramount interest [29, 30].

Directional selectivity offers potential improvement in performance for solar absorbers due to the fact that solar radiation on the Earth's surface comes from essentially a point source.

Solar radiation on Earth has a divergence half-angle of about 0.25° [54]. This means that if a surface is designed such that it only absorbs at small angles to the surface normal, it can still absorb all direct solar radiation (that is, radiation which is not diffusely scattered in the atmosphere), given that the surface is pointed at the sun. Emittance is calculated by integrating across all angles [28]:

$$\epsilon_\lambda(T,\lambda) = 2\int_0^{\frac{\pi}{2}} \epsilon'_\lambda(T,\lambda,\theta)cos\theta sin\theta d\theta \tag{3.2}$$

If high absorptance is only needed at angles of 0.25° or less, Kirchoff's law only requires large emittance at these small angles. Therefore, if radiation from larger angles can be suppressed, the overall hemispherical emittance can be greatly reduced (see Eq. (3.2)). Thus the directionally selective surface is an effective solar absorber: a surface which emits minimal radiation while still collecting maximum incident solar radiation. It should be noted that the particular case of a 0.25° divergence half angle assumes no concentration. A larger absorptance (and therefore emittance) angle would be needed for concentrated sunlight. If the angular range of absorptance in a directionally selective absorber is very small, solar tracking would be required to keep the absorber pointed at the sun (similar to solar tracking being required for optically concentrating systems with high concentration ratios). Directionally selective absorbers have an advantage over spectrally selective absorbers in solar thermal applications. When operating at high temperature (where heat engine performance will be most efficient), spectral overlap starts to degrade performance. With a directionally selective absorber, performance need not be limited by absorber temperature, which would potentially allow new temperature operating regimes to be used.

It is clear that directionally selective surfaces have important implications to solar thermal applications, but at present there are few proposed methods for achieving directional selectivity in practice. Previous work has shown that the use of photonic crystals (periodic structures with periods on the length scale near the wavelength of light) can offer control over angular absorptance properties of a surface [55], as shown in Fig. 3.1a. While the focus of such investigations into photonic crystals has been improving the performance of PV solar cells [56, 57], the angular effect on thermal emittance indicates that such surfaces could potentially be used for solar-thermal systems as well [58, 59]. Rather than considering novel absorber surfaces, this thesis investigates a geometrical optics approach using an optical cavity. This offers a potential advantage in cost and simplicity, as no complicated microfabrication or exotic materials are required, and it is inherently a macro scale, device level technology. Traditional solar cavity receivers have been designed to minimize convective and radiative losses [60–62], however in these cavities no effort has been made to control the directional emittance of the cavity aperture (see Fig. 3.1b). The optical cavity proposed in this thesis surrounds the absorber with a reflective surface, such that radiation leaving the absorber from large angles is reflected back and can be reabsorbed. This effectively gives the absorber directionally dependent emittance (see Fig. 3.1c).

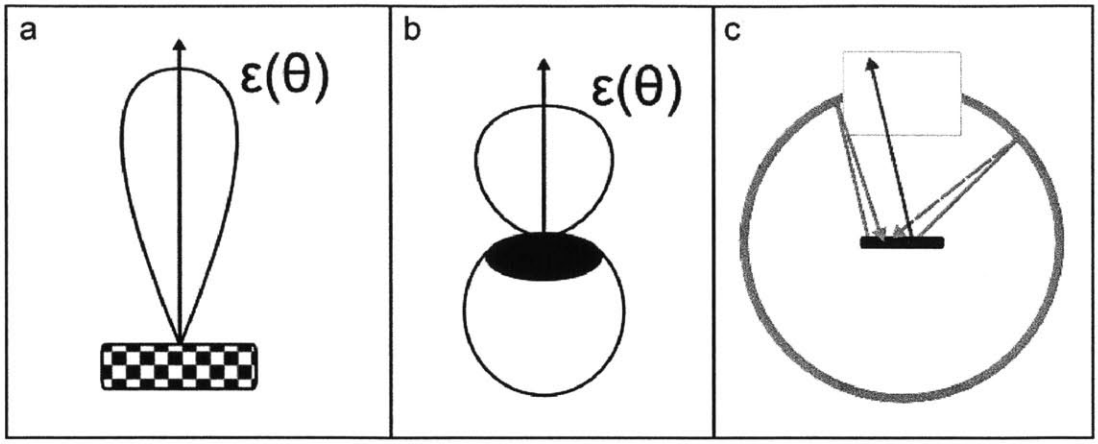

Figure 3.1 Comparison of different solar receivers and directional emittance strategies: a) photonic crystal has angularly dependent emissivity, which could be tailored so that emission only happens at small angles b) traditional solar cavity receivers do not focus on directional selectivity, aperture is effectively Lambertian c) new proposed optical cavity reflects rays emitted at large angles back to the absorber, therefore having effective directional emittance

In essence the optical cavity reduces losses by reflecting radiative back to the absorber, which is the function of a radiation shield. The idea of using a radiation shield to reduce radiative losses is not new by any means [28, 63]. The challenge in using radiation shields with the absorbers for solar-thermal applications is that for a radiation shield to be effective, it should cover the radiating surface. For a solar absorber, this would block incoming solar radiation, rendering the absorber ineffective. Instead, the proposed optical cavity relies on radiation being specularly reflected back to the absorber using clever geometry. If the cavity is properly designed (which will be discussed in more detail in section 3.2) a small aperture in the cavity will allow sunlight to strike the absorber unimpeded, while radiation from the absorber not directed towards the aperture is reflected back and reabsorbed. Since there are less radiative

losses at larger angles (the aperture is normal to the surface) the absorber effectively has directional radiative properties.

While both the photonic crystal and the proposed cavity here both lead to directionally dependent behavior, there are some important differences to note. The photonic crystal has an advantage in that it has directionally selective surface properties which are constant across the entire surface of the absorber. By contrast, the absorber in the optical cavity has effective directionally selective properties given by the cavity. Its surface is not inherently directionally selective, and different areas on the absorber will be affected by the cavity slightly differently. An advantage of the optical cavity system is that the temperature stability of the absorber is independent of the directional selectivity of the system, since the reflective cavity walls do not need to be at elevated temperature. If photonic crystals were used as absorbers, they would need to be at high temperature for efficient heat engine operation, so temperature stability of the photonic crystal would be a concern.

While the absorber in the proposed optical cavity has directional properties, it cannot be easily described using the directional emissivity as is used in equation (3.2) . This is because not all points on the absorber will have the same dependence on direction (e.g., two of the rays in Fig. 3.1c are emitted at the same angle at different locations: one escapes through the aperture while one is reflected back). Instead of the emittance from the absorber being described by a directional emittance ϵ', the hemispherical emittance from the absorber can be described by an effective emittance ϵ^*. Effective emittance can be understood as the emittance the absorber would need to have in the absence of the cavity to result in equivalent radiative losses.

It is trivial to calculate the radiative losses Q_{loss} from the absorber in the absence of the cavity using the Stefan-Boltzmann law [24]:

$$Q_{loss} = A\sigma\epsilon_{abs}(T_H^4 - T_{amb}^4) \tag{3.3}$$

We expect that when the cavity is introduced, there is a new radiative loss Q_{loss}^* which is less than Q_{loss}. The effective emittance can be calculated from the new radiative loss by:

$$\epsilon^* = \frac{Q_{loss}^*}{A\sigma(T_H^4 - T_{amb}^4)} \tag{3.4}$$

When the effective emittance is known (possibly as a function of hot side temperature, due to change in the emitted spectrum) for a given cavity, it greatly simplifies further analysis of the overall system. In coupling the absorber to the TEG and the rest of the system, radiative losses can be considered simply by using the cavity effective emittance, rather than continuing to consider the complexities of reflections within the cavity. Thus, the effective emittance of the absorber might be considered the figure of merit for the optical cavity. However, small apertures decrease effective emittance but could limit overall system efficiency by limiting the concentration ratio of sunlight on the absorber, so effective emittance is not the sole consideration of cavity design in overall performance (this will be discussed in more detail in section 4.7).

3.2 Geometries of the optical cavity

The keys to an effective optical cavity are having high specular reflectivity for the reflecting surface and choosing a geometry which will reflect radiation from the absorber back to the absorber in a minimum number of reflections. It is worth distinguishing between 2-D and 3-

D geometries for cavity design. Here 2-D refers to a system that could be extended to an arbitrary length in the depth direction (such as trough systems in current solar technologies) and would only be able to concentrate incoming solar radiation in one axis. 3-D refers to situations where all dimensions are defined (as in dish systems) and such systems can concentrate incoming solar radiation in both transverse axes. It should be noted that in certain cases axial propagation needs to be considered in 2-D systems, so the geometry cannot be treated as truly two dimensional [64]. The axial component of ray propagation can increase the travel distance through the cavity medium or amplify errors that arise from reflecting surface roughness or imperfections. For the investigation of this proposed optical cavity, the radiative propagates through vacuum, which is non-participating, and the reflecting surfaces are treated as perfectly smooth. Therefore the treatment is truly two dimensional, and axial propagation does not need to be considered.

The simplest geometry which has our desired property is a circular cylindrical cavity for a 2-D system. Radiation emanating from the center of a circle will reflect back to the center of the center simply by the construction of a circle: the normal of any point on the circle points to its center. Therefore if an absorber is placed at the center of a circular cylinder it follows that the emitted radiation (if reflecting specularly) will return to the absorber. This works perfectly if the absorber is an infinitesimal point, however once the absorber has some finite width, not all radiation will return in one reflection. At some large angles, emitted radiation will reflect multiple times inside the cavity before returning to the absorber see Fig. 3.2. Since real surfaces will not have perfect reflection, each additional reflection degrades performance, as more radiation is absorbed by the cavity walls rather than reabsorbed by the absorber surface.

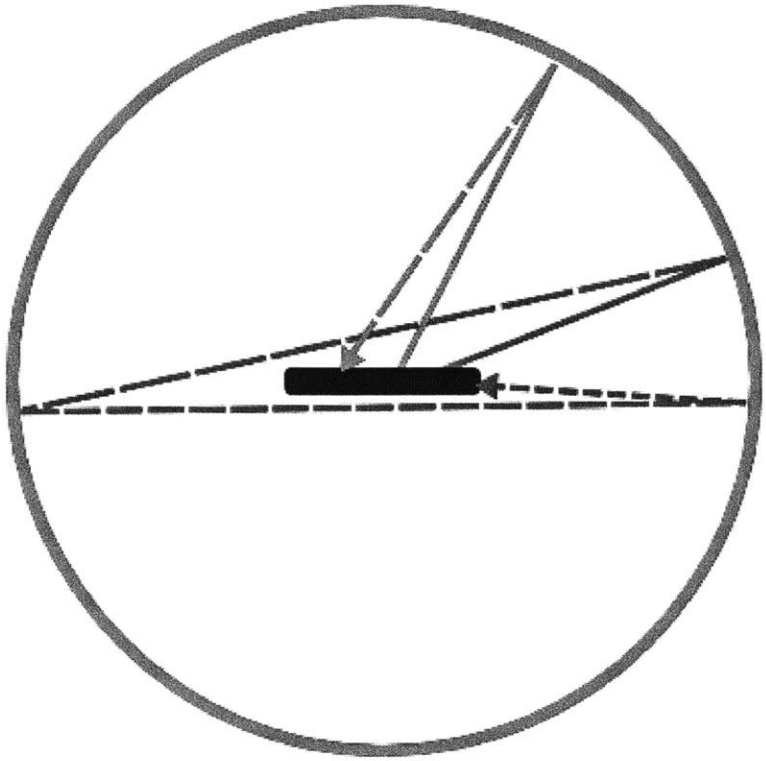

Figure 3.2 Diagram of circular cavity reflection behavior: most rays should return to absorber in one reflection, but some rays reflect off cavity walls multiple times before returning to the absorber

The multiple reflections of radiation emitted by a finite absorber before returning can be avoided through using a more elegant cavity geometry. An ellipse, described by

$$\left(\frac{x}{a}\right)^2 + \left(\frac{y}{b}\right)^2 = 1 \tag{3.5}$$

with a the semi-major axis and b the semi-minor axis, is the locus of points with sum of distances to two points being constant. These points are called the foci of the ellipse, and are given by

$$f = \sqrt{a^2 - b^2} \tag{3.6}$$

where f is the distance between a focus and the center of the ellipse. By this construction, an elliptical reflector has the property of reflecting all light from one focus to its other focus (see Fig. 3.3), with incident and reflected angles being equal by the law of reflection [65].

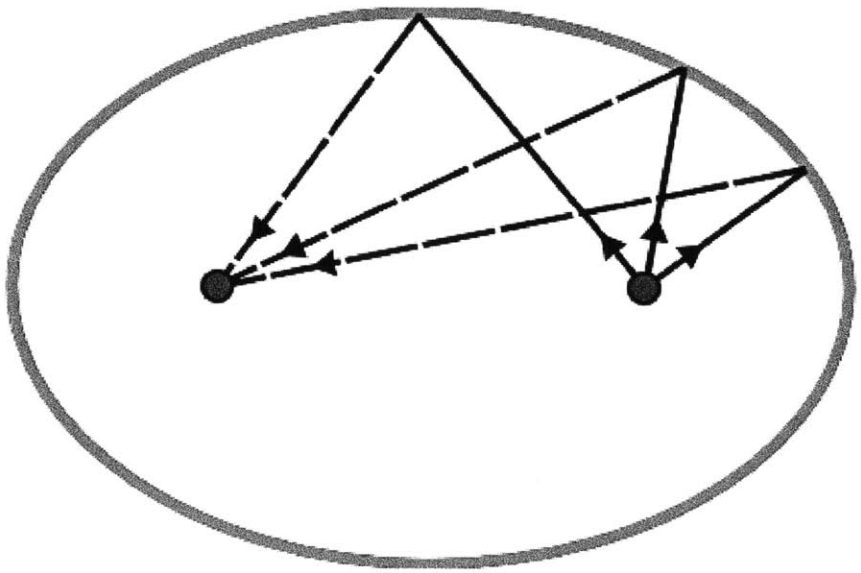

Figure 3.3 Reflecting behavior of ellipse: all rays emitted from one focus are reflected to the other focus

Let us consider using an elliptical cylindrical cavity with the absorber spanning the foci of the ellipse. The ellipse's reflecting property indicates that at any point along the ellipse, the angle between the normal and each edge is equal. This means that any ray striking a point on the ellipse from a smaller angle will reflect from that point at that same smaller angle. The absorber only spans angles smaller than the angles formed with the edges, so radiation emitted from any point on the absorber will reflect back to the absorber in one reflection (see Fig. 3.4). The emitted radiation returning in one reflection indicates that the elliptical cavity gives ideal

performance and maximizes reabsorbed radiation. Due to this behavior, and the fact that solar radiation only needs to be absorbed on one side of the absorber, in practice a full elliptical cavity need not be used. Instead a half ellipse can be used, as shown in Fig. 3.5. This half cavity can be used for circular cavities as well, although reflections from the bottom of the cavity will slightly degrade performance.

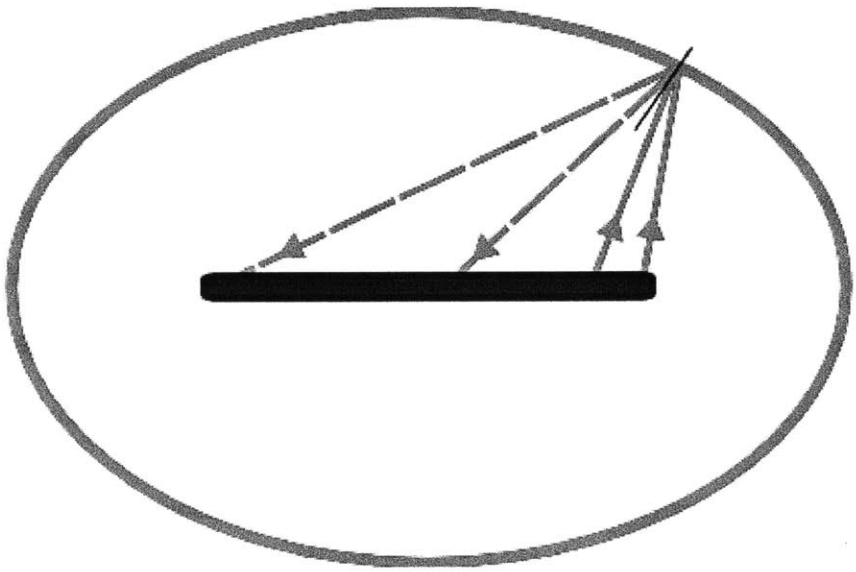

Figure 3.4 Ideal reflecting behavior of elliptical cavity: all rays emitted from the absorber will return to the absorber in a single reflection

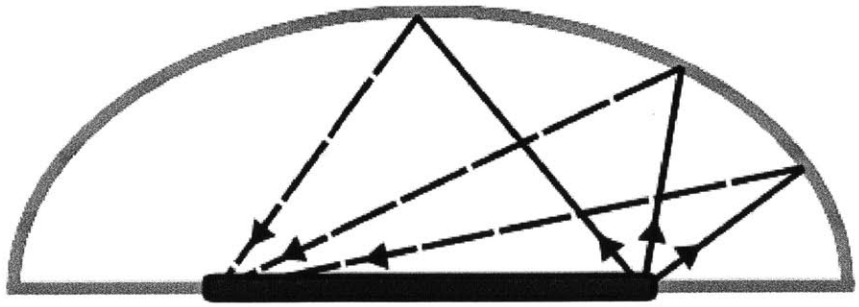

Figure 3.5 Diagram illustrating half cavity: since all rays return to the absorber in a single reflection, the bottom half of the cavity is not necessary

Both the circular and elliptical cylindrical cavities have equivalent geometries in 3-D with comparable performance. The analog for the circular cylinder in 3-D is a spherical cavity. Similar to the circular cylinder, this system performs perfectly in the case of a point absorber, but an absorber of finite width leads to unwanted multiple reflections. The analog for the elliptical cylinder is an ellipsoid. The equation for the surface of an ellipsoid is given by Eq. (3.7) .

$$\left(\frac{x}{a}\right)^2 + \left(\frac{y}{b}\right)^2 + \left(\frac{z}{c}\right)^2 = 1 \tag{3.7}$$

where a, b and c are the semi-principle axes. The particular analog to the elliptical cylinder of interest is an oblate ellipsoid, for which $a = b$ and $a > c$. In this case, a is the analog to the semi-major axis and c is analog to the semi-minor axis. Similar to the elliptical cylinder case, the absorber radius r_{abs} should be set by

$$r_{abs} = \sqrt{a^2 - c^2} \tag{3.8}$$

When the absorber radius is set by Eq. (3.8) , which is equivalent to spanning the foci in 2-D, the same ideal performance results. Any radiation emitted from the absorber will return back to the absorber in one reflection.

The interested reader is encouraged to investigate this mathematically, however only an intuitive approach will be outlined here. It is possible to show why this ideal performance occurs for the 3-D case with relative ease given an understanding of the 2-D case. Consider a differential area element on the ellipsoid surface. The absorber is a circle, but if it is projected onto a plane perpendicular to the differential area element, it becomes an ellipse (see Fig. 3.6). If the normal vector to the differential area element passes through the center of the projected

ellipse, then due to the law of reflection, any radiation from the edge of the projected ellipse striking the differential area element will be reflected to the opposite edge of the projected ellipse. The normal vector is trivially in the center of the ellipse in the horizontal direction (i.e., not to the "left" or "right" of the center by the area element's perspective) due to symmetry. We can argue that the normal vector is in the center of the ellipse in the vertical direction because it must be in order for radiation from the closest point on the absorber to reflect to the furthest point on the absorber, and we know this behavior to be accurate from the 2-D case. Since this ellipse is a projection of the absorber, it follows that any radiation from a point on the edge of the absorber will return to the edge of the absorber in a single reflection. Any radiation from within the absorber will form a smaller angle with the reflecting surface, and thus will be reflected to a point within the boundary of the absorber. Since our differential reflecting area element was chosen arbitrarily, this is true of the entire reflecting surface, so the ideal reflecting behavior is maintained for all points and all directions on the absorber.

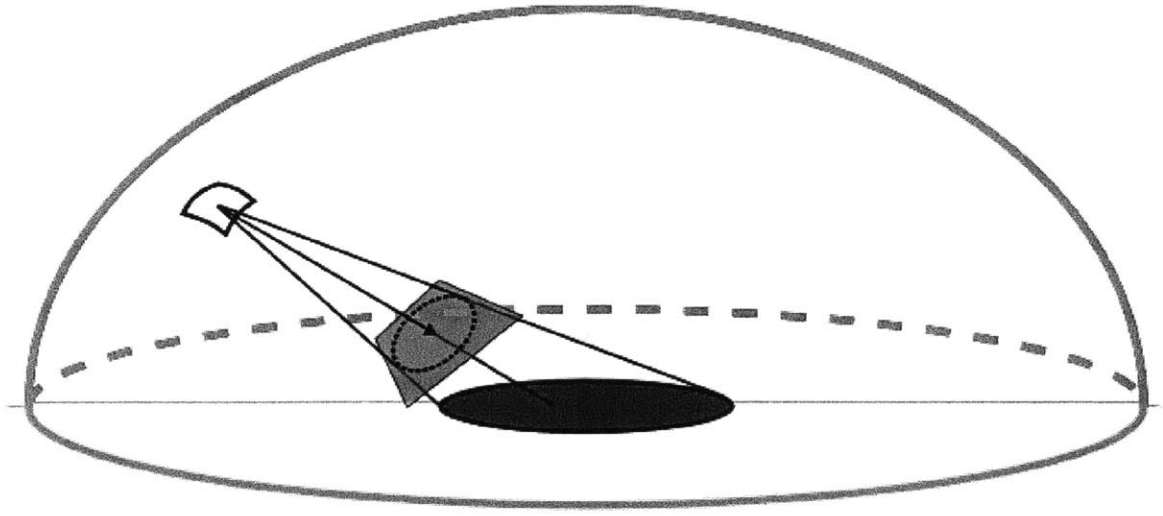

Figure 3.6 Diagram illustrating ideal ellipsoidal cavity reflecting behavior: surface normal points through the center of absorber's projection onto a normal plane

While it will not be explored in depth in this thesis, the same ideal reflective behavior can be achieved for tri-axial ellipsoids (that is, ellipsoids with three distinct semi-axes lengths). For these cases, the absorber will be ellipsoidal rather than circular. If the tri-axial ellipsoidal cavity is defined by semi-axes a_{cav}, b_{cav}, and c_{cav}, then the absorber should be defined by semi-axes a_{abs} and b_{abs} such that $a_{abs} = \sqrt{a_{cav}^2 - c_{cav}^2}$ and $b_{abs} = \sqrt{b_{cav}^2 - c_{cav}^2}$. The a_{abs} semi-axis and a_{cav} semi-axis should be aligned. An example of an application where such an arrangement could be beneficial is if different tracking requirements for the North-South and East-West directions were desired.

The nomenclature used to describe the different cavity geometries varies slightly for the circular versus ellipsoidal cases as well as the 2-D versus 3-D cases. Figure 3.7 shows the symbols used to define absorber size and cavity size for each geometry. In the circular and spherical geometries, cavity radius is given by r_{cav} whereas in the elliptical and ellipsoidal geometries, cavity size is given by the ellipse semi-major axis a. For the 2-D circular geometry the absorber size is given by its half width w_{abs}. In the 2-D elliptical geometry the absorber size is given by the location of the ellipse focus f. For both 3-D geometries the absorber size is given by the absorber radius r_{abs}.

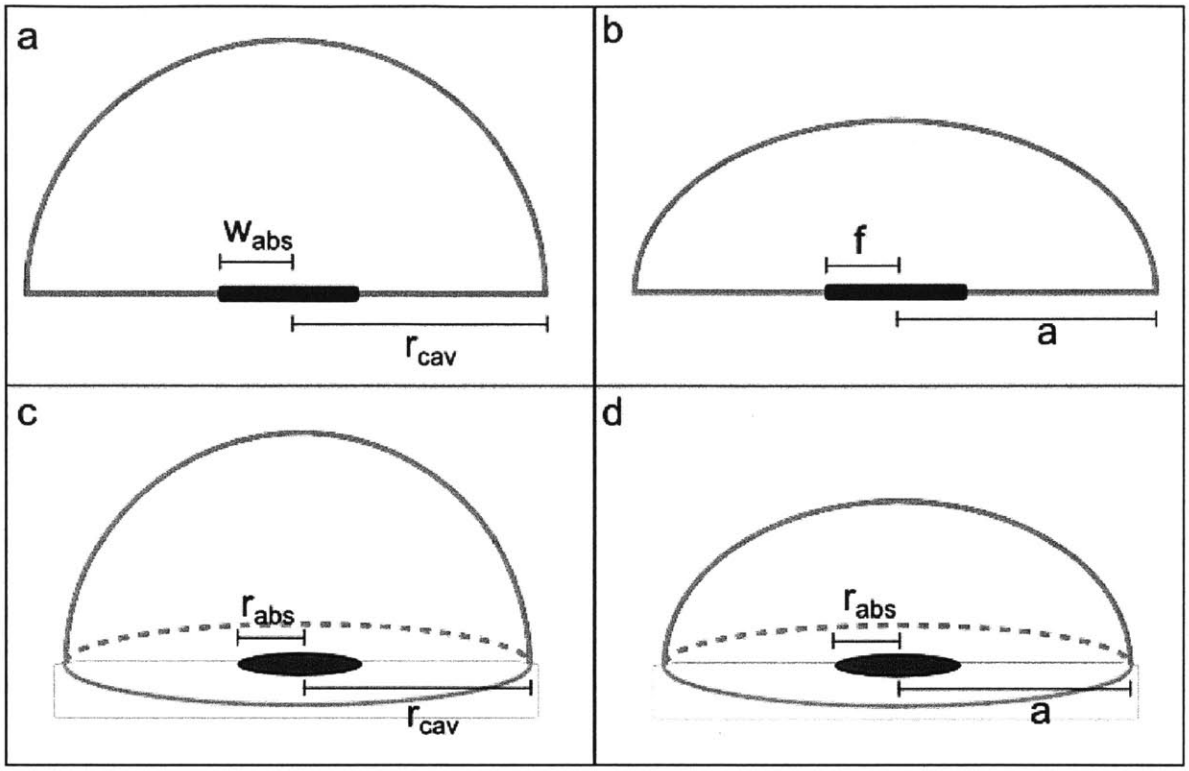

Figure 3.7 Nomenclature for cavity sizing, giving symbols for absorber size and cavity size: a) 2-D circular cavity b) 2-D elliptical cavity c) 3-D spherical cavity d) 3-D ellipsoidal cavity

In exploring geometry, it is also important to consider the aperture in the cavity which allows sunlight to reach the absorber. Up to this point, the optical cavities have been treated as fully enclosed rather than having an aperture. The aperture is important to the performance of the cavity because any radiation from the absorber directed towards the aperture will be lost (it has no chance of being reflected back to the absorber to be reabsorbed). For the sections to follow apertures of various sizes will be considered. The importance of aperture size for device design and overall system efficiency will be discussed in section 4.7.

In describing the size of the aperture, we use an "opening angle" Ψ between the absorber and aperture. Opening angle is defined as the angle between the absorber normal at its edge and a

vector connecting the absorber edge and aperture edge (see Fig. 3.8). The aperture size is described by the cavity's opening angle because this determines what optical concentration will be achievable [54], which is important to calculating opto-thermal efficiency (see section 4.7.1 for further discussion).

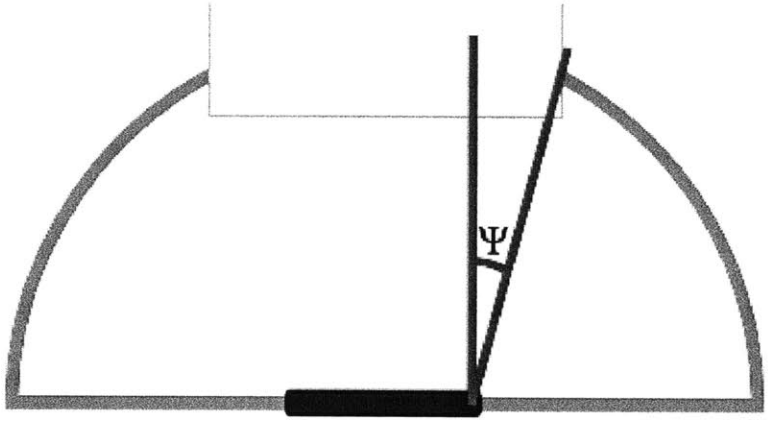

Figure 3.8 Diagram illustrating opening angle Ψ

Since smooth surfaces are assumed, a cavity's geometry is fully defined with three parameters being known: the cavity size, the absorber size and the opening angle. Since surface roughness is not being considered in this investigation, the absolute sizes of the geometry are not important, only the relative size of the absorber and cavity. Thus for the purposes of this thesis, a cavity has a fully defined geometry with two parameters known: the cavity size ratio and the opening angle, where cavity size ratio is the cavity size parameter divided by the absorber size parameter (e.g., r_{abs}/w_{abs} for the 2-D circular case).

3.3 Modeling optical cavity performance

We are interested in being able to predict how the effective emittance is reduced for different cavity parameters in order to inform design decisions. Through development of a model

to predict performance, significant time and effort can be saved during physical experimentation with the cavity, to determine which cavity designs are worth investigating.

3.3.1 Analytical ellipse performance

The ideal reflection properties of the elliptical cavity lend themselves well to the calculation of effective emittance, so elliptical cavities will be considered first. The simplest case to analyze is a blackbody absorber in an elliptical cavity with no aperture (this would be useless for a solar-thermal system, but is still valuable for illustrative purposes). Radiation from the absorber is fully reabsorbed after one reflection from the cavity walls. The energy lost is simply the radiation emitted by the absorber times the absorptance of the cavity walls. In this case, the effective emittance is then simply unity minus the specular reflectance of the cavity walls. If we assume that all reflectance from the cavity walls is specular, in this simple case the effective emittance of the absorber can also be expressed as the emittance of the cavity walls. It should be noted that for this application the ratio of absorber area to cavity area is small, such that any radiation diffusely reflecting off the cavity walls can be assumed to eventually be lost. For further treatments in this thesis, cavity wall emittance (also referred to as mirror emittance in this thesis) will be used interchangeably with unity minus specular reflectance, as absorptance and diffuse reflectance both result in radiation being lost to the cavity.

The more practical case of a black absorber in an elliptical cavity with an aperture is still simple to analyze. In this case, all the radiation directed from the absorber to the aperture is lost, whereas radiation directed towards the cavity walls is reabsorbed after one reflection as before. The effective emittance of the absorber can then be expressed as

$$\epsilon^* = F_{abs,ap} + F_{abs,cav}\epsilon_{cav} \tag{3.9}$$

where $F_{abs,ap}$ is the view factor from the absorber to the aperture, $F_{abs,cav}$ is the view factor from the absorber to the cavity walls and ϵ_{cav} is the emittance of the cavity walls.

While calculating view factor is sometimes a complicated endeavor, for the geometries we are interested in it is rather simple. The view factor from the absorber to the aperture can be calculated using Hottel's string rule in the 2-D case [66], and is thus given by

$$F_{abs,ap} = \frac{\sqrt{(f+x_0)^2+y_0^2} - \sqrt{(f-x_0)^2+y_0^2}}{2f} \tag{3.10}$$

where f is the absorber half length, and x_0 and y_0 denote the position of the edge of the aperture, with the origin at the center of the ellipse. For the 3-D case, the view factor is between two coaxial disks, and has been calculated previously [24]:

$$F_{abs,ap} = \frac{1}{2}\left(\left[1+\frac{1+(x_0/z_0)^2}{(r_{abs}/z_0)^2}\right] - \sqrt{\left[1+\frac{1+(x_0/z_0)^2}{(r_{abs}/z_0)^2}\right]^2 - 4\left(\frac{x_0}{r_{abs}}\right)^2}\right) \tag{3.11}$$

where r_{abs} is the absorber radius, and x_0 and z_0 denote the position of the edge of the aperture on the x-z plane. The absorber is not concave, so the sum of view factors must be unity [28]. The view factor from the absorber to the cavity walls can then be found simply by

$$F_{abs,cav} = 1 - F_{abs,ap} \tag{3.12}$$

If the emittance of the absorber is ϵ_{abs} rather than the absorber being black, the effective emittance of the system will naturally be lower. In this case, emitted radiation may have multiple reflections between the absorber surface and cavity walls before being absorbed by either surface

or leaving through the aperture. This multiple reflection behavior leads to the effective emittance being the sum of a geometric series. If the reflection from the absorber is treated as diffuse, effective emittance is given by

$$\epsilon^* = \epsilon_{abs}\left(F_{abs,ap} + \epsilon_{cav}F_{abs,cav}\right)\sum_{n=0}^{\infty}\left[(1-\epsilon_{cav})(1-\epsilon_{abs})F_{abs,cav}\right]^n \tag{3.13}$$

Evaluating the geometric series yields:

$$\epsilon^* = \frac{\epsilon_{abs}\left(F_{abs,ap} + \epsilon_{cav}F_{abs,cav}\right)}{1 - F_{abs,cav}(1 - \epsilon_{cav} - \epsilon_{abs} + \epsilon_{cav}\epsilon_{abs})} \tag{3.14}$$

It should be noted that this treatment assumes that all points on the absorber have the same view factor to the aperture, which will not be true in reality. This approximation should not lead to significant error except for systems with very large absorbers relative to the cavity size. The specular case is much more difficult to treat analytically, as there is no easy way to determine how many times radiation will reflect inside the cavity before leaving through the aperture. The selective surfaces used in practice are very smooth and should have minimal diffuse reflection, so the lack of an analytical solution is unfortunate. The diffuse case still gives a decent approximation, and thus will be used here. Its accuracy will be compared to the specular case when explored with ray tracing simulations in section 4.2.

Equation (3.14) can be rewritten as:

$$\epsilon^* = \epsilon_{abs}\left(\frac{F_{abs,ap}}{1 + F_{abs,cav}(\epsilon_{cav} + \epsilon_{abs} - \epsilon_{cav}\epsilon_{abs} - 1)} + \frac{\epsilon_{cav}F_{abs,cav}}{1 + F_{abs,cav}(\epsilon_{cav} + \epsilon_{abs} - \epsilon_{cav}\epsilon_{abs} - 1)}\right) \tag{3.15}$$

which offers more insight into the effect of the cavity. The expression in parentheses in Eq. (3.15) is a value less than one corresponding to the reduction of the effective emittance of the absorber due to the cavity. For example, if the parenthetical expression evaluates to 0.25, then the effective emittance of the cavity system is 25% of the absorber's emittance. The losses are separated into two terms. The first term in parentheses is radiation lost through the aperture, and can be reduced most directly by making the aperture smaller. Note that while making the aperture smaller reduces effective emittance, it also reduces the allowable concentration ratio, so a balance must be found (this will be discussed in more detail in section 4.7). The second term in parentheses is radiation absorbed by the mirror walls. This reduction is primarily a function of the ratio of cavity wall emittance to absorber emittance. This makes intuitive sense, as the cavity walls need to be much more reflective than the absorber surface in order for the cavity to have a significant effect. If the ratio $\epsilon_{cav}/\epsilon_{abs}$ is close to one (or greater than one), then the cavity walls absorb much of the radiation before it has a chance to be reabsorbed by the absorber. This can be seen directly in the case where $F_{abs,cav}$ is set to one (no aperture) and the second term in parentheses becomes:

$$\frac{\frac{\epsilon_{cav}}{\epsilon_{abs}}}{\frac{\epsilon_{cav}}{\epsilon_{abs}} + 1 - \epsilon_{cav}} \tag{3.16}$$

The analysis pursued above offers a simple equation to predict effective emittance (Eq. (3.15)). Directions for improvement in effective emittance suggested by Eq. (3.15) are quite obvious: effective emittance is reduced with reductions in absorber emittance and cavity wall emittance. The ratio $\epsilon_{cav}/\epsilon_{abs}$ is also particular important and should be made as small as possible. Thus if

ϵ_{abs} can already be made very small (for example, through a specularly selective absorber surface) the cavity will not be able to reduce effective emittance much further, and using the cavity may not be worth pursuing. Effective emittance can also be reduced by making the view factor from the absorber to the aperture smaller, but effects on overall device performance must be considered as well, and are covered in section 4.7.

3.3.2 Ray tracing simulations

Analysis of elliptical/ellipsoidal cavity geometries is made simple by the ideal behavior that any radiation from the absorber will return in a single reflection. This is not the case for circular/hemispherical cavities or for elliptical/ellipsoidal cavities with some distortion or imperfections, which are still of interest. Circular and hemispherical cavities are of interest despite their lack of ideal reflecting behavior because they are much more prolific in the manufacturing space, and it is possible to find stock pieces that could be used to build such cavities. Even when the ideal geometry can be used, imperfections such as misalignment between the absorber and cavity could lead to non-ideal behavior.

In these non-ideal cases, it is prohibitively complex to derive an analytical expression for effective emittance. A more practical solution is to use ray tracing methods to predict cavity performance. Ray tracing is a Monte Carlo method which uses many simulated "rays" to in this case predict average behavior of radiation exchange between different surfaces [67]. In ray tracing, each ray represents a bundle of light with a given wavelength, position and direction of propagation. With the geometry and radiative properties of the surfaces in the receiver system known, ray tracing can predict effective emittance by the following procedure (each step of the procedure will be explained in more detail following the numbered list):

1. Generate a large number (typically $\geq 10^6$) of rays at the absorber surface. Random numbers, along with known cumulative distribution functions (CDFs), are used to determine the following for each ray:
    - Wavelength
    - Position
    - Propagation direction
2. The rays are propagated until they intersect a surface
3. Based on the surface properties and random numbers, the rays are either:
    - Absorbed
    - Reflected specularly
4. Repeat steps 2 and 3 until all rays are absorbed
5. Count the rays absorbed by each surface to find effective emittance

The first step in ray tracing is to generate the rays. In order to understand how this is done, we will take a brief digression to discuss some concepts of probability and statistics. Consider a group of objects with at least one property which varies between the objects. For our example, we can consider a group of rays with different wavelengths. A probability density function (PDF) is a function describing the relative likelihood of the object to have a certain value of the property of interest [68] (see Fig. 3.9a). The integral of a PDF over a range of property values gives the probability that a randomly selected object will have its property value in that range. It follows then that the integral of a PDF over the entire range of possible values is one. For example, the PDF for ray wavelengths would be intensity given by Planck's law (Eq. (3.17)), scaled such that the integral over all wavelengths is unity. A cumulative distribution function (CDF) is a function that describes the likelihood of an object having a given property

value or lower. It thus goes from zero to one over the range of possible property values [68] (see Fig. 3.9b). The CDF for a given property and group of objects is given by the integral of the corresponding PDF. These concepts are important for generating the rays at the beginning of the simulation.

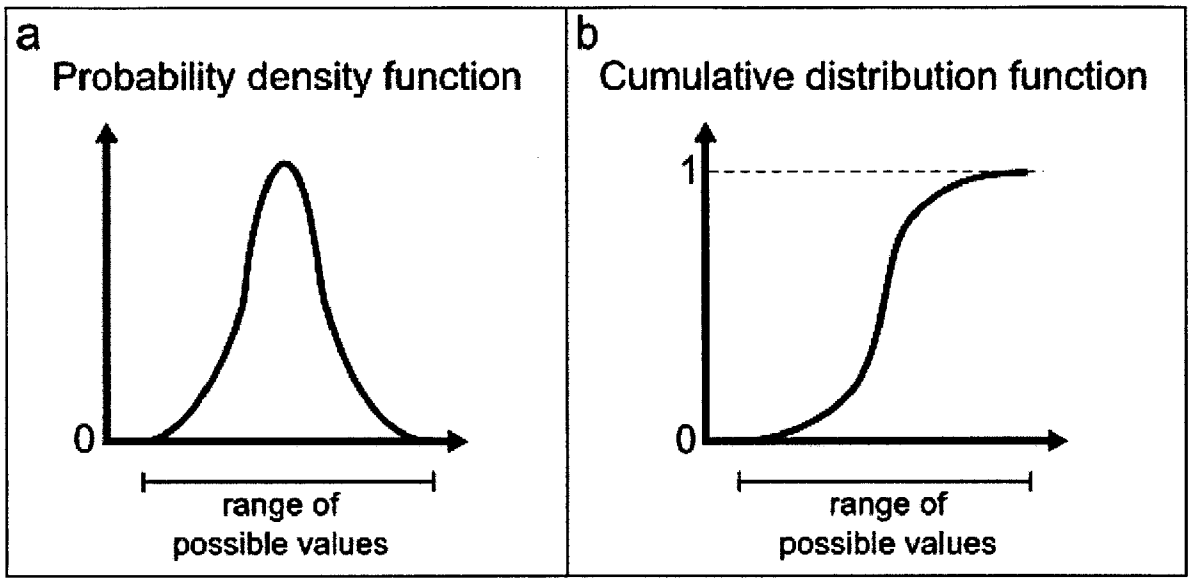

Figure 3.9 Important statistical functions for ray tracing: a) Probability density function (PDF) b) Cumulative distribution function (CDF)

Each ray that will be tracked needs a wavelength and a starting position and direction. These are determined using random number generation and CDFs. With known CDFs, properties can be chosen appropriately given a method for generating a random number evenly distributed from zero to one (a feature which is standard in programming packages). A random number is generated for each property of each ray, and the property value is assigned as the inverse CDF value of that random number (see Fig. 3.10). As mentioned previously, the CDF for wavelength can be obtained for a blackbody absorber by taking the integral of the scaled intensity as given by Planck's law:

$$E_\lambda(T,\lambda) = \frac{2\pi hc^2}{\lambda^5(e^{hc/\lambda k_B T} - 1)} \tag{3.17}$$

and is a function of the absorber temperature (hotter absorbers will tend to generate rays with shorter wavelengths).

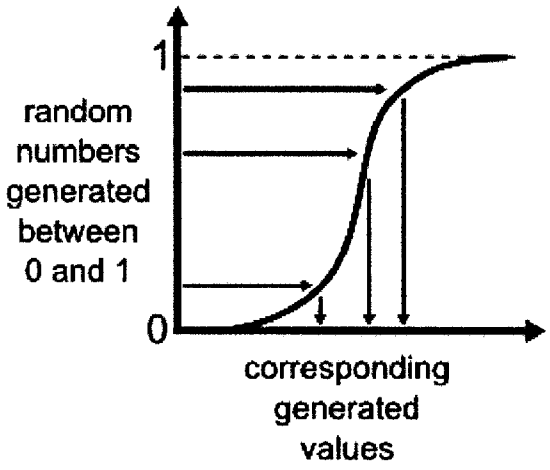

Figure 3.10 Diagram illustrating how intial values are generated in ray tracing simulations

If the absorber is a selective surface rather than a blackbody absorber, the intensity function given by Planck's law can be multiplied by the emissivity of the surface as a function of wavelength (this becomes the new PDF). The CDF for absorber position (that is, where on the absorber a ray originates from) depends on absorber geometry, and is simple to find if the absorber radiative properties are constant as a function of position. For a rectangular absorber, the PDFs are constant, so the CDFs are simply linear functions increasing from zero to one for the span of the absorber. For a circular absorber, the PDF is linear with radial position, so the CDF is simply a function proportional to radial position squared. The CDF for starting direction can be found from Lambert's cosine law for a Lambertian surface [28], in which case the PDF is simply $sin\phi cos\phi$ over the interval from zero to $\pi/2$, where ϕ is the azimuthal launching angle.

The polar launching angle is evenly distributed between zero and 2π, and thus trivial to generate. If the absorber surface is not Lambertian, the PDF for azimuthal launching angle can be modified by the directional emissivity, similar to how intensity as a function of wavelength is modified by spectral emissivity in generating wavelengths of rays.

For our application, there is a modification made to the procedure outlined above which simplifies the calculation but should not alter the outcome. Since the absorber is assumed to be isothermal, and the radiative spectrum from the absorber at its operating temperature is the only spectrum of interest, it is not necessary to determine the wavelength of rays. Instead the rays can be treated as spectrally homogeneous, and radiative properties can be calculated by integrating over said spectrum.

Once the rays have been generated, they are propagated until they intersect one of the relevant surfaces. The ray intersects a surface $\vec{s}$ at time t when

$$\vec{r}_0 + \vec{v}t = \vec{s} \tag{3.18}$$

is satisfied, with $\vec{r}_0$ being the ray starting position and $\vec{v}$ being the ray velocity. Equation (3.18) is used to find t for each surface, and whichever surface yields the smallest t (which is still greater than zero) is the surface that the ray encounters. The new position of the ray is found trivially by $\vec{r} = \vec{r}_0 + \vec{v}t$. In practice, the surface is described parametrically by $z = f(x, y)$ and t is found by solving the system of equations:

$$x = r_{x,0} + v_x t \tag{3.19}$$

$$y = r_{y,0} + v_y t \tag{3.20}$$

$$z = f(x, y) = r_{z,0} + v_z t \tag{3.21}$$

When the ray encounters a surface, there are three possibilities: it can be absorbed, reflected specularly or reflected diffusely. The radiative properties of the encountered surface are in general a function of the ray's wavelength and incident angle. A random number can be generated, and with the radiative properties known the random number can determine whether the ray is absorbed or reflected. If the ray is absorbed, it should be noted which surface it was absorbed by, but beyond that no longer needs to be tracked.

If the ray is reflected specularly, the new ray velocity vector forms an angle with the normal of the encountered surface which is equal to the angle formed between the normal and incident ray. The reflected velocity $\vec{v}_r$ can therefore be calculated by

$$\vec{v}_r = \vec{v}_i + 2\hat{n}(\vec{v}_i \cdot \hat{n}) \tag{3.22}$$

with $\vec{v}_i$ being incident velocity and $\hat{n}$ being the surface normal. If the ray is reflected diffusely, the new ray velocity is determined using randomly generated numbers and CDFs, in the same manner that direction is determined for the original rays leaving the absorber. As mentioned before, rays are assumed to reflect specularly in the simulations relevant to this thesis, as all surfaces in the cavity system are expected to be smooth.

Rays that are not absorbed have a new launching position and direction, and should be propagated until they intersect a surface. At this surface, a random number determines whether the rays are absorbed or reflected, and this process repeats until all rays have been absorbed. Once all rays are absorbed, counting the rays absorbed at each surface can yield the effective emittance, since each ray represents the same amount of energy. For the blackbody absorber case, effective emittance is given simply by

$$\epsilon^* = \frac{N_{tot} - N_{abs}}{N_{tot}} = 1 - \frac{N_{abs}}{N_{tot}} \tag{3.23}$$

where N_{tot} is the total number of rays generated for the simulation, and N_{abs} is the number of rays reabsorbed by the absorber. More rays being reabsorbed corresponds to better performance of the cavity, and the limiting case when $N_{abs} = N_{tot}$ (i.e. all rays end up reabsorbed) corresponds to a cavity with perfect performance and an effective emittance of zero. If the absorber is a selective surface with emittance ϵ_{abs} then the effective emittance is given by

$$\epsilon^* = \epsilon_{abs}\left(1 - \frac{N_{abs}}{N_{tot}}\right) \tag{3.24}$$

as the overall radiation emitted in the first place is reduced by the absorber emittance. For calculating effective emittance, all that is needed is the ratio of rays reabsorbed to the total number of rays. However, the number of rays absorbed by different sections of cavity wall or lost through the aperture can give insight into how to best improve the cavity performance. For example, if many rays are lost through the aperture, it may be worthwhile to reduce the aperture size, or if many rays are absorbed by the cavity walls, it may be worthwhile to use a more reflective surface material.

3.4 Summary

This chapter has introduced methods to predict the effective emittance of an absorber in the proposed optical cavity, which can vary with cavity geometry as well as cavity and absorber surface properties. For cavities with an elliptical geometry and a diffusely reflecting absorber, an analytical expression can be used to predict performance. For cavities with circular or spherical geometries or with specularly reflecting absorbers, a more time consuming ray tracing simulation

should be used to predict performance. In the following chapter, these methods will be used to examine the particular performance of various cavities.

Chapter 4 Optical Cavity Simulation Results and Discussion

Using the analytical expressions for elliptical geometries with a diffuse absorber or through the use of ray tracing simulations, covered in detail in chapter 3, we are able to predict the effective emittance of different cavity setups. These predictions are helpful in determining which cavity designs are the most effective and worth pursuing experimentally.

4.1 Analytical results for elliptical geometries

4.1.1 2-D elliptical geometries

There are a number of important parameters which determine specific effective emittance of an absorber cavity system. The characteristic values in Table 4.1 are used in the results for this section except when specifically noted otherwise. It is worth noting that absorber temperature is not listed as a parameter. This is because, as mentioned before, cavity performance is not dependent on absorber temperature (aside from the fact that absorber emittance may be a function of temperature).

Table 4.1 Parameters used for 2-D analytical model

Parameter	Symbol	Value
Cavity wall emittance	ϵ_{cav}	0.05
Absorber emittance	ϵ_{abs}	0.2
Opening angle	Ψ	5°
Cavity size ratio	a/f	10

Results for the 2-D case will be discussed first. For the characteristic values used in Table 4.1 the effective emittance of a 2-D elliptical cavity is 0.12. This shows a large reduction in emittance from 0.2, and would reduce the radiative loss to 60% of the loss which would be experienced in the absence of the cavity. For a blackbody absorber in the cavity, which is of interest because in high temperature applications selective surfaces may not be stable, the effective emittance is 0.23. While this is a relatively high emittance, it still represents a reduction in radiative losses to less than a fourth of the case without the cavity, a much more significant relative improvement in performance. To better understand this result and explore possible improvements, the effect of changing various parameters will be explored below.

For an elliptical cavity, the opening angle from the absorber to the aperture is particularly important. This is because in the elliptical case all radiation reaching the cavity walls is reflected back to the absorber, so there are minimal mirror losses. Figure 4.1 shows the effect of increasing opening angle on effective emittance for different absorber emittances. We expect that lower absorber emittances lead to lower effective emittances, and that larger opening angles lead to higher effective emittances, which are both shown to be the case. Larger absorber emittances are more sensitive to increase in aperture size, as the radiation directed out the aperture (for a given aperture size) can only be reduced by lowering absorber emittance. However, even with a low absorber emittance, aperture size is important: the effective emittance of the $\epsilon = 0.2$ system increases by over 50% from about 0.1 to 0.16 when the opening angle is increased from 2° to 20°. For the blackbody absorber case, the influence is even greater, with effective emittance almost tripling for the same change in aperture size.

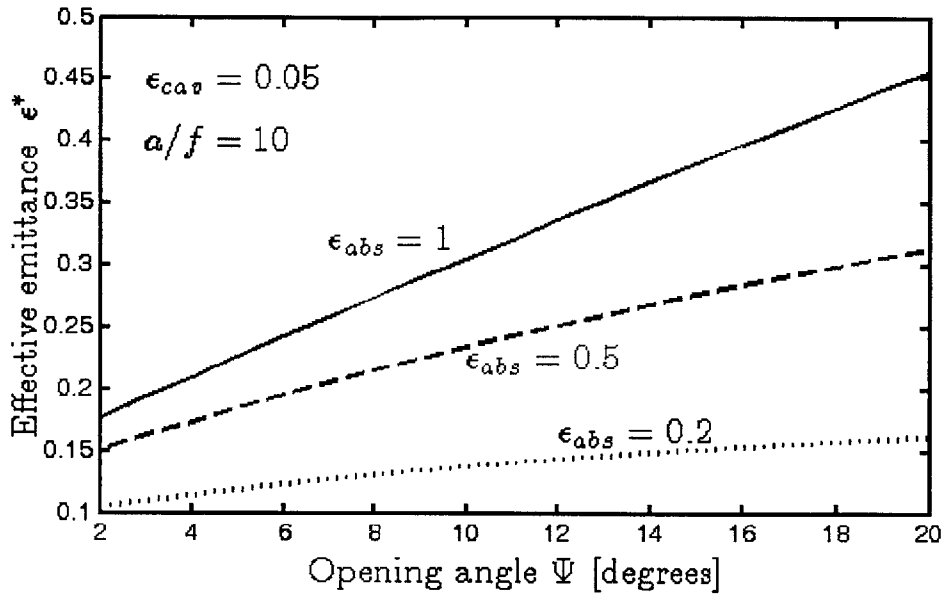

Figure 4.1 Analytical effective emittance results for varying opening angle for 2-D elliptical cavity. Different curves denote different absorber emittances

Mirror emittance is also an important factor, and as discussed earlier the cavity cannot successfully reduce effective emittance by a significant amount unless the ratio $\epsilon_{cav}/\epsilon_{abs}$ is kept low. Figure 4.2 shows the effect that mirror emittance ϵ_{cav} has on effective emittance for different absorber emittances. Again in this case, larger absorber emittances make effective emittance more sensitive to parameter changes, in this case ϵ_{cav}. For the $\epsilon_{abs} = 1$ and $\epsilon_{abs} = 0.5$ cases, effective emittance increases approximately linearly with ϵ_{cav}, with effective emittance growing about twice as fast for the $\epsilon_{abs} = 1$ case compared to the $\epsilon_{abs} = 0.5$ case. The $\epsilon_{abs} = 0.2$ case strays the furthest from linear behavior, as this is an example where the ratio $\epsilon_{cav}/\epsilon_{abs}$ is allowed to increase above one. For this case, the cavity is absorbing relatively more radiation than the absorber, so the overall effective emittance is beginning to asymptote at

$\epsilon^* = \epsilon_{abs}$. This confirms the argument presented earlier for a low mirror emittance relative to absorber emittance being important to cavity performance.

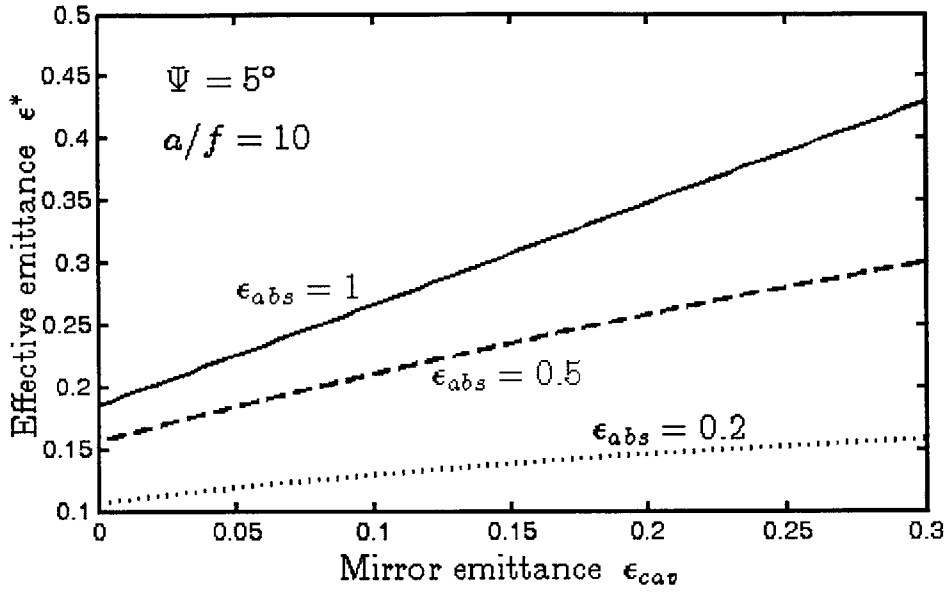

Figure 4.2 Analytical effective emittance results for varying mirror emittance for 2-D elliptical cavity. Different curves denote different absorber emittances

For the elliptical case, even with the ideal behavior where all radiation is reflected back to the absorber in a single bounce, the size of the cavity can have an effect on performance when the aperture opening is set by an opening angle. With opening angle held constant, a larger cavity (corresponding to a larger cavity ratio a/f where a is semi-major axis and f is the absorber half-width as given by Eq. (3.6)) will have a smaller view factor from the absorber to aperture $F_{abs,ap}$, yielding improved performance. The effect of cavity size on effective emittance is shown in Fig. 4.3 for various opening angles. Different opening angles are affected by cavity size very similarly. Cavity performance is sensitive to size up until $a/f \approx 30$ after which the trend

flattens out. Since our standard value of $a/f = 10$ is in the range where effective emittance still has sensitivity to size, this indicates that performance could be improved if one was willing to use a bigger cavity.

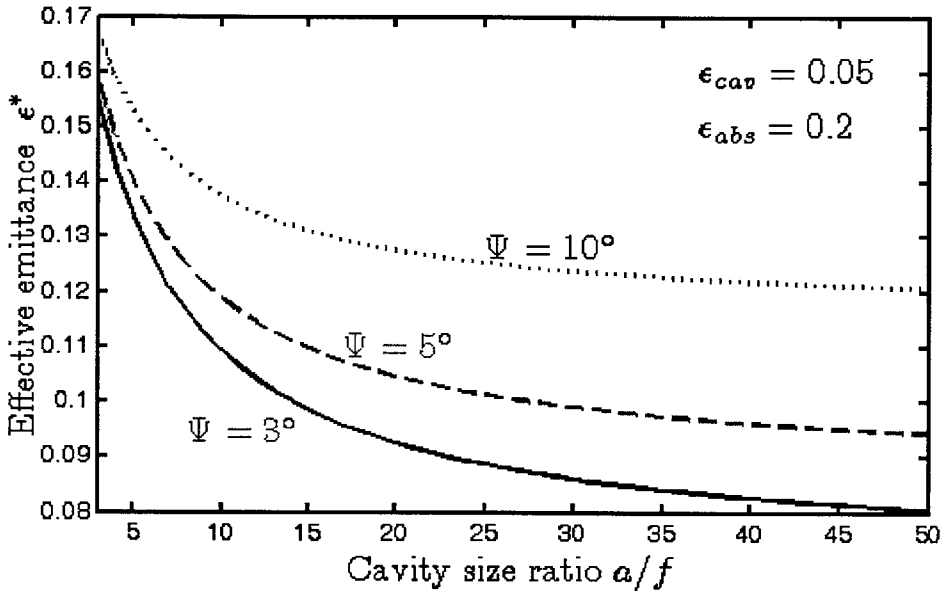

Figure 4.3 Analytical effective emittance results for varying cavity size ratio for 2-D elliptical cavity. Different curves denote different opening angles

4.1.2 3-D ellipsoidal geometries

The 3-D case has lower effective emittances in general due to the fact that it is able to contain radiation in two axes rather than just a single axis. This improvement comes from the fact that in the 3-D, the view factor from the absorber to the aperture is significantly smaller, since they are both disks rather than parallel infinitely extending plates. This is analogous to higher concentration ratios being achievable in two axes (e.g., dish) concentration systems than in one axis (e.g., trough) concentration systems. Using the standard values in Table 4.2, the

effective emittance of a 3-D ellipsoidal cavity is slightly above 0.062, representing a reduction of about 50% from the standard 2-D elliptical cavity case. For a blackbody absorber in an ellipsoidal cavity, the effective emittance is 0.083, a reduction of over 60% from the 2-D case, and a reduction of over 90% in radiative losses from the cavity-less case. The standard values used for the 3-D case are the same as the 2-D, although now the cavity size ratio is defined using the absorber radius r_{abs} as defined in Eq. (3.8) rather than the absorber half width f.

Table 4.2 Parameters used for 3-D analytical model

Parameter	Symbol	Value
Cavity wall emittance	ϵ_{cav}	0.05
Absorber emittance	ϵ_{abs}	0.2
Opening angle	Ψ	5°
Cavity size ratio	a/r_{abs}	10

Results for the 3-D case show similar trends to the 2-D case in terms of varying parameters, with the 3-D case performance tending to be more sensitive to changes in parameter values. The effect of opening angle on performance is even more pronounced in the 3-D case, due to the fact that the aperture is growing in two dimensions rather than just one as in the 2-D case. Effective emittance as a function of opening angle is shown in Fig. 4.4 for various absorber emittances. Changing opening angle from 2° to 20° more than triples the effective emittance of a blackbody absorber in this case, and the less sensitive $\epsilon_{abs} = 0.2$ case still more than doubles the effective emittance for the same increase in opening angle.

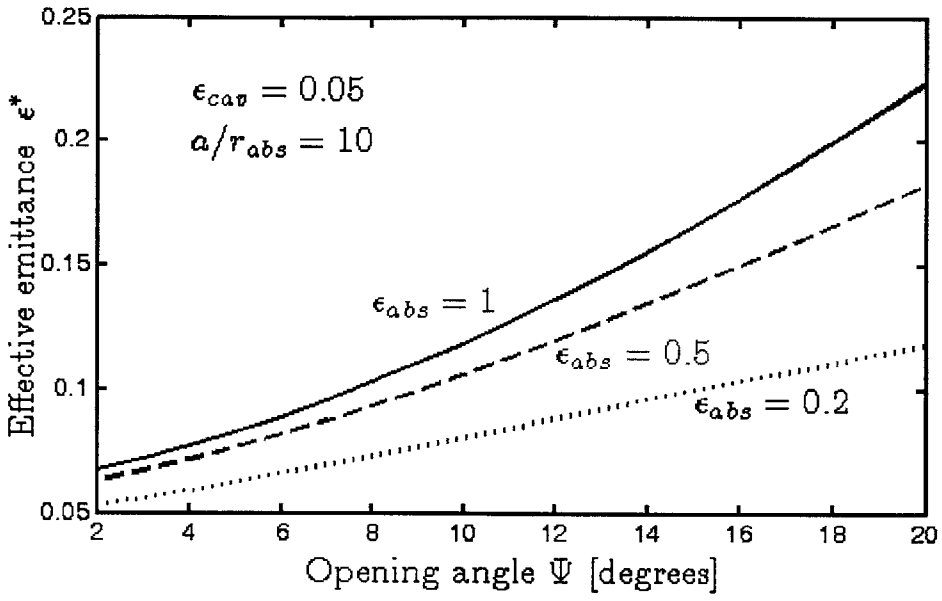

Figure 4.4 Analytical effective emittance results for varying opening angle for 3-D ellipsoidal cavity. Different curves denote different absorber emittances

Mirror emittance is also extremely important in the 3-D case. This is due to the relatively small view factor from the absorber to aperture, as previously discussed. Since a great majority of the radiation from the absorber is directed towards the cavity walls, it becomes more important that the mirrored cavity walls are not absorptive. This can be seen in Fig. 4.5 which plots ϵ_{cav} against effective emittance for various absorber emittances. The trend here is very similar to the 2-D case, with higher slopes due to the higher sensitivity to ϵ_{cav} because of the large $F_{abs,cav}$ term in the 3-D case. It is also worth noting how similar the effective emittances are for different absorber emittances for small mirror emittances. This similarity is due to the case of a highly reflective mirror wall giving radiation many chances to escape through the aperture. In the blackbody case, there is a large amount of initially radiated energy, but it is all captured within one reflection. For the selective surface case, less radiation is given off to begin

with, but many internal reflections give that radiation more chances to be completely lost to the aperture of the cavity.

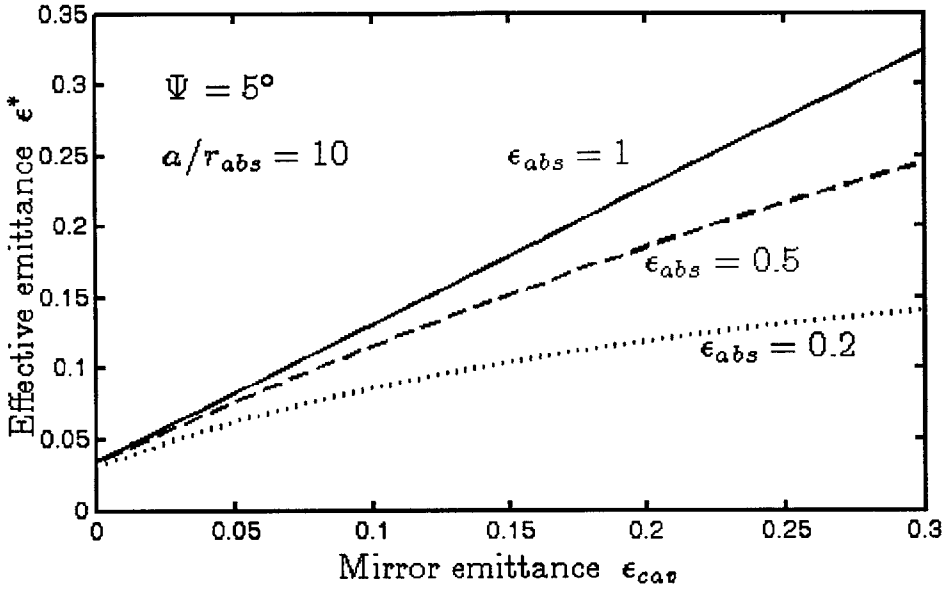

Figure 4.5 Analytical effective emittance results for varying mirror emittance for 3-D ellipsoidal cavity. Different curves denote different absorber emittances

The effect of cavity size on performance in the 3-D case is similar to the 2-D case. Effective emittance as a function of cavity size is shown in Fig. 4.6 for various opening angles. Effective emittance is sensitive in a shorter range for the 3-D, with performance improving with increasing cavity size until around $a/r_{abs} \approx 15$, after which larger values give diminishing returns. There is thus still a small amount of improvement to be gained by making a larger cavity if the typical ratio of $a/r_{abs} = 10$ is being used.

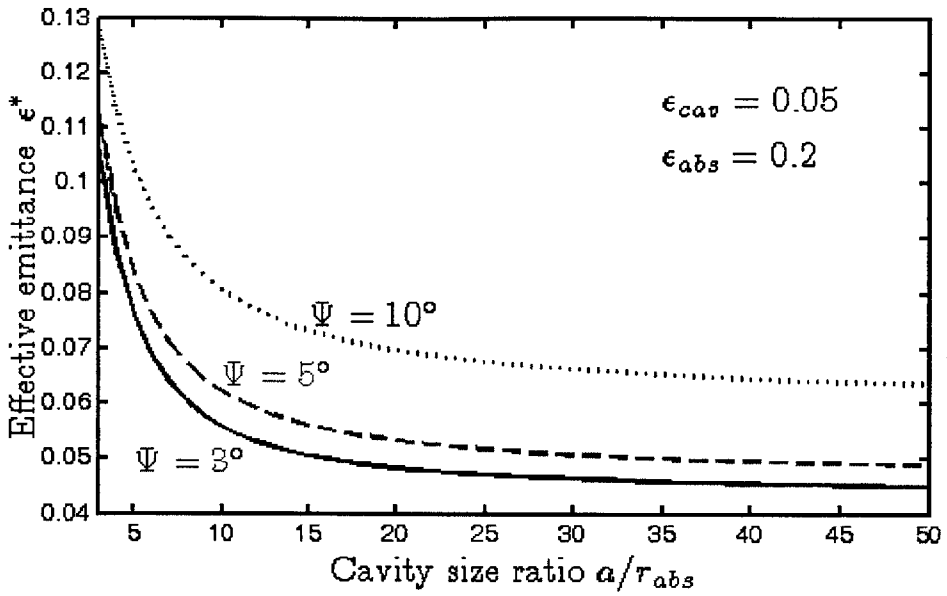

Figure 4.6 Analytical effective emittance results for varying cavity size ratio for 3-D ellipsoidal cavity. Different curves denote different opening angles

The results from the analytical treatment of elliptical and ellipsoidal cavities show that they perform well, significantly reducing the radiative losses from an absorber in a solar-thermal system. If these results can be matched in practice, there is no doubt that the cavity will lead to significantly improved performance for a STEG or other solar-thermal system.

4.2 Elliptical geometries with specular absorber reflection

The reflective behavior of the ellipsoidal cavity allows us to find an analytical solution for effective emittance when a blackbody absorber is used. This is possible because all radiation directed towards the mirror walls return to the absorber and are reabsorbed. When the absorber is not a blackbody the reflected radiation might reflect from the absorber rather than be reabsorbed, and if this reflection is specular it is not obvious where the radiation will be subsequently

directed (into the cavity walls again or out the aperture). Previously we used the diffuse radiation case to estimate the performance, but with ray tracing we can find the specular case performance and compare it to the diffuse case.

4.2.1 2-D elliptical geometries

The difference in the two cases is most notable for large apertures. Figure 4.7 shows effective emittance as a function of opening angle for a 2-D elliptical cavity for various absorber emittances. Figure 4.7 shows the ray tracing specular results for the equivalent cavity with a diffuse absorber as is plotted in Fig. 4.1 (solid curves for specular results, dashed curves for diffuse results). We see that the blackbody cases are exactly the same, which we expect because in the blackbody case there are no issues of multiple internal reflections. For the $\epsilon_{abs} = 0.5$ and $\epsilon_{abs} = 0.2$ cases, the specular performance is better, especially for large opening angles. This indicates that radiation specularly reflecting from the cavity walls is more likely to continue hitting the walls and absorber, whereas diffuse reflections from the absorber are more likely to leave through the aperture. At the standard opening angle of 5°, the diffuse analytical case overestimates effective emittance by about 0.03 and 0.02 in the $\epsilon_{abs} = 0.5$ and $\epsilon_{abs} = 0.2$ cases respectively. This is not a huge error, but it is significant enough that if the majority of reflection from the absorber is specular, ray tracing simulations should be pursued rather than the analytical solution.

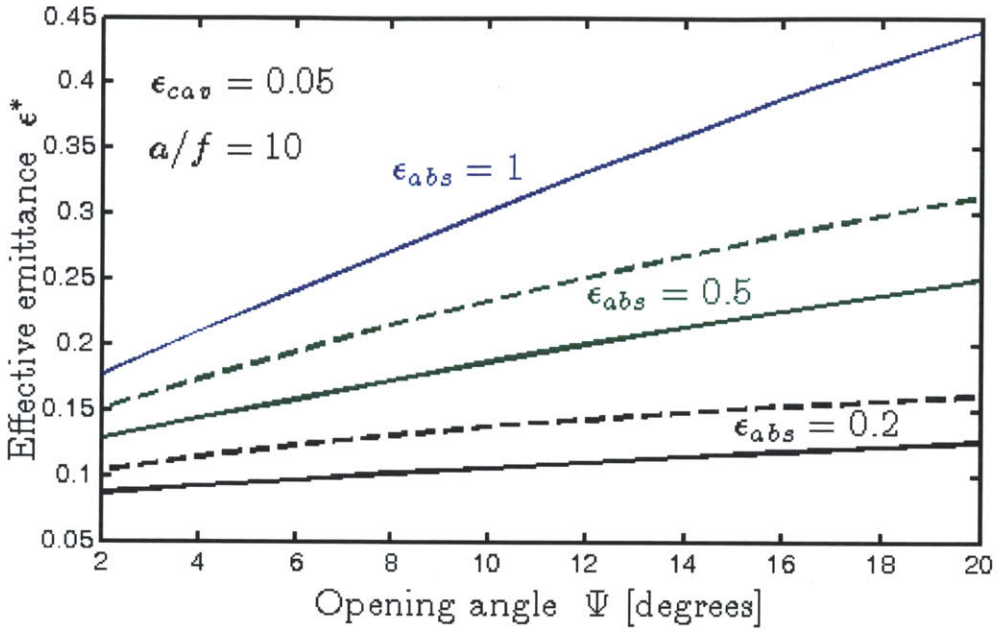

Figure 4.7 Ray tracing effective emittance results for varying opening angle for 2-D elliptical cavity with specularly reflecting absorber (solid curves), and diffuse absorber results for comparison (dashed curves)

Figure 4.8 shows effective emittance versus mirror emittance for the 2-D elliptical cavity case from specular ray tracing simulation (solid curves), with diffuse results for comparison (dashed curves). Comparing to the results for the diffuse solution, we see that the results are very similar for large mirror emittance values, and show a larger difference when the mirrors are highly reflective. This makes intuitive sense, as the more radiation the mirrored walls absorb, the less significant the reflecting behavior of the absorber becomes. For small mirror emittance values, the specular results show a significant improvement, around 15% lower effective emittance when $\epsilon_{cav} = 0.05$.

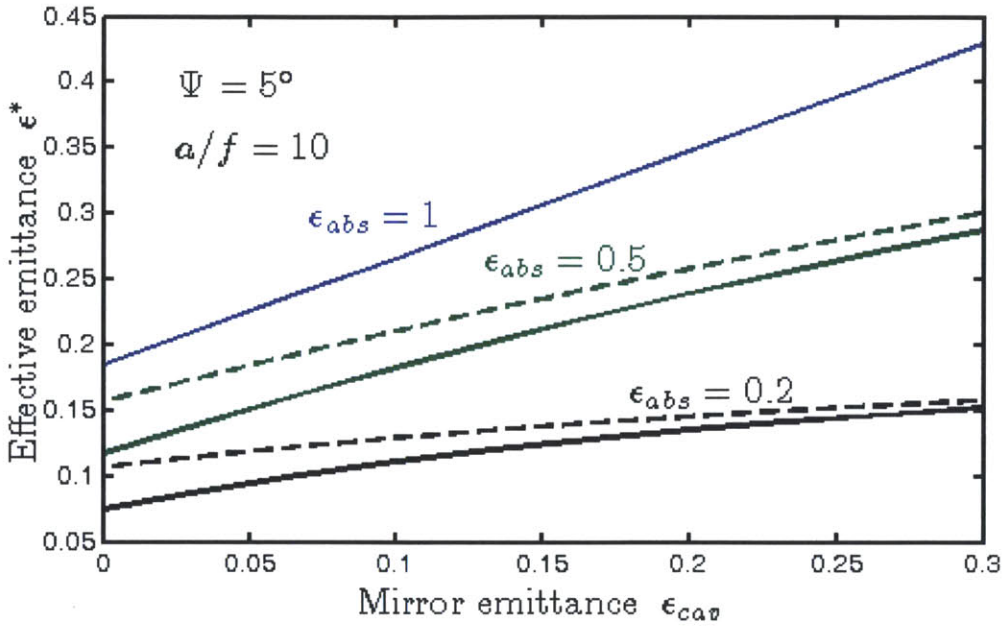

Figure 4.8 Ray tracing effective emittance results for varying mirror emittance for 2-D elliptical cavity with specularly reflecting absorber (solid curves), and diffuse results for comparison (dashed curves)

Figure 4.9 shows effective emittance versus cavity size for the 2-D elliptical cavity case from specular ray tracing simulation (solid curves) along with diffuse results for comparison (dashed curves). Comparing to the diffuse case, we can see that performance is similar for small cavities, but the specular case performs significantly better for large cavities. This is a bit counter intuitive given the pattern noted earlier where larger apertures made the specular case perform better, as now larger cavities (which have smaller view factors to the aperture) also lead to better specular performance. Here the result can be viewed as a consequence of large cavities becoming closer to hemispherical, and in a hemispherical cavity with specular reflection from the absorber, radiation not initially directed toward the aperture is unlikely to be later reflected towards it. This is because radiation undergoing multiple reflections inside a hemispherical cavity will tend to

have very similar azimuthal launch angles from the absorber or cavity floor even after many internal reflections. It is thus important to consider the specular ray tracing results rather than the diffuse solution for large cavities.

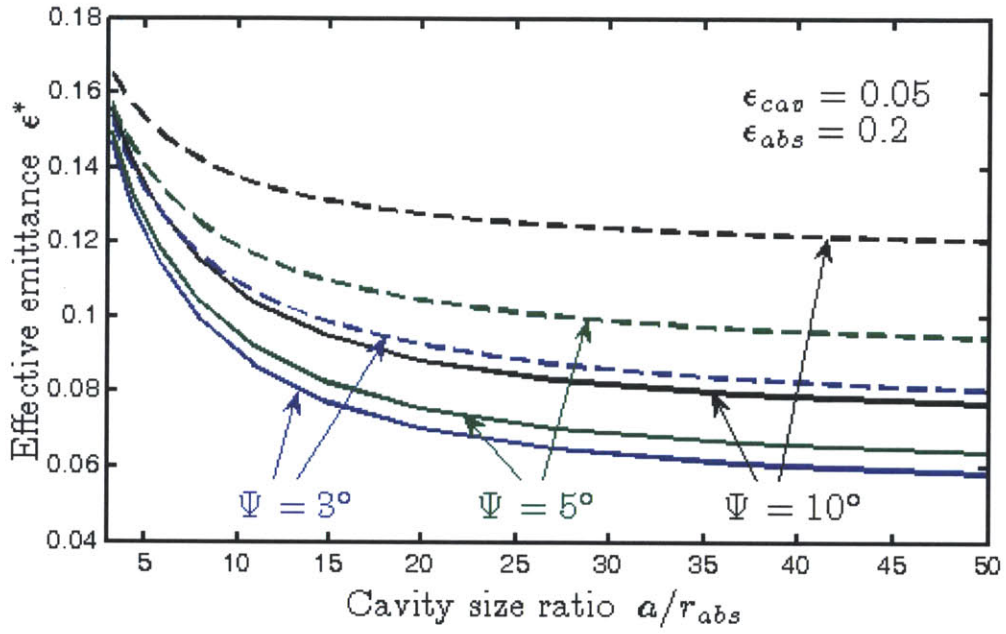

Figure 4.9 Ray tracing effective emittance results for varying cavity size ratio for 2-D elliptical cavity with specularly reflecting absorber (solid curves), with diffuse results for comparison (dashed curves)

4.2.2 3-D ellipsoidal geometries

Figure 4.10 shows effective emittance versus opening angle for a specular absorber, this time for the 3-D ellipsoidal cavity case (solid curves), along with results from the diffuse case for comparison (dashed curves). Comparing to the diffuse absorber case, the results are very similar for small opening angles. As before however, for opening angles larger than about 5°, the results rapidly diverge, with the effective emittances calculated in the diffuse case being significantly larger. Even for small opening angles, the diffuse case predicts about 20% higher effective

emittance, so again a ray tracing simulation should be used over the analytical solution if specular reflection is expected.

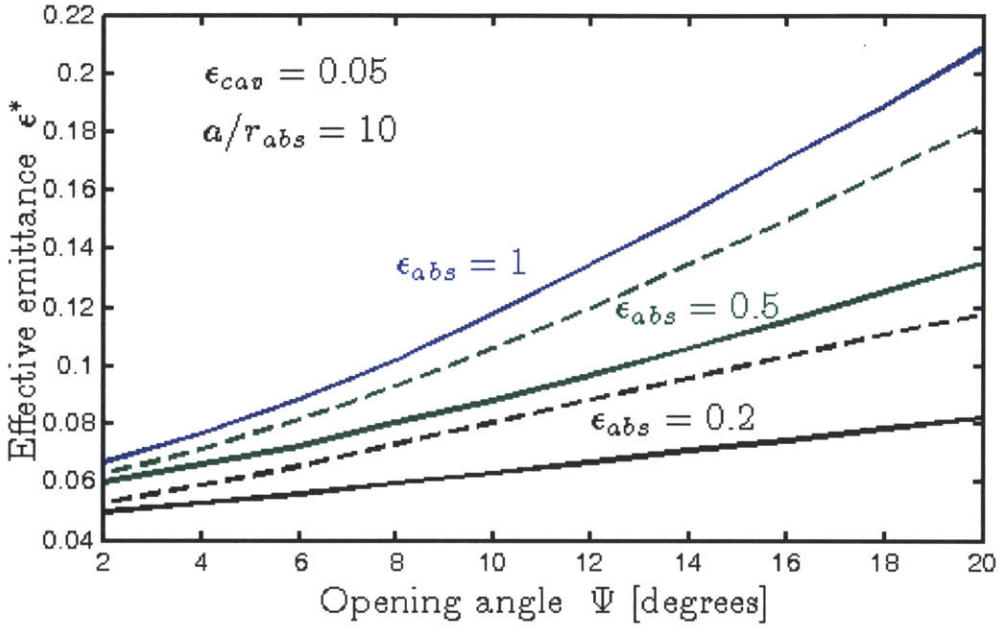

Figure 4.10 Ray tracing effective emittance results for varying opening angle for 3-D ellipsoidal cavity with specularly reflecting absorber (solid curves), with diffuse results for comparison (dashed curves)

Figure 4.11 shows effective emittance versus mirror emittance for a 3-D ellipsoidal cavity from specular ray tracing results (solid curves), as well as results from the diffuse case for comparison (dashed curves). The two cases are very similar, with results being almost identical for large mirror emittance values. At low mirror emittance values, the specular case shows more differentiation between absorber emittance values, due to the larger number of reflections off the absorber which afford more chances for re-absorption in the specular case.

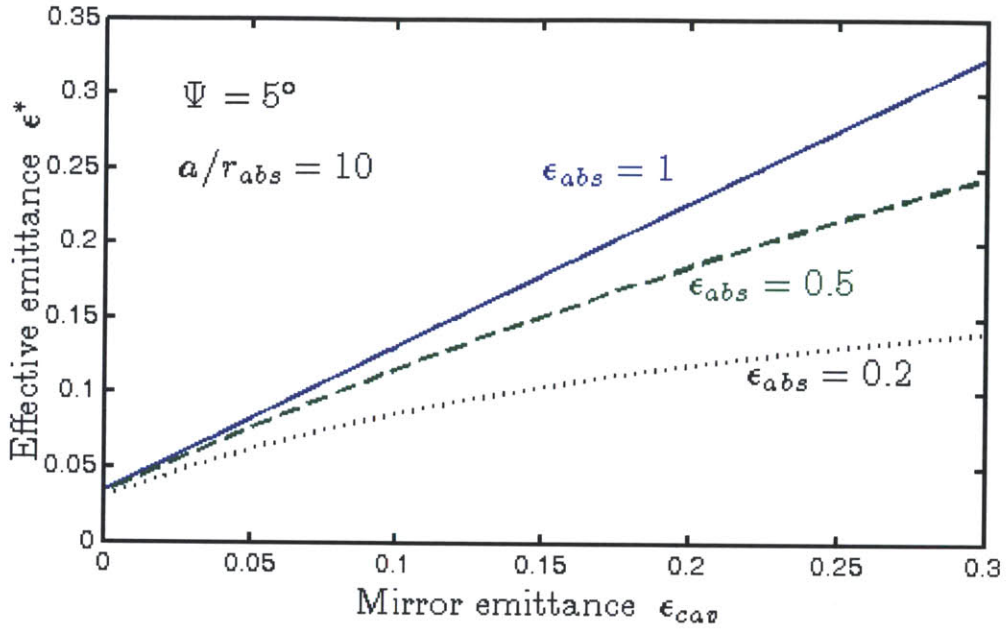

Figure 4.11 Ray tracing effective emittance results for varying mirror emittance for 3-D ellipsoidal cavity with specularly reflecting absorber (solid curves), with diffuse results for comparison (dashed curves)

Figure 4.12 shows effective emittance versus cavity size ratio for a 3-D ellipsoidal cavity from specular ray tracing results (solid curves), along with the diffuse case results for comparison (dashed curves). In the 3-D case, there is not as large a difference in results between the diffuse and specular cases as there was in the 2-D case (see Fig. 4.9). The exception is the case with the large opening angle of 10°, for which the specular case still performs significantly better (the reason for this having been discussed above).

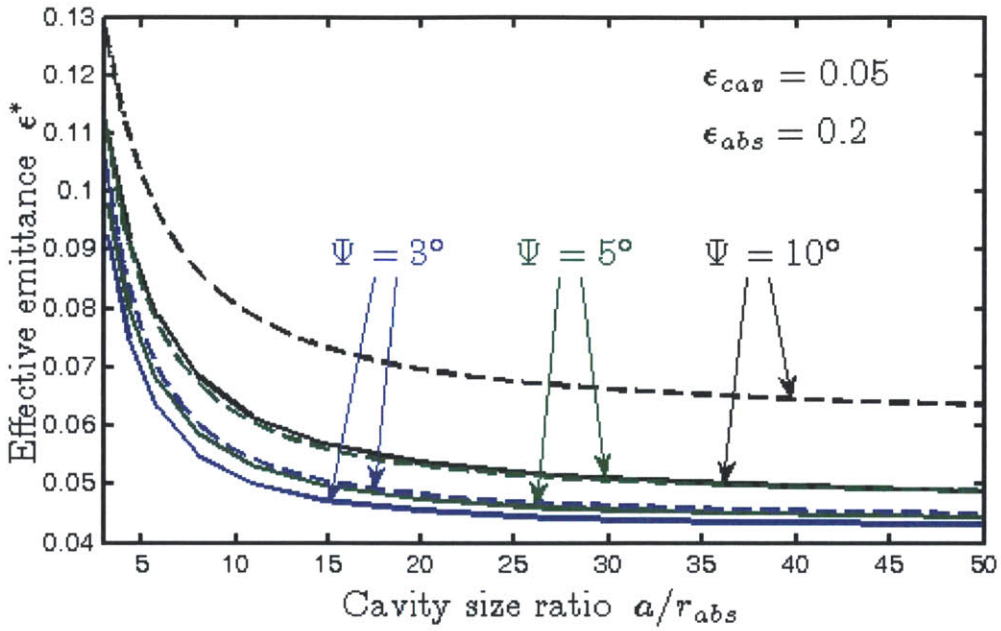

Figure 4.12 Ray tracing effective emittance results for varying cavity size ratio for 3-D ellipsoidal cavity with specularly reflecting absorber (solid curves), with diffuse results for comparison (dashed curves)

4.3 Performance of circular and hemispherical cavities

The main point of interest in investigating circular or hemispherical cavities compared to elliptical cavities is the lack of ideal reflecting behavior. For a properly aligned elliptical cavity, any ray emitted from the absorber will return in a single reflection. This is not the case for circular or hemispherical cavities. For these cavities, as the cavity becomes larger relative to the absorber, performance becomes closer to ideal. This can be viewed from two equivalent perspectives: as the cavity grows larger, the absorber appears more like an infinitesimal dot at its center, which the cavity is able to specularly reflect back to perfectly. Alternatively, we know an ellipse yields perfect performance, and an ellipse with two foci at the same location is a circle. As the cavity grows larger relative to the absorber, it approaches the elliptical case. Table 4.3

below shows the values used for ray tracing simulations involving circular and hemispherical cavities unless otherwise noted.

Table 4.3 Parameters used for ray tracing simulations

Parameter	Symbol	Value
Cavity wall emittance	ϵ_{cav}	0.05
Absorber emittance	ϵ_{abs}	0.2
Opening angle	Ψ	5°
Cavity size ratio	r_{cav}/w_{abs} or r_{cav}/r_{abs}	10
Rays used in simulation	N_{tot}	10^6

4.3.1 2-D circular geometries

Figure 4.13 shows results from the ray tracing simulation for a 2-D circular cavity, along with results from the 2-D elliptical cavity for comparison. It also separates contributions to effective emittance between rays absorbed by the mirrored cavity walls and rays lost through the aperture. The circular cavity performs similarly to the 2-D elliptical cavity, with effective emittance values +/- 0.01 of the equivalent case (see the $\Psi = 5°$ case in Fig. 4.9). Thus for the circular cavity, emittance is also significantly reduced, with effective emittances below 0.08 achievable for large cavities ($r_{cav}/w_{abs} > 30$). It is interesting to note that at small cavity ratios, the circular cavity actually performs better than the elliptical cavity. This is because for these small cavities, the elliptical geometry allows more multiple reflecting rays out through the aperture. Also interesting to note is the trend of the specific contributions. Larger cavities always reduce aperture losses, but for small cavities increasing cavity size seems to make mirror losses worse. This is because for these small cavities, the aperture size is considerable enough that stray rays are more likely to leave through the aperture than have many mirror reflections.

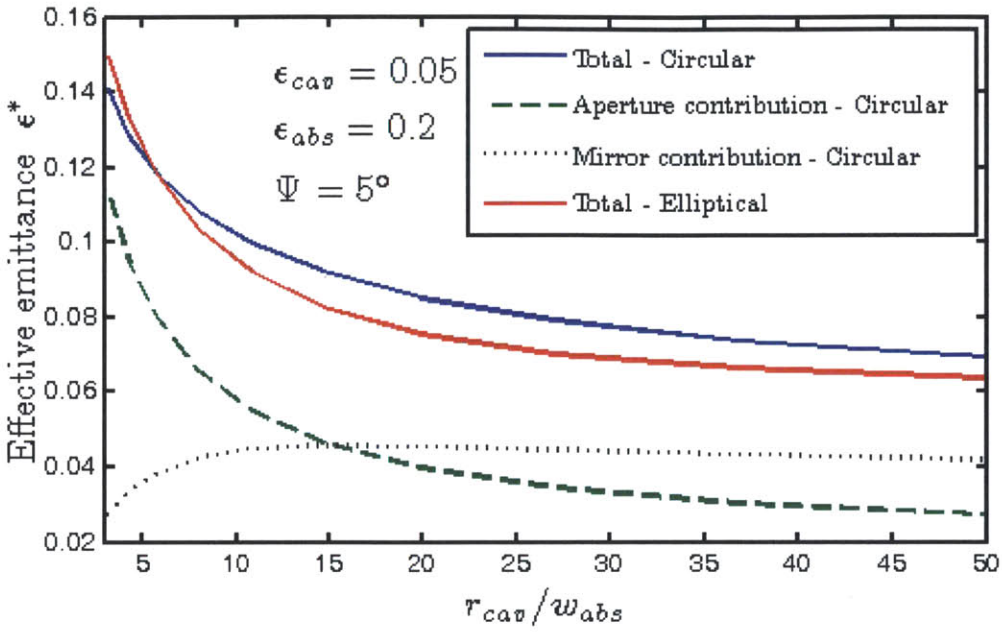

Figure 4.13 Effective emittance for 2-D circular cavity with varying cavity size ratio: solid blue curve denotes total emittance, dashed green curve denotes aperture contribution and dotted black curve denotes mirror contribution. Solid red curve shows total emittance of the 2-D elliptical cavity for comparison

4.3.2 3-D spherical geometries

Figure 4.14 shows effective emittance for a hemispherical cavity as a function of the cavity size ratio r_{cav}/r_{abs} given by ray tracing simulations, along with results from the 3-D ellipsoidal cavity for comparison. Here the hemispherical cavity performs worse than the ellipsoidal cavity, with the hemispherical cavity effective emittances being around 0.01 to 0.02 greater than the equivalent ellipsoidal case. It is also interesting to note the difference in relative contribution to effective emittance for this case compared to the 2-D case. Since the 3-D case has a smaller view factor between the absorber and aperture, mirror reflectance becomes much more important, and is the dominant cause of radiative losses for the hemispherical cavity. As shown,

the hemispherical cavity can achieve effective emittance below 0.08 for moderate cavity sizes ($r_{cav}/r_{abs} > 10$).

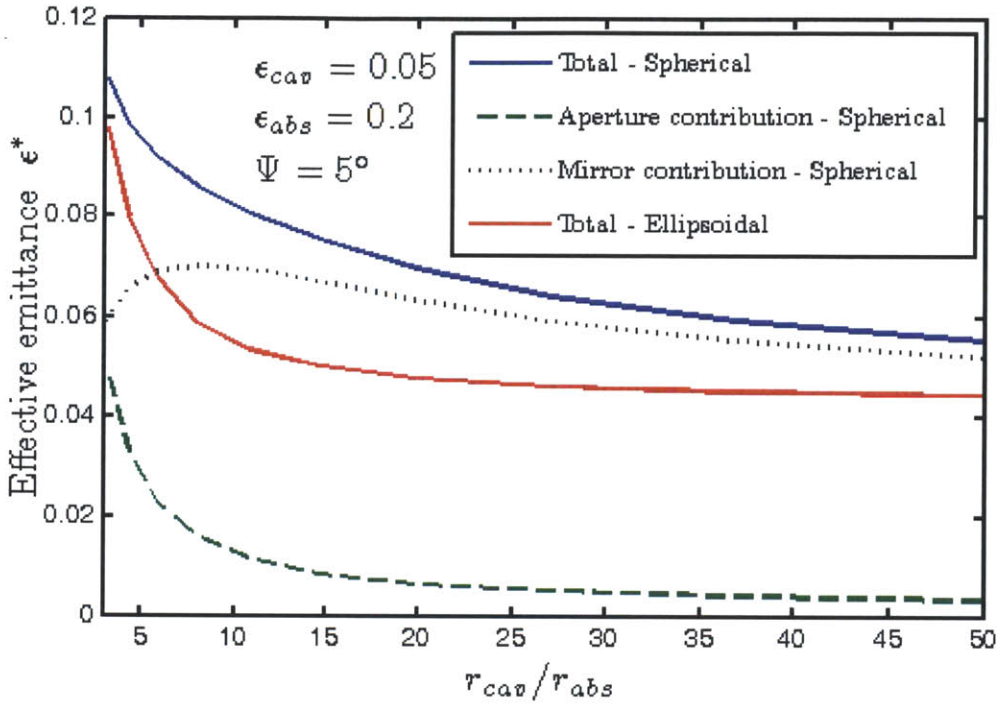

Figure 4.14 Effective emittance for 3-D hemispherical cavity with varying cavity size ratio: solid blue curve denotes total emittance, dashed green curve denotes aperture contribution and dotted black curve denotes mirror contribution. Solid red curve denotes total emittance of the 3-D ellipsoidal cavity for comparison

While the non-ideal geometries do not perform as well as the elliptical geometries, ray tracing simulations show that they are still successful at significantly reducing effective emittance of a solar absorber. Their ease of manufacture and potential for stock parts thus make the circular and hemispherical geometries worth pursuing despite their performance being worse in some cases.

4.4 Misalignment of absorber in x-y plane

A potential problem in manufacturing this proposed optical cavity lies in precisely aligning the absorber within the cavity. This is especially true considering that if the absorber is to be thermally isolated from the cavity (which it needs to be in practice) the absorber cannot be in direct contact with the cavity floor. Precise alignment is also complicated by the fact that the cavity has better performance when the absorber is much smaller than the cavity, and it is more difficult to properly align an absorber in a large cavity than a small one. First we will consider systems where the absorber is off center in the x-y plane. That is, in the 2-D case the absorber will be left or right of center by a distance x_{mis}, and in the 3-D case the center of the absorber will be some radial distance r_{mis} from the center axis of the cavity (see Fig. 4.15).

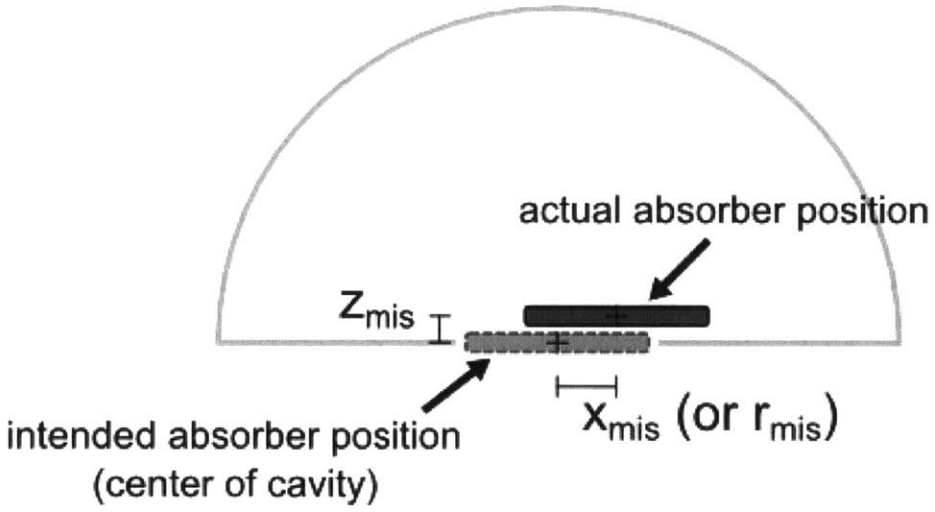

Figure 4.15 Diagram of how absorber misalignment is defined: lighter absorber marks intended position while darker absorber marks actual position. Note that the sign of x_{mis} and r_{mis} is unimportant due to rotational symmetry. Positive values of z_{mis} denote the absorber being above the center plane, while negative values denote the absorber being below the center plane

4.4.1 2-D cavity geometries

The first case we will investigate is misalignment of the absorber for a 2-D circular cavity. Figure 4.16 shows effective emittance as a function of absorber misalignment for various cavity size ratios. It should be noted that absorber misalignment distance is normalized to absorber size, so the ratio x_{mis}/w_{abs} is used rather than simply x_{mis}. For all the absorber cavity size ratios investigated, effective emittance increases by about 0.05 at a misalignment of one absorber half width. The larger cavities are thus more sensitive to misalignment for two reasons. While the absolute increase in effective emittance is similar for all cases, this represents a much more significant relative increase for the large cavity cases. Additionally, the misalignments are normalized to absorber size, so the same misalignment ratio for the larger cavity size ratios represents a smaller absolute misalignment. Lastly it can be noted for the circular case that the increase in effective emittance with misalignment reaches a linear relationship, but starts a bit flatter. This means that for small misalignments, the degradation of performance is more forgiving.

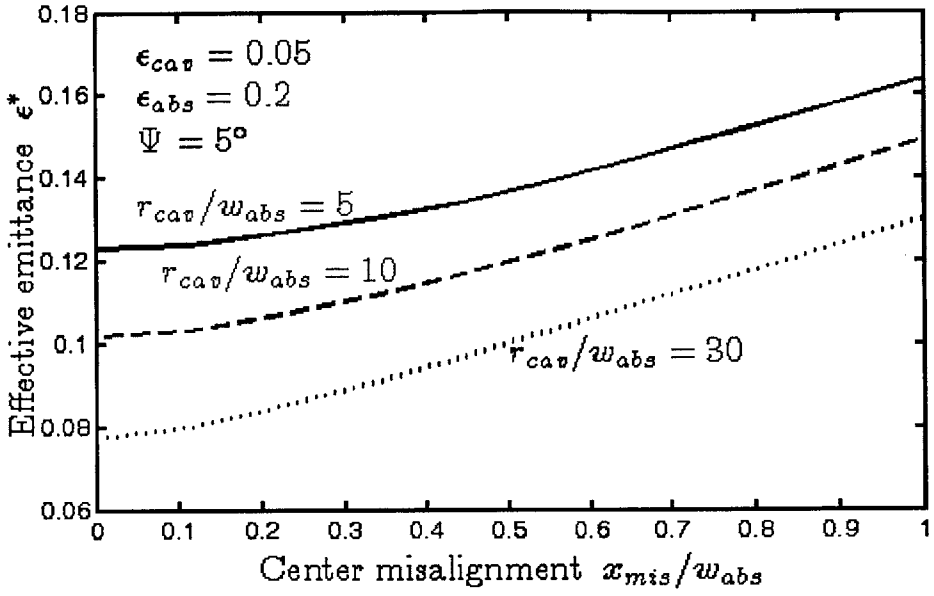

Figure 4.16 Effective emittance for varying center misalignment for 2-D circular cavity

Figure 4.17 shows the effect of absorber misalignment for 2-D elliptical cavities. It is almost identical to the circular case, with increases in effective emittance of about 0.05 compared to the aligned case for misalignment ratios of $x_{mis}/f = 1$. The only notable difference from the circular case is that the relationship between effective emittance and misalignment is now approximately linear for the entire range of misalignments investigated. This means that for an elliptical cavity, performance degradation is not as forgiving for small misalignments.

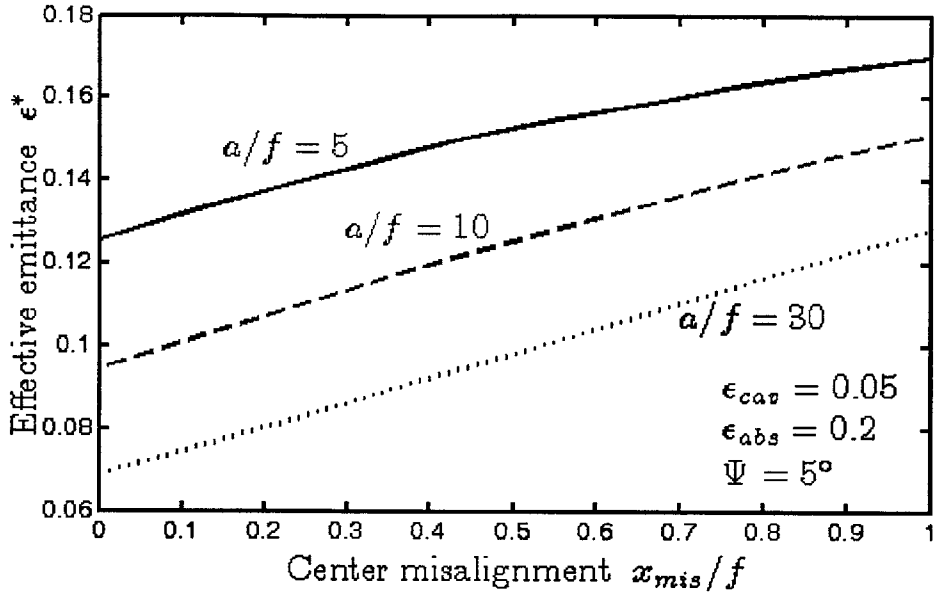

Figure 4.17 Effective emittance for varying center misalignment for 2-D elliptical cavity

4.4.2 3-D cavity geometries

Trends for misalignment in the 3-D cases are more pronounced. Figure 4.18 shows effective emittance as a function of absorber misalignment with various cavity size ratios for a 3-D hemispherical cavity. For this case, the sensitivity of larger cavities is even more apparent. For the small cavity with $r_{cav}/r_{abs} = 5$, effective emittance increases by about 50% from 0.095 to 0.135 when the absorber is misaligned by one radius. For the larger cavity with $r_{cav}/r_{abs} = 30$, effective emittance is almost doubled from around 0.06 to 0.12. Thus for large hemispherical cavities, absorber alignment is extremely important. Similar to the circular cavity, the increase is less drastic when absorber misalignment is maintained below $x_{mis}/r_{abs} = 0.2$, which makes it a good target for alignment tolerance in practice.

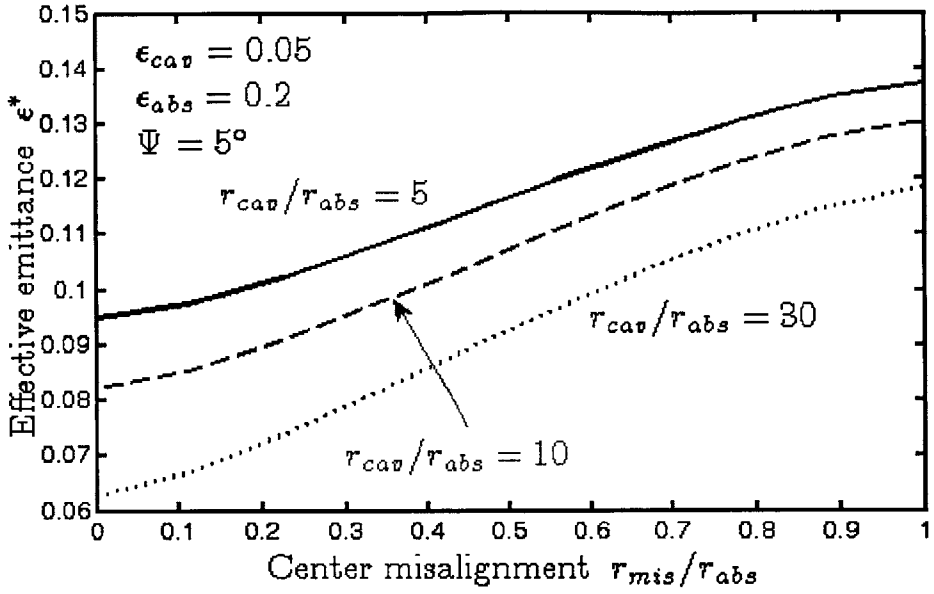

Figure 4.18 Effective emittance for varying center misalignment for 3-D hemispherical cavity

Figure 4.19 shows the effect of absorber misalignment on effective emittance for 3-D ellipsoidal cavities. The trend is similar to hemispherical cavities, although with an even larger relative increase. For the largest ellipsoidal cavity investigated ($a/r_{abs} = 30$), effective emittance almost doubles, increasing from below 0.05 to almost 0.12 when the absorber is misaligned by one absorber radius. Similar to the 2-D elliptical case, the trend is approximately linear even for small misalignments, so care should be taken for precise absorber alignment in the ellipsoidal cavity case.

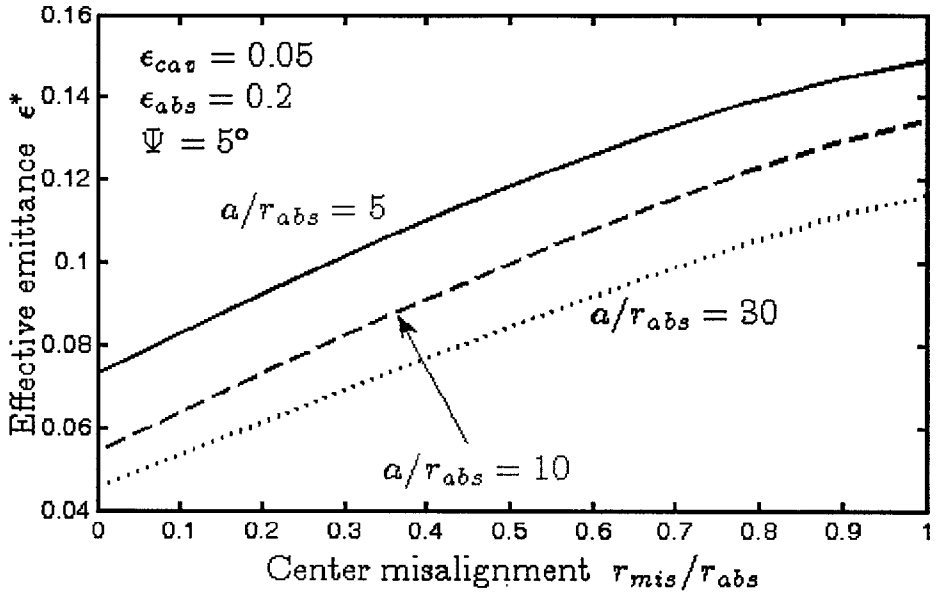

Figure 4.19 Effective emittance for varying center misalignment for 3-D ellipsoidal cavity

Absorber misalignment in the x-y plane always results in worse performance, so care should be taken to properly align the absorber and cavity axis. As shown, larger cavities are more sensitive to this misalignment, so their improved performance will be lost if care is not taken to properly align the system. Circular and hemispherical cavities are a bit more lenient however, and if the misalignment relative to the absorber radius can be kept below 0.2, then the increase in effective emittance will not be excessive.

4.5 Misalignment of absorber in z plane

Misalignment can occur in the z direction ("height") as well (the absorber and cavity floor might be higher or lower than the centered position). In these cases, we will see that performance is not necessarily at an optimum when the absorber and floor are located at the center plane of the cavity. Here the misalignment is characterized by a distance z_{mis} (see Fig.

4.15), and the influence on effective emittance is investigated versus the ratio of z_{mis} to absorber half width (2-D case) or radius (3-D case).

4.5.1 2-D cavity geometries

Figure 4.20 shows effective emittance versus height misalignment for different cavity size ratios in the 2-D circular cavity case. Performance is highly sensitive to height misalignment, when z_{mis}/w_{abs} is increased from 0 to 0.5, effective emittance increases above 0.16 for all three cases investigated. This performance shows a very small benefit over the absorber emittance of 0.2. When the height is lowered rather than raised, the performance is degraded slightly less, with effective emittance increasing to around 0.15 when $z_{mis}/w_{abs} = -0.5$. Also worth noting is that for this case, the optimal performance actually occurs when z_{mis}/w_{abs} is slightly greater than zero. This is because for the circular case, raising the absorber and floor slightly makes the cavity closer to the hemispherical case, and some of the benefit of that geometry is gained. The circular cavities at optimal height "misalignment" actually perform comparably to the elliptical cases (see Fig. 4.21), so if precise alignment is possible the 2-D case circular cavities should be pursued over elliptical geometries.

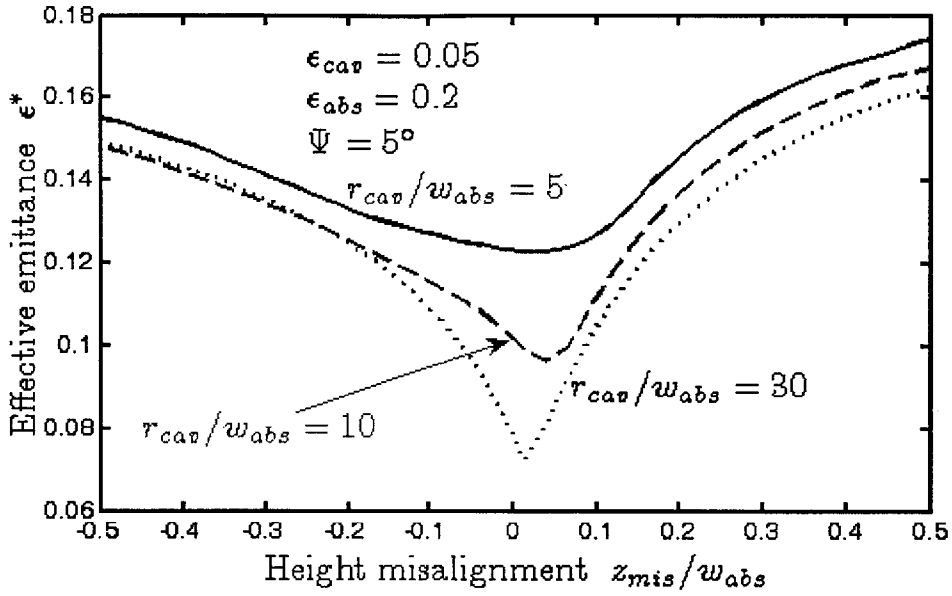

Figure 4.20 Effective emittance for varying height misalignment for 2-D circular cavity

Figure 4.21 shows effective emittance versus height misalignment for different cavity size ratios in the 2-D elliptical cavity case. The results here are very similar to the circular case, with the only notable difference being that optimal performance here occurs for an absorber with no height misalignment.

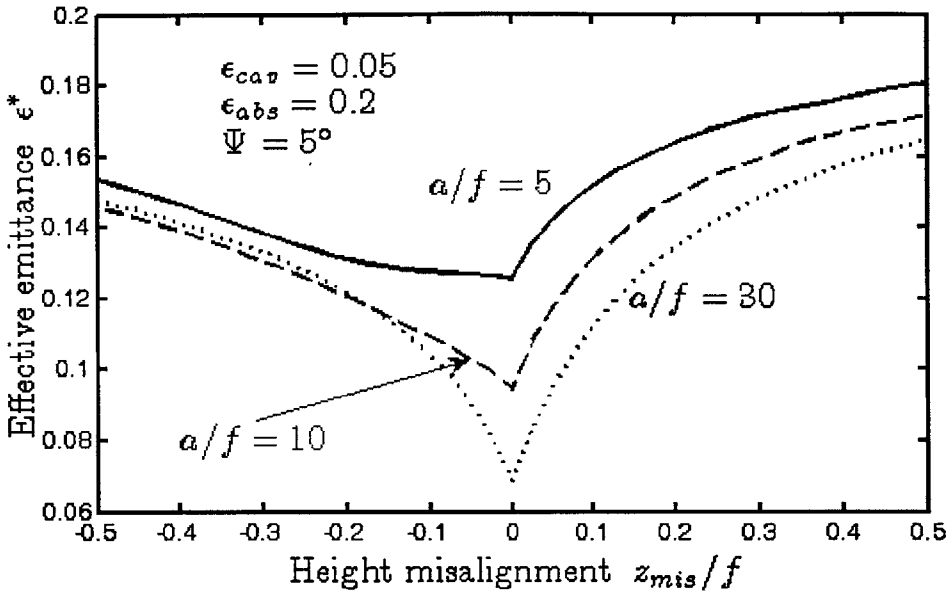

Figure 4.21 Effective emittance for varying height misalignment for 2-D elliptical cavity

4.5.2 3-D cavity geometries

Figure 4.22 shows effective emittance as a function of height misalignment for various cavity size ratios in the 3-D hemispherical cavity case. Performance is very sensitive to alignment for all the sizes considered, with a very narrow range of acceptable misalignment ratios before the cavity is no longer effective. Similar to the 2-D circular case, the optimal performance actually occurs for z_{mis}/r_{abs} ratios slightly greater than zero.

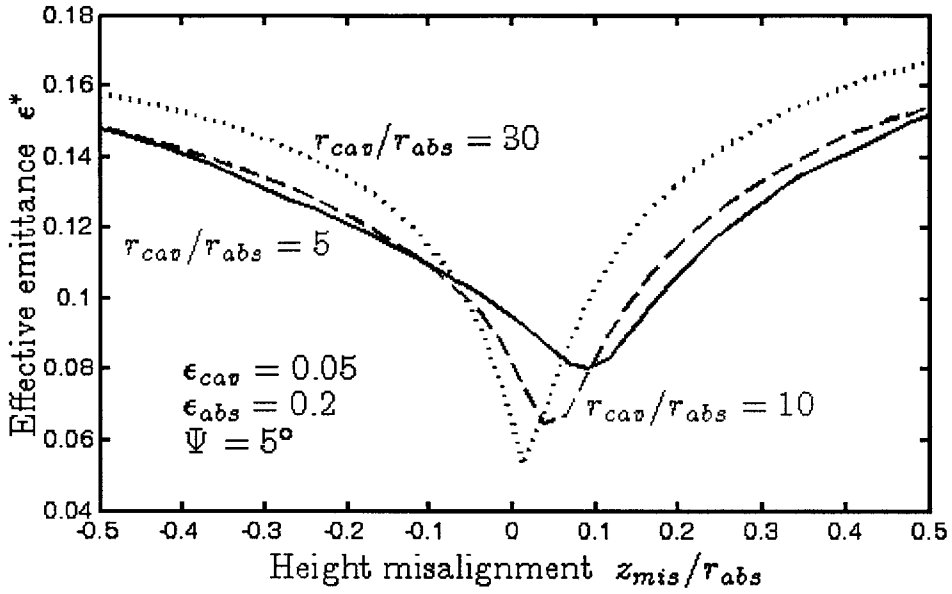

Figure 4.22 Effective emittance for varying height misalignment for 3-D hemispherical cavity

Figure 4.23 shows effective emittance as a function of height misalignment for various cavity size ratios in the 3-D ellipsoidal cavity case. Once again performance suffers sharply for even small deviations from the ellipse center plane. For this case the optimal performance occurs when the absorber and floor are located at the ellipsoid equator (i.e., $z_{mis} = 0$).

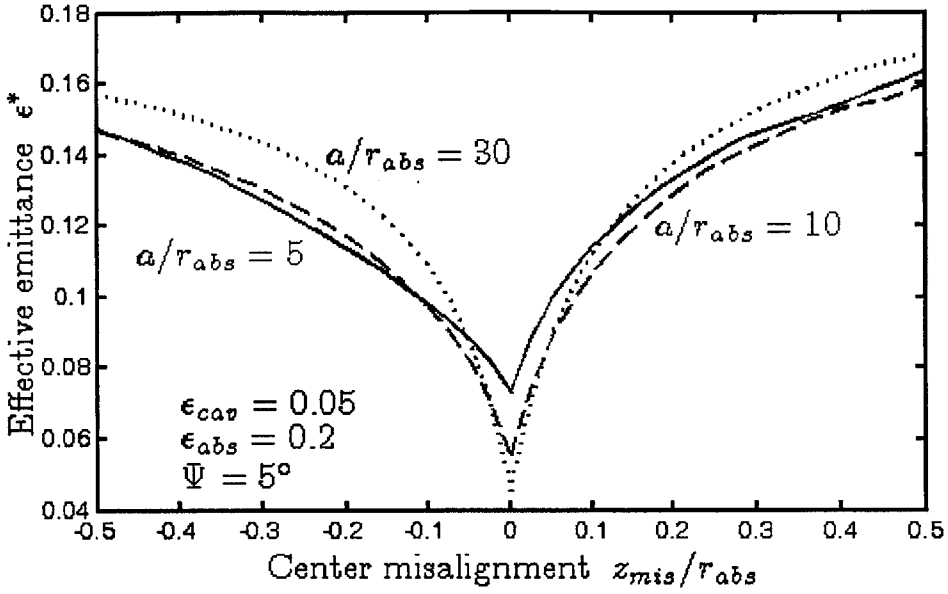

Figure 4.23 Effective emittance for varying height misalignment for 3-D ellipsoidal cavity

From the results in this section it is clear that proper alignment in the z direction is paramount to effective cavity operation. With misalignments as small as $z_{mis}/r_{abs} = 0.5$ the cavity can be rendered almost useless. Therefore particular care should be taken to properly align the absorber and floor of the cavity relative to the rest of the cavity when building such an optical cavity in practice.

4.6 Distortion of geometry

Results show that cavity performance for all geometries improves as the cavity size ratio increases (see section 4.3). From a manufacturing perspective this is problematic, as the processes used to manufacture larger structures (e.g., blow molding) can result in imperfect geometries and non-uniform thinning of structure walls [69]. In particular, hemispherical geometries may be distorted into ellipsoidal geometries. The effect of this distortion will be

investigated briefly here for hemispheres. 2-D geometries will not be considered as they are simpler to fabricate, and 3-D ellipsoids will not be considered as their precise manufacture would likely require a more complicated manufacturing process than those used for hemispheres to begin with.

Figure 4.24 shows the effective emittance as a function of cavity size for slightly distorted hemispheres along with a perfect hemisphere for comparison. For these cavities, a 1% oblate ellipsoid means that the ceiling (or rather where the ceiling would be in the absence of the aperture) of the hemisphere is 1% shorter than the equatorial radius, and a 1% prolate ellipsoid means the ceiling of the hemisphere is 1% longer than the equatorial radius. It is important to observe that for distorted geometries, performance deteriorates for larger cavity sizes. For the prolate ellipsoid, performance is poor and even for the moderate size ratio of $r_{cav}/r_{abs} = 25$ effective emittance is at a value close to the emittance of the absorber. The oblate ellipsoid outperforms the perfect hemisphere at small cavity size ratios before rapidly deteriorating. The cavity size which results in the best performance for oblate ellipsoids is the size ratio which satisfies the absorber condition given in Eq. (3.8) that is if the distortion happens to align with the condition which is aimed for in the design of ellipsoidal cavities.

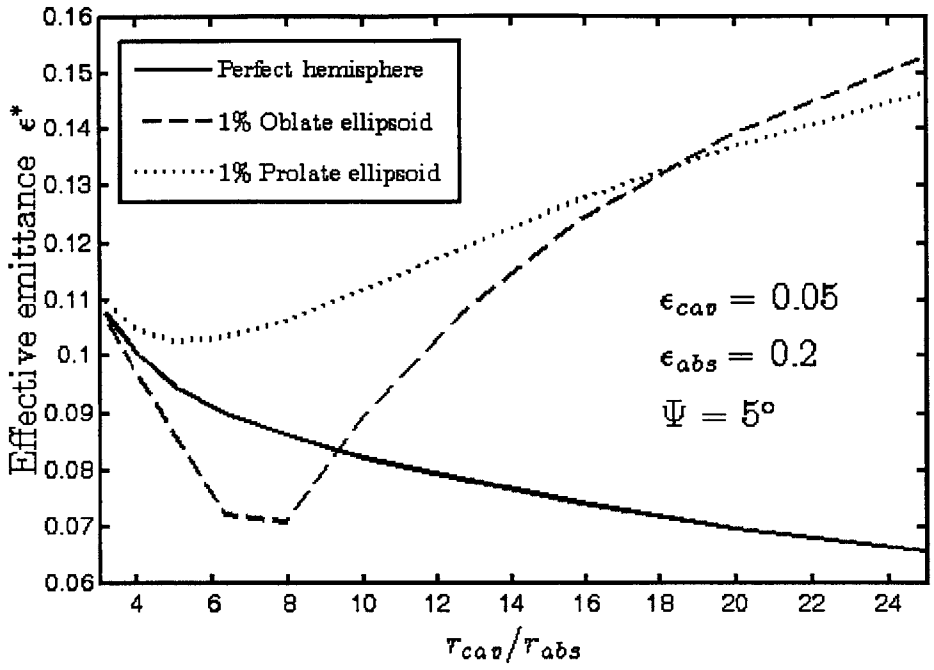

Figure 4.24 Effective emittance versus cavity size ratio for slightly distorted hemispheres. The dashed green curve denotes a 1% oblate distortion and the dotted black curve denotes a 1% prolate distortion. The solid blue curve denotes performance of a perfect hemisphere for comparison

These results show that in the case of distortion which would lead to prolate ellipsoids (even if the distortion is only 1%) performance of the cavity is poor, and such distortions should be avoided. Oblate distortions lead to good performance if the absorber size is chosen such that the ideal geometry pursued in the design of ellipsoidal cavities is obtained, otherwise oblate distortions also lead to poor performance. These results stress the important of the cavity geometry, and limit the size of potential cavities based on tolerances achievable for manufactured hemispheres.

4.7 Integration into a solar-thermal system

While the goal of the optical cavity is to reduce the effective emittance of the absorber, the reason we are interested in reducing effective emittance is to improve overall performance of some solar-thermal system (e.g., a STEG). It is therefore necessary to consider how the optical cavity interacts with other parts of the system, not only considering how absorber effective emittance is affected. In the case of an absorber in the optical cavity, the opto-thermal efficiency is given by

$$\eta_{ot} = \alpha\tau - \frac{\epsilon^*\sigma(T_H^4 - T_C^4)}{CG} \tag{4.1}$$

with the only difference from Eq. (1.9) being the replacement of emittance ϵ with effective emittance ϵ^*.

Reducing the size of the aperture will always improve (decrease) the effective emittance of the absorber, since less radiation will be able to escape through the aperture rather than be reflected back. At first glance, one might think this means that a smaller aperture will always result in better performance. This is not the case due to the fact that a smaller aperture will allow less sunlight to reach the absorber, setting an upper limit on the solar concentration ratio C. When considering opto-thermal efficiency, it is then the ratio ϵ^*/C which one would like to minimize, rather than simply minimizing ϵ^*. For an effective cavity, ϵ^* should be kept small while being able to maintain a large C.

If opto-thermal efficiency is the only concern and a treatment to minimize ϵ^*/C is taken, one will find that the optimized case completely sacrifices the cavity in favor of higher concentration. However part of the advantage of the cavity is avoiding expensive concentrating

optics and tight tracking limits, so more than opto-thermal efficiency alone needs to be considered for system design. For an effective system which makes good use of the optical cavity, neither ϵ^*/C or ϵ^* should be minimized blindly, both need to be considered.

4.7.1 Optical concentration

Optical concentration is a strategy which is commonly employed to improve the performance of solar thermal systems [70]. When sunlight is concentrated, efficiency can be improved as sunlight incident on a large area (the input of the concentrating optics) can be absorbed by a small area (the solar absorber). Since losses are associated with the smaller absorber area, optical concentration reduces losses thereby improving efficiency. Traditionally, solar concentration was performed by using lenses or reflecting mirrors to form a smaller image of the sun on the solar collector. More recently, the field of nonimaging optics is pursued for concentration applications, which relaxes the requirement that an image of the sun be formed. In general, nonimaging optics produces better performance, as relaxing the image forming requirement allows for higher concentration ratios and looser tracking requirements, and image forming is irrelevant to solar thermal applications [71]. Concentrating optics will not be explored with great depth in this thesis, but the interested reader is encouraged to explore further on their own [7].

There are a number of different optical concentration strategies that can be pursued in conjunction with the proposed optical cavity system. One method is using a lens with its focal plane at the absorber, with a relatively large aperture to allow the focused light through [72] (see Fig. 4.25a). Note that while lenses might be more commonly associated with imaging optics, nonimaging Fresnel lenses are commonly used in solar applications, so the advantage of nonimaging optics can still be realized here [73]. Another method is to use a compound parabolic

concentrator, which is a pair of curved mirrors, focused at a small aperture, with the light spilling onto a larger absorber [54] (see Fig. 4.25b). The compound parabolic concentrator is the quintessential nonimaging optics concentrator, which reflects all incident light within the acceptance angle to the focus in 2-D, and achieves close to ideal performance in 3-D. In this thesis, only methods where the focal plane of the concentration system is at the absorber are pursued (e.g., Fig. 4.25a). This is because in the balance of effective emittance ϵ^* and concentration ratio C, making the aperture smaller yields relatively small gains for effective emittance, while focusing at the absorber makes significant gains for concentration ratio. It is also counter-productive from a system wide perspective to focus sunlight and let it disperse again before being absorbed.

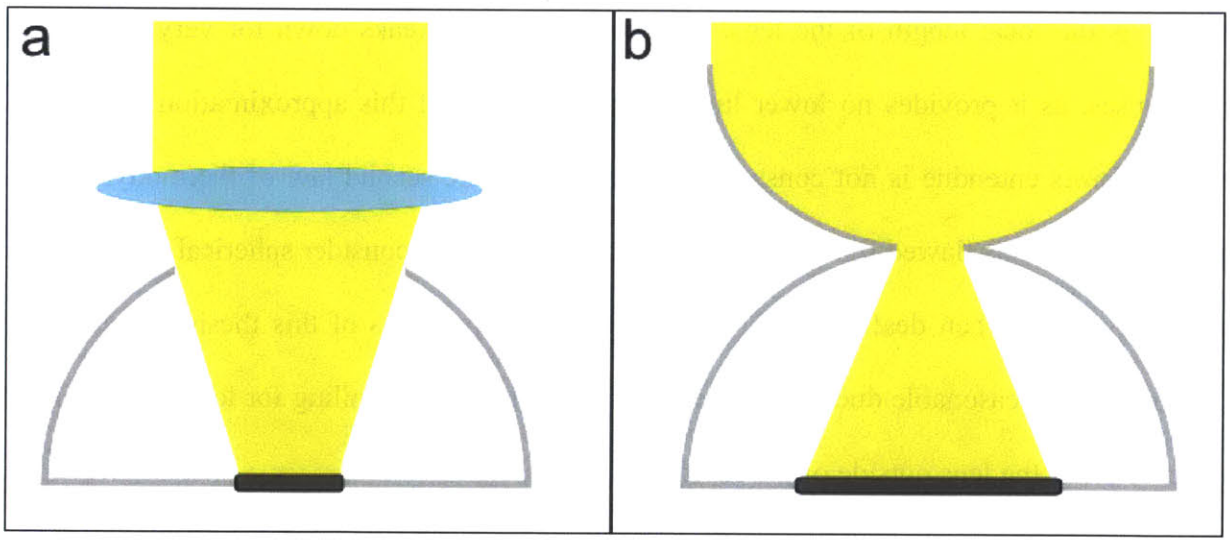

Figure 4.25 Examples of concentrating optics: a) focusing lens b) compound parabolic concentrator

Concentrating optical system design is a field in itself and will not be explored in depth in this thesis. That being said, it is important to know the achievable concentration ratios possible for a cavity with a given opening angle, as concentration ratio plays a large role in opto-thermal

efficiency of the system. A simple treatment for concentration that can be achieved with a single lens will be used to estimate the concentration ratios achievable for given cavity geometries.

The purpose of focusing lenses is to bring collimated light to a single point at the lenses focal plane (see Fig. 4.26a). If the incident light is not perfectly collimated, but rather has some divergence half angle θ_d, then the lens will focus the light to a finite spot rather than a point (see Fig. 4.26b). This is relevant to our situation as solar insolation is not collimated but has a divergence half angle of about 0.25°. In the simplest approximation, the radius of the spot r_{spot} will be [72]

$$r_{spot} = f_L \tan \theta_d \tag{4.2}$$

where f_L is the focal length of the lens. This approximation breaks down for very short focal length lenses, as it provides no lower limit to spot size, and if this approximation is used for small spot sizes entendue is not conserved (a violation of the second law of thermodynamics). The approximation is flawed for short focal lengths as it does not consider spherical aberration or other issues faced when dealing with real lenses. For the purposes of this thesis however, the approximation is reasonable due to relatively small opening angles calling for long focal lengths in order to place the lens outside of the cavity.

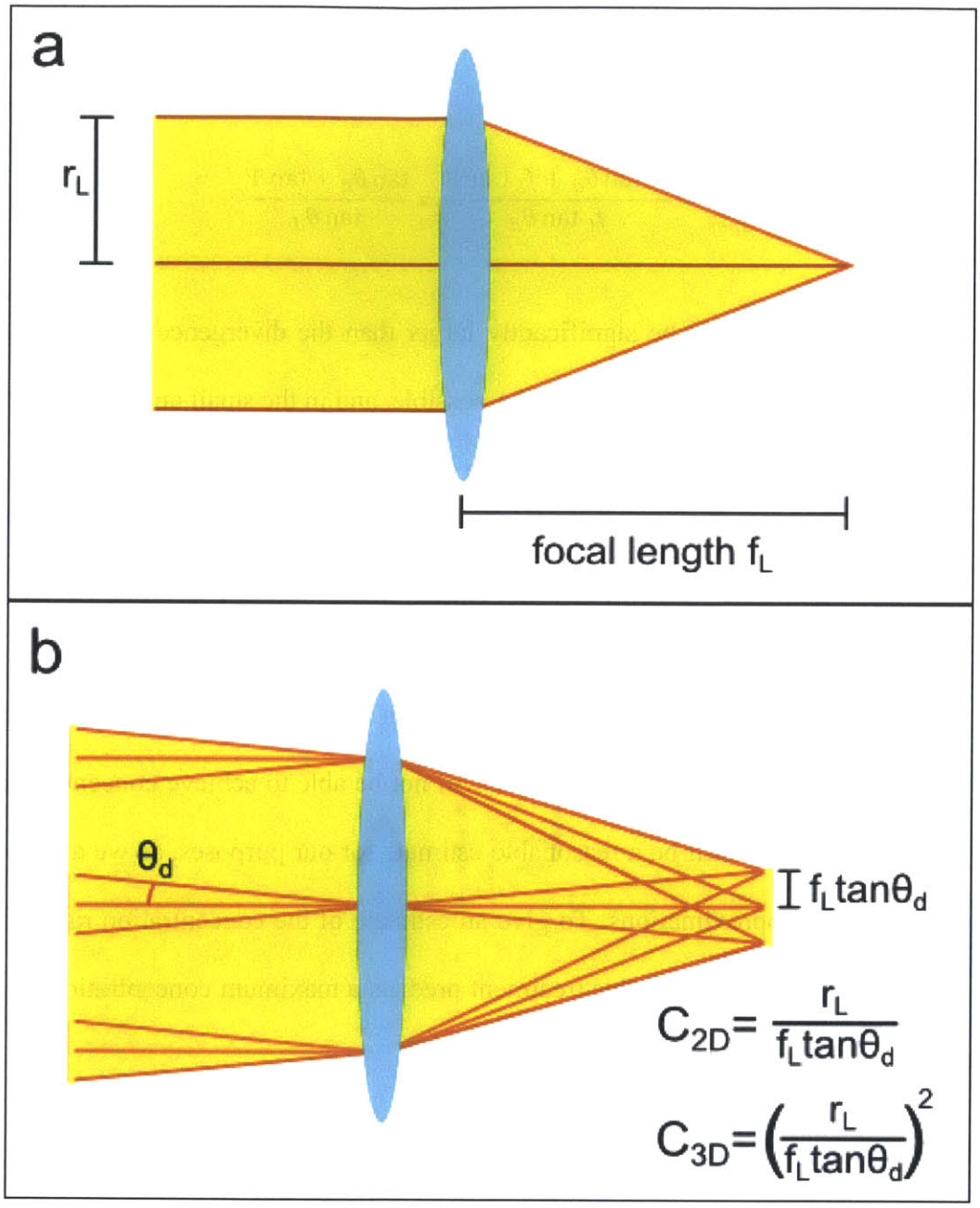

Figure 4.26 Principle of a focusing lens: a) lens focusing collimated light b) lens focusing light with some divergence. Expressions for concentration ratio *C* are given in the figure

The parameter of interest here is the concentration ratio of the lens in the optical system. With a lens of radius r_L, the concentration ratio C is given by r_L/r_{spot} in the 2-D case and

$(r_L/r_{spot})^2$ in the 3-D case. Examining the geometry of the system, the ratio of lens radius to spot radius is given by

$$\frac{r_L}{r_{spot}} = \frac{f_L \tan\theta_d + f_L \tan\Psi}{f_L \tan\theta_d} = \frac{\tan\theta_d + \tan\Psi}{\tan\theta_d} \tag{4.3}$$

Since the opening angle should be significantly larger than the divergence angle of incoming light in order for a large concentration ratio to be possible, and in the small angle limit (where we expect to be operating) tangent and sine of an angle are equal, this can be simplified to

$$\frac{r_L}{r_{spot}} = \frac{\sin\Psi}{\sin\theta_d} \tag{4.4}$$

which is the result for maximum possible concentration following a conservation of etendue argument [54]. This indicates that in practice we will not be able to achieve concentration ratios quite this high, but it should still be a reasonable estimate for our purposes, as we arrived at this result using reasonable approximations. To give an estimate of the concentration ratios possible using the standard 5° opening angle, this treatment predicts a maximum concentration of 20x for the 2-D case and 400x for the 3-D case.

4.7.2 Effect on opto-thermal efficiency

As increasing opto-thermal efficiency is the reason for using the cavity, it is worth investigating how the opto-thermal efficiency is influenced with and without the cavity. A brief investigation of opto-thermal efficiency for a system using the parameter values in Table 4.4 will be undertaken below. It is worth noting that transmittance has now been decreased to 0.9 from the earlier value of 0.95 used in this thesis in order to account for the losses associated with concentrating optics. Additionally, the cold side temperature has been increased to 50° C, as

operation at higher temperatures using concentration would make maintaining a low cold side temperature more difficult. Finally, the solar insolation value has been decreased to 800 W/m^2, as only direct solar insolation is usable in a concentrating system, and the previous value of 1000 W/m^2 included both direct and diffuse insolation.

Table 4.4 Parameters used for opto-thermal efficiency model

Parameter	Symbol	Value
Absorptance	α	0.95
Transmittance	τ	0.9
Cold side temperature	T_C	50° C
Solar insolation	G	800 W/m^2
Cavity opening angle	Ψ	5°

Figure 4.27 shows opto-thermal efficiency for a 2-D receiver system with and without the use of the optical cavity. Here the absorber emittance used is $\epsilon_{abs} = 0.2$, and an effective emittance with the cavity of $\epsilon^* = 0.1$ is assumed which is achievable as shown from results in previous sections. The concentration ratio used is $C = 15$, which is a more conservative value than the maximum possible ratio of 20 for a 5° opening angle cavity. The optical cavity significantly improves the opto-thermal efficiency of the system, and maintains a respectable η_{ot} of 0.7 up to 500° C. In the absence of the cavity, this efficiency can only be maintained up to around 375° C. This means that in addition to improving efficiency at the operating temperatures of existing systems, the use of the cavity opens up a new feasible regime of operating temperatures.

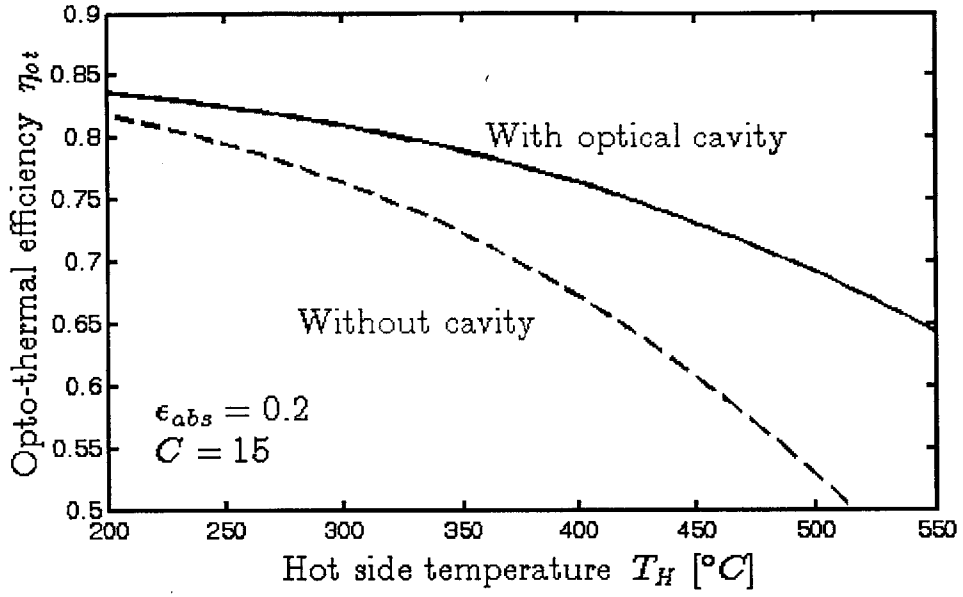

Figure 4.27 Opto-thermal efficiency as a function of hot side temperature with and without 2-D optical cavity

Figure 4.28 shows opto-thermal efficiency for a 3-D receiver system with and without the use of the optical cavity. Here the operating temperatures are much higher than for the 2-D case, due to the increased concentration ratios. Here the absorber emittance used is $\epsilon_{abs} = 0.5$, and the effective emittance with the cavity is assumed to be $\epsilon^* = 0.08$. The higher absorber emittance is used because for these high operating temperatures it would be much more difficult to achieve the previously used emittance of 0.2 while maintaining high absorptance, due to more spectral overlap and potential instability of the absorber surface. For the 3-D case, a conservative concentration ratio of 100x is used. The optical cavity is extremely effective at increasing opto-thermal efficiency and pushes the feasible operating temperature regime to 1000° C. Such high temperatures would only be achievable without the cavity if very high concentration ratios were

used. A large part of this performance boost is due to the optical cavity being relatively more effective at reducing the large absorber emittances which occur at such high temperatures.

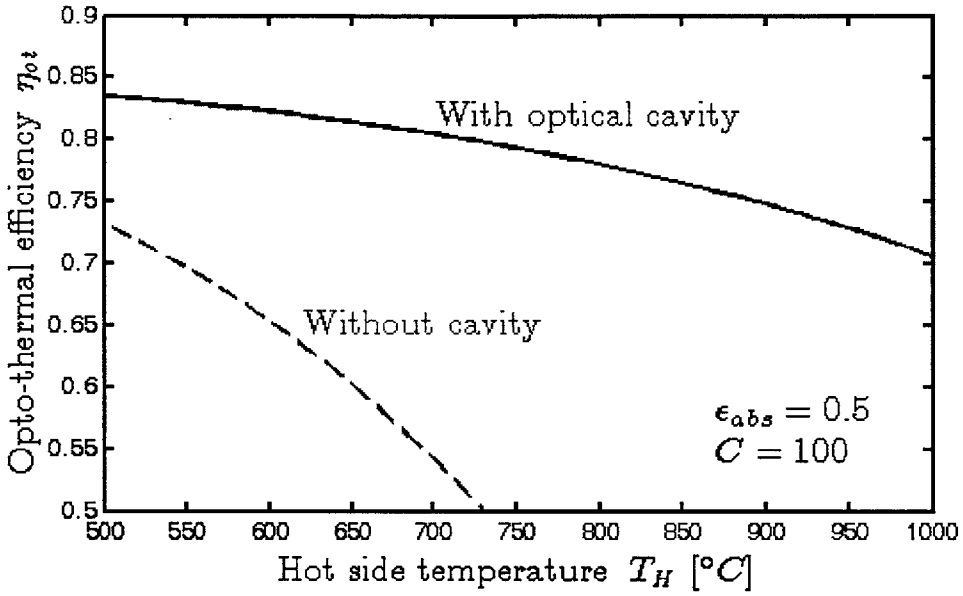

Figure 4.28 Opto-thermal efficiency as a function of hot side temperature with and without 3-D optical cavity

These results clearly show an advantage to be gained through the use of the proposed optical cavity. For both 2-D and 3-D systems, use of the optical cavity can improve opto-thermal efficiency and allow for the use of higher operating temperatures.

4.8 Summary

In this chapter, the performance of different optical cavities was investigated using primarily ray tracing simulations, as well as some analytical models. Many different factors influence cavity performance. Elliptical geometries perform better than circular/spherical geometries, however when spectrally selective absorbers are used rather than blackbody

absorbers, the benefit of elliptical geometries is small. Performance improves with increased cavity size and reflectance for all cavities. Alignment of the absorbers within the cavity is shown to be critical, in both the x-y plane and the z plane, with misalignments as small as one fifth the absorber radius resulting in significantly reduced performance.

Chapter 5 Optical Cavity Experimental Results

Results from the analytical treatment of ellipsoidal cavities (section 4.1) and ray tracing simulations of non-ideal cavities (section 4.3) show that the proposed optical cavities are successful in significantly reducing effective emittance, however this reduction is not of practical use if it cannot be demonstrated experimentally as well. This chapter reports preliminary experimental results for the performance of the optical cavity.

5.1 Experimental procedure

Measuring total hemispherical emittance directly is quite difficult, and existing methods would likely be difficult to integrate with the optical cavity system [74]. Instead, the effect of the optical cavity can be investigated by comparing relative radiative losses with and without the absorber enclosed by the cavity. The procedure used for determining the reduction in effective emittance was as follows:

1. In a vacuum chamber, attach the absorber surface to a heater. Suspend the heater such that it has minimal conduction losses to the chamber. Raise the heater temperature to some elevated temperature for which the effective emittance is of interest, and measure the power required to maintain that elevated temperature (see Fig. 5.1a).
2. Put the absorber surface within the optical cavity in the vacuum chamber, and bring the heater to the same elevated temperature. Measure the power required to maintain the elevated temperature (see Fig 5.1b).

If the heater is close to isothermal and in good thermal contact with the absorber surface, we can expect that the power from the first case P_1 and the power from the second case P_2 to be given by

$$P_1 = Q_{loss} + A_{abs}\sigma\epsilon(T_H^4 - T_{amb}^4) \tag{5.1}$$

$$P_2 = Q_{loss} + A_{abs}\sigma\epsilon^*(T_H^4 - T_{amb}^4) \tag{5.2}$$

where Q_{loss} is the heat lost from the heater by radiation from the backside and conduction losses through the mount and wires. We expect that Q_{loss} should be the same in both cases, as none of these heat loss mechanisms should be affected by the presence of the cavity. Therefore, the difference in emittances can be given by

$$\epsilon - \epsilon^* = \frac{P_1 - P_2}{A_{abs}\sigma(T_H^4 - T_{amb}^4)} \tag{5.3}$$

This experiment yields the reduction in effective emittance $\epsilon - \epsilon^*$, however the effective emittance of the absorber/cavity system can only be found if the emittance of the absorber is known. In the case that the absorber emittance is known, the effective emittance of the system is given simply by

$$\epsilon^* = \epsilon - \frac{P_1 - P_2}{A_{abs}\sigma(T_H^4 - T_{amb}^4)} \tag{5.4}$$

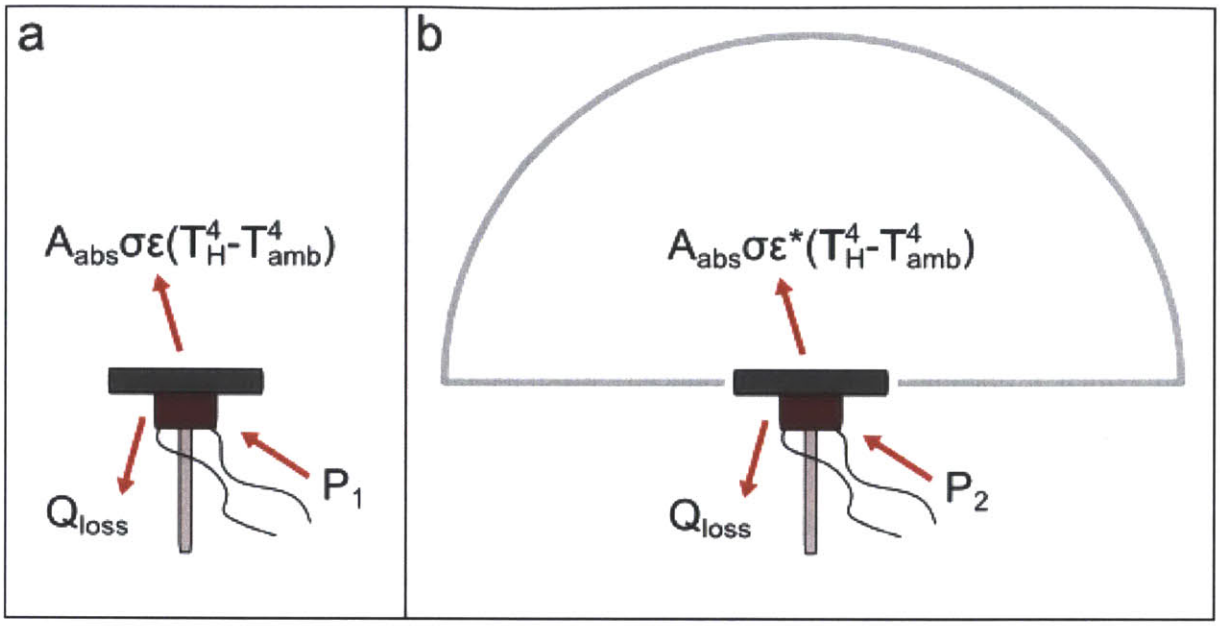

Figure 5.1 Diagram of experimental procedure: a) power input without cavity b) power input with cavity

An experimental rig was built to measure the effective emittance reduction of such an optical cavity using the method outlined above, and is shown in Fig. 5.2. Figure 5.2a shows the heater and absorber surface. The heater is mounted on a low thermal conductivity ceramic pillar in order to reduce conduction losses during operation. The pillar is attached to a two-axis linear stage for precise alignment of the center of the absorber. The absorber surface used for the experiment is high stability black paint, with emittance close to unity. While in practice a lower emittance surface would likely be used, for experimental purposes the greatest $\epsilon - \epsilon^*$ can be measured for an absorber with high emittance. Figure 5.2b shows the absorber aligned in the center of the floor of the cavity. The floor of the cavity consists of plastic sheets, with a hole for the hemispherical cavity top to couple to the floor. For later setups, the floor of the cavity will be made reflective in order to improve performance. Figure 5.2c shows the mirrored cavity, which

is a 10 cm diameter glass hemisphere, with a gold coating of greater than 200 nm thickness. While gold is not the most reflective surface for visible light, it is highly reflective in the IR spectrum, which is the relevant spectrum for the operating temperatures of the absorber. In practice the cavity would need an aperture to allow sunlight to reach the absorber, but for initial demonstration purposes, omitting the aperture allows for greater effective emittance reduction (referring back to Fig. 4.14, we would expect an effective emittance at least 0.02 greater if an aperture with a 5° opening angle was introduced). From the photo it is apparent that the surface is very smooth and highly specularly reflecting. Figure 5.2d shows the rig fully assembled, with the reflective hemispherical dome placed over the absorber.

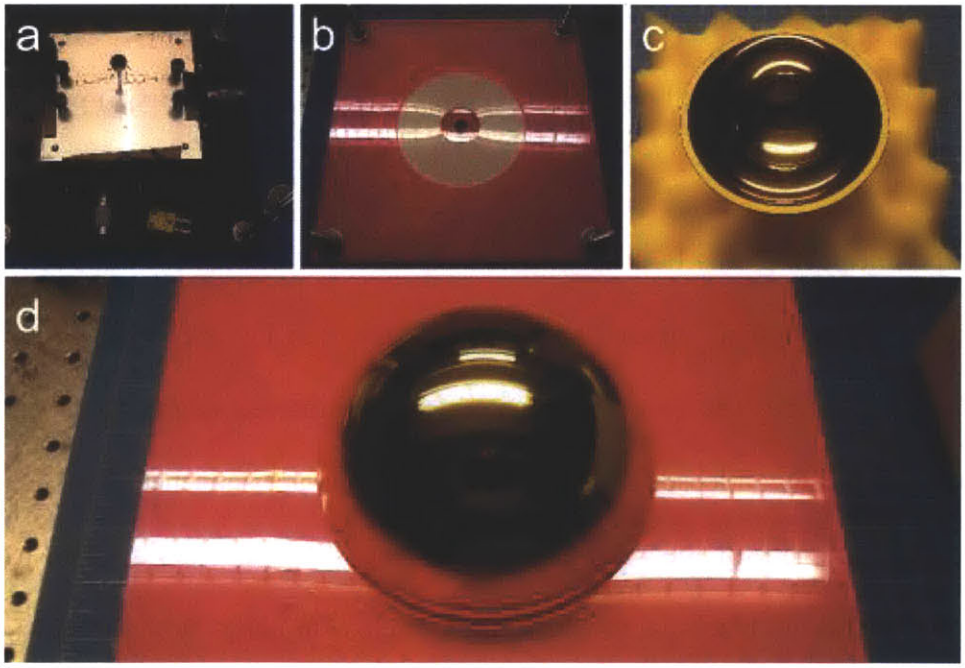

Figure 5.2 Photos of experimental rig: a) heater and absorber surface b) cavity floor c) reflective hemipsherical cavity d) fully assembled experimental rig

5.2 Preliminary results

At the point of writing, only preliminary testing has been performed using this experimental rig to measurement effective emittance reduction due to the cavity, however it should still be valuable to the reader to be able to observe the current status of the experiment. The results reported here will therefore be expanded with further work.

Figure 5.3 shows the power input required to maintain the absorber surface at elevated temperature with and without the presence of the cavity for different operating temperatures. Here only the operating temperatures of 100° C, 200° C and 300° C are used. While higher temperatures would be used in practice, because the absorber is close to black, emittance reduction should not be a function of absorber temperature. Going to higher temperatures can cause heater failure, so it is thus desirable to avoid going to high temperatures unnecessarily. The values for power input are also shown in Table 5.1 along with three standard deviation uncertainty. The high standard deviations for power input with the cavity are larger likely due to slight alignment changes for different experimental runs. While this high uncertainty is undesirable, it indicates that performance can likely be improved after more effort is applied to solving alignment issues.

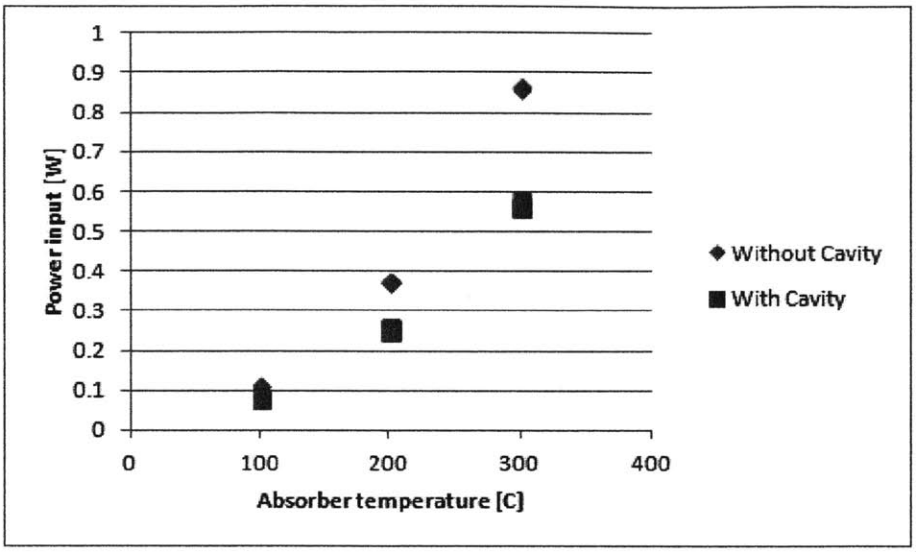

Figure 5.3 Measured power inputs to maintain absorber temperature

Table 5.1 Power inputs to maintain absorber surface temperature: +/- values for 3 standard deviation uncertainty

Temperature	Power input without cavity	Power input with cavity
100° C	0.114 +/- 0.005 W	0.081 +/- 0.007 W
200° C	0.376 +/- 0.007 W	0.253 +/- 0.010 W
300° C	0.864 +/- 0.011 W	0.567 +/- 0.022 W

Figure 5.4 shows the calculated effective emittance reduction when the values in Table 5.1 are used with Eq. (5.3) for the experimental cavity system. The error bars are for three standard deviation uncertainty. The reduction in effective emittance is in the range of 0.6 to 0.7, except for the 100° C case, which has a much larger range of uncertainty. This large uncertainty is due to a low signal to noise ratio for the lowest temperature case, as the radiative losses make up a smaller portion of total heat loss at lower temperatures. Additionally, there is large uncertainty for this experiment in general, as it involves taking a small difference of two large numbers.

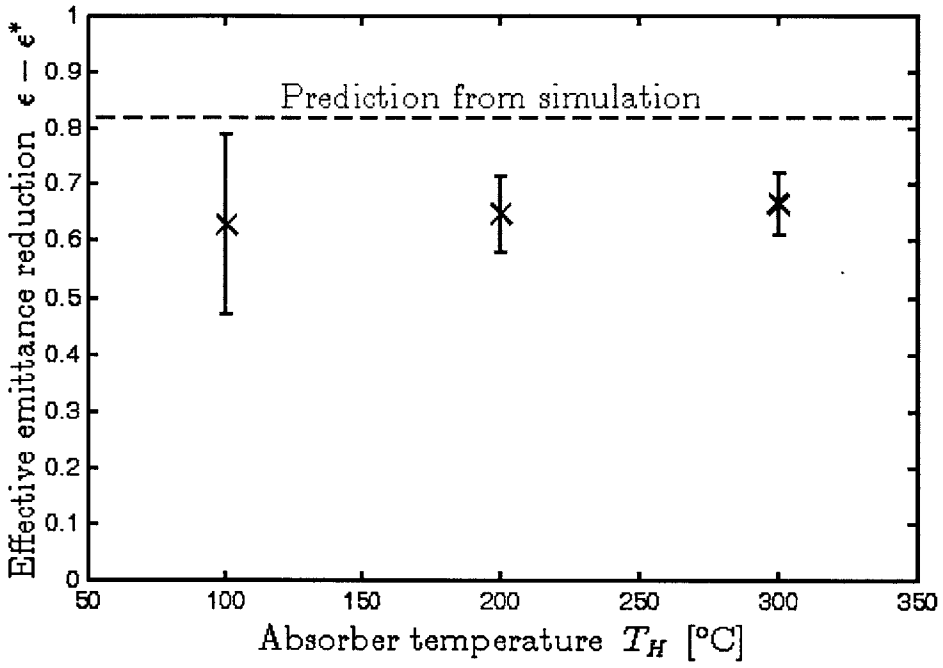

Figure 5.4 Measured effective emittance reduction with cavity: error bars represent 3 standard deviation uncertainty. Dashed red line shows predicted results from simulation

Figure 5.4 also shows the reduction in effective emittance predicted by ray tracing simulation. In this ray tracing simulation, the same cavity size ratio of $r_{cav}/r_{abs} = 10$ is used, emittance values of $\epsilon_{cav} = 0.05$ and $\epsilon_{abs} = 0.95$ are assumed, and the cavity floor is assumed to be completely absorbing (since it is plastic in the experiment). Additionally, the absorber is assumed to be positioned at the exact center of the cavity. The experimental results fall short of the prediction from simulation, which indicates that there are still issues to address regarding the construction of the cavity, including absorber alignment and cavity wall specular reflectance. While the result falls short of the predicted performance, it is still promising as it indicates that the principle of the optical cavity is successful. If the cavity at this size was modeled as a diffuse radiation shield, the emittance reduction would be essentially zero, due to the view factor from

the hemisphere to the plastic cavity floor being so much larger than the view factor from the hemisphere to the absorber.

While there is undoubtedly more experimental work to be done in terms of characterizing the cavity, this result shows a clear reduction in effective emittance of an absorber in the cavity. This reduction would be orders of magnitude lower if the reduction was happening through diffuse radiation shielding rather than the specular directional behavior which constitutes the idea behind this cavity. With more work, this cavity holds the potential to greatly decrease the effective emittance of solar absorbers in solar-thermal systems, increasing efficiency and opening up new regimes for high temperature heat cycles.

Chapter 6 Conclusion

6.1 Summary

This thesis explores two improvements to STEGs through device level modifications: thin-film STEGs and optical cavity solar receivers. Difference in performance with the thin-film STEGs primarily arise from sunlight incident on the device striking the TE legs and heat sink, which is avoided in the traditional STEG arrangement. In exploring thin-film STEG performance, two device parameters (γ and β) were found, which help guide device design regardless of device scale. Additionally, limitations for manufacturing thin film devices were considered, and their impact on device efficiency was analyzed. It has been shown that from a theoretical standpoint, thin-film STEGs can achieve performance close to traditional STEGs when considering the same material properties. This is an important result because thin-film STEGs could potentially be produced at lower cost than bulk STEGs, thus if thin-film STEGs perform with similar efficiency, their cost per watt could be lower.

An optical cavity was proposed which is designed to specularly reflect emitted radiation back to the absorber of a solar-thermal system. This is achieved by placing the absorber in the center of a circular, hemispherical, elliptical or ellipsoidal cavity with highly reflective walls. The optical cavity has been shown to reduce the effective emittance of a solar absorber through ray tracing simulations for all investigated geometries. While the elliptical and ellipsoidal geometries generally have better performance, the circular and hemispherical results are still impressive enough that pursuing those geometries should not be ruled out. Aside from geometry, cavity performance depends on cavity size, mirror reflectance, aperture size and absorber

alignment. Aperture size is an important parameter to choose carefully, as smaller apertures lower the absorber effective emittance, but can hurt overall system performance by reducing the allowable solar concentration ratio. Preliminary experimental results for the optical cavity show a reduction in effective emittance significantly greater than if the cavity was treated as a diffuse radiation shield. These results are promising, as they indicate that the optical cavities investigated could improve the performance of many solar-thermal systems.

6.2 Future work

While this thesis explores theoretical performance of the two proposed improvements to STEG design with some thoroughness, there still exists significant room for exploration of these improvements from an experimental standpoint. Thin-film STEGs have been explored experimentally, however the efficiencies achieved at this point are significantly lower than those achieved using bulk STEG materials [50]. Thin-film STEGs as proposed in this thesis have yet to be explored. It would be a large undertaking to realize the thin-film STEG design proposed here, but if implemented successfully would be a very impressive demonstration and could potentially reduce manufacturing costs of STEG systems considerably.

Preliminary experimental results for the optical cavity have been recorded and presented in this thesis, however significant experimental work remains to demonstrate the optical cavity as a commercially viable technology. More work needs to be done in order to close the gap between the theoretically predicted effective emittance reduction and the reduction observed in experiment. Additionally, once the predicted emittance reduction has been demonstrated, the cavity must be integrated into a fully functional solar-thermal conversion system. Once this is

achieved, the optical cavity has the potential to be used in many systems and make a positive impact through improving the performance of solar-thermal conversion systems worldwide.

References

[1] G.-R. Walther, E. Post, P. Convey, A. Menzel, C. Parmesan, T. J. C. Beebee, J.-M. Fromentin, O. Hoegh-Guldberg, and F. Bairlein, "Ecological responses to recent climate change," *Nature*, vol. 416, no. 6879, pp. 389–395, 2002.

[2] S. Shafiee and E. Topal, "When will fossil fuel reserves be diminished?," *Energy Policy*, vol. 37, no. 1, pp. 181–189, 2009.

[3] Eia, "Estimated Levelized Cost of New Generation Resources, 2016.," *Energy*, no. December. EIA, 2010.

[4] J. Staub, *International Energy Outlook*, vol. 0484, no. July. Citeseer, 2010, pp. 70–99.

[5] M. A. Green, *Solar cells: Operating principles, technology, and system applications*, vol. 1. University of New South Wales, 1982, p. 274.

[6] Ren, "Renewables 2012 Global Status Report," REN21 Secretariat, 2012.

[7] S. A. Kalogirou, "Solar thermal collectors and applications," *Progress in Energy and Combustion Science*, vol. 30, no. 3, pp. 231–295, 2004.

[8] A. Kribus, R. Zaibel, D. Carey, A. Segal, and J. Karni, "A solar-driven Combined Cycle plant," *Solar Energy*, vol. 62, no. 2, pp. 121–129, 1998.

[9] M. Telkes, "Solar Thermoelectric Generators," *Journal of Applied Physics*, vol. 25, no. 6, p. 765, 1954.

[10] R. Swanson, "Thermophotovoltaic converter and cell for use therein," *US Patent 4,234,352*, vol. 17, no. 1969, 1980.

[11] M. Laroche, R. Carminati, and J. J. Greffet, "Near-field thermophotovoltaic energy conversion," *Journal of Applied Physics*, vol. 100, no. 6, p. 063704, 2006.

[12] G. N. Hatsopoloulos and E. P. Gyftopoulos, *Thermionic Energy Conversion*, Vol. 2. Cambridge, Massachusetts: MIT Press, 1979.

[13] H. J. Goldsmid, *Applications of Thermoelectricity*. London: Methuen, 1960.

[14] G. Chen, *Nanoscale Energy Transport and Conversion*. New York, New York: Oxford University Press, 2005.

[15] E. WESTON, "Apparatus for Utilizing Solar Radiant Energy," *US Patent 389,124*, 1888.

[16] D. Kraemer, B. Poudel, H.-P. Feng, J. C. Caylor, B. Yu, X. Yan, Y. Ma, X. Wang, D. Wang, A. Muto, K. McEnaney, M. Chiesa, Z. Ren, and G. Chen, "High-performance flat-panel solar thermoelectric generators with high thermal concentration.," *Nature materials*, vol. 10, no. 7, pp. 532–8, Jul. 2011.

[17] K. McEnaney, D. Kraemer, Z. Ren, and G. Chen, "Modeling of concentrating solar thermoelectric generators," *Journal of Applied Physics*, vol. 110, no. 7, p. 074502, 2011.

[18] H. Goldsmid, J. Giutronich, and M. Kaila, "Solar thermoelectric generation using bismuth telluride alloys," *Solar Energy*, vol. 24, pp. 435–440, 1980.

[19] S. Omer and D. Infield, "Design optimization of thermoelectric devices for solar power generation," *Solar Energy Materials and Solar Cells*, vol. 53, pp. 67–82, 1998.

[20] R. Amatya and R. J. Ram, "Solar Thermoelectric Generator for Micropower Applications," *Journal of Electronic Materials*, vol. 39, no. 9, pp. 1735–1740, Apr. 2010.

[21] D. M. Rowe, "A high performance solar powered thermoelectric generator," *Applied Energy*, vol. 8, no. 4, pp. 269–273, Aug. 1981.

[22] P. Li, L. Cai, P. Zhai, X. Tang, Q. Zhang, and M. Niino, "Design of a Concentration Solar Thermoelectric Generator," *Journal of Electronic Materials*, vol. 39, no. 9, pp. 1522–1530, Jun. 2010.

[23] G. Chen, "Theoretical efficiency of solar thermoelectric energy generators," *Journal of Applied Physics*, vol. 109, no. 10, p. 104908, 2011.

[24] F. P. Incropera, D. P. DeWitt, T. L. Bergman, and A. S. Lavine, *Fundamentals of Heat and Mass Transfer*, vol. 6th. John Wiley & Sons, 2007, p. 997.

[25] M. Rubin, "Optical properties of soda lime silica glasses," *Solar Energy Materials*, vol. 12, no. 4, pp. 275–288, Sep. 1985.

[26] B. Yoldas, "Investigations of porous oxides as an antireflective coating for glass surfaces," *Applied Optics*, vol. 19, no. May, pp. 1425–1429, 1980.

[27] J. Hiller, J. D. Mendelsohn, and M. F. Rubner, "Reversibly erasable nanoporous anti-reflection coatings from polyelectrolyte multilayers.," *Nature materials*, vol. 1, no. 1, pp. 59–63, Sep. 2002.

[28] M. F. Modest, *Radiative Heat Transfer*, vol. 18, no. 3. Academic Press, 2003, p. 822.

[29] M. J. Blanco, J. G. Martín, and D. C. Alarcón-Padilla, "Theoretical efficiencies of angular-selective non-concentrating solar thermal systems," *Solar Energy*, vol. 76, no. 6, pp. 683–691, Jan. 2004.

[30] V. Badescu, "Spectrally and angularly selective photothermal and photovoltaic converters under one-sun illumination," *Journal of Physics D: Applied Physics*, vol. 38, no. 13, pp. 2166–2172, Jul. 2005.

[31] K. McEnaney, "Modeling of Solar Thermal Selective Surfaces and Thermoelectric Generators," Massachusetts Institute of Technology, 2010.

[32] J. FAN, "Wavelength-selective surfaces," *Adv. in Chem*, 1977.

[33] C. G. Granqvist, *Spectrally Selective Surfaces for Heating and Cooling Applications*. Bellingham, Washington: SPIE, 1989.

[34] B. Poudel, Q. Hao, Y. Ma, Y. Lan, A. Minnich, B. Yu, X. Yan, D. Wang, A. Muto, D. Vashaee, X. Chen, J. Liu, M. S. Dresselhaus, G. Chen, and Z. Ren, "High-thermoelectric performance of nanostructured bismuth antimony telluride bulk alloys.," *Science*, vol. 320, no. 5876, pp. 634–638, 2008.

[35] R. Venkatasubramanian, E. Siivola, T. Colpitts, and B. O'Quinn, "Thin-film thermoelectric devices with high room-temperature figures of merit.," *Nature*, vol. 413, no. 6856, pp. 597–602, Oct. 2001.

[36] G. J. Snyder and E. S. Toberer, "Complex thermoelectric materials.," *Nature materials*, vol. 7, no. 2, pp. 105–14, Feb. 2008.

[37] D. J. Bergman and L. G. Fel, *Enhancement of thermoelectric power factor in composite thermoelectrics*, vol. 85, no. 12. IEEE, 1999, p. 8205.

[38] D. Vashaee and A. Shakouri, "Improved thermoelectric power factor in metal-based superlattices.," *Physical Review Letters*, vol. 92, no. 10, p. 106103, 2004.

[39] D. M. Rowe and V. S. Shukla, "The Effect of Phonon-Grain Boundary Scattering on the Lattice Thermal-Conductivity and Thermoelectric Conversion Efficiency of Heavily Doped Fine-Grained, Hot-Pressed Silicon Germanium Alloy," *Journal of Applied Physics*, vol. 52, no. 12, pp. 7421–7426, 1981.

[40] K. Biswas, J. He, I. D. Blum, C.-I. Wu, T. P. Hogan, D. N. Seidman, V. P. Dravid, and M. G. Kanatzidis, "High-performance bulk thermoelectrics with all-scale hierarchical architectures.," *Nature*, vol. 489, no. 7416, pp. 414–8, 2012.

[41] D. Kraemer, K. McEnaney, M. Chiesa, and G. Chen, "Modeling and optimization of solar thermoelectric generators for terrestrial applications," *Solar Energy*, vol. 86, no. 5, pp. 1338–1350, May 2012.

[42] H. Boettner, G. Chen, and R. Venkatasubramanian, "Aspects of thin-film superlattice thermoelectric materials, devices, and applications," *MRS bulletin*, vol. 31, no. March, pp. 211–217, 2006.

[43] J. Tang, H.-T. Wang, D. H. Lee, M. Fardy, Z. Huo, T. P. Russell, and P. Yang, "Holey silicon as an efficient thermoelectric material.," *Nano letters*, vol. 10, no. 10, pp. 4279–83, Oct. 2010.

[44] F. Volklein, M. Blumers, and L. Schmitt, "Thermoelectric microsensors and microactuators (MEMS) fabricated by thin film technology and micromachining," ... *International Conference on*, no. 1 999, 1999.

[45] J. Nurnus, H. Bottner, and C. Kunzel, "Thin film based thermoelectric energy conversion systems," ... . *Proceedings ICT'02* ... , pp. 523–527, 2002.

[46] M. a. Green, "Thin-film solar cells: review of materials, technologies and commercial status," *Journal of Materials Science: Materials in Electronics*, vol. 18, no. S1, pp. 15–19, Apr. 2007.

[47] R. Yang and G. Chen, "Multistage thermoelectric microcoolers," *Journal of Applied Physics*, vol. 95, no. 12, p. 8226, 2004.

[48] G. Min and D. M. Rowe, "Cooling performance of integrated thermoelectric microcooler," *Solid-State Electronics*, vol. 43, no. 5, pp. 923–929, May 1999.

[49] G. J. Snyder, J. R. Lim, C.-K. Huang, and J.-P. Fleurial, "Thermoelectric microdevice fabricated by a MEMS-like electrochemical process.," *Nature materials*, vol. 2, no. 8, pp. 528–31, Aug. 2003.

[50] M. Mizoshiri, M. Mikami, K. Ozaki, and K. Kobayashi, "Thin-Film Thermoelectric Modules for Power Generation Using Focused Solar Light," *Journal of Electronic Materials*, vol. 41, no. 6, pp. 1713–1719, Apr. 2012.

[51] Astm G, "Standard Tables for Reference Solar Spectral Irradiances: Direct Normal and Hemispherical on 37° Tilted Surface," *2ASTM*, vol. G173–03E1, no. ASTM G173–03. ASTM International, p. DOI: 10.1520/G0173–03R08 www.astm.org, 2003.

[52] W.-S. Liu, Q. Zhang, Y. Lan, S. Chen, X. Yan, Q. Zhang, H. Wang, D. Wang, G. Chen, and Z. Ren, "Thermoelectric Property Studies on Cu-Doped n-type CuxBi2Te2.7Se0.3 Nanocomposites," *Advanced Energy Materials*, vol. 1, no. 4, pp. 577–587, Jul. 2011.

[53] X. Tang, W. Xie, H. Li, W. Zhao, Q. Zhang, and M. Niino, "Preparation and thermoelectric transport properties of high-performance p-type Bi[sub 2]Te[sub 3] with layered nanostructure," *Applied Physics Letters*, vol. 90, no. 1, p. 012102, 2007.

[54] J. J. O'Gallagher, *Nonimaging Optics in Solar Energy*, vol. 2, no. 1. 2008, pp. 1–120.

[55] R. B. Wehrspohn and J. Üpping, "3D photonic crystals for photon management in solar cells," *Journal of Optics*, vol. 14, no. 2, p. 024003, Feb. 2012.

[56] J. G. Mutitu, A. Barnett, and D. W. Prather, "Angular Selective Light Filter Based on Photonic Crystals for Photovoltaic Applications," *IEEE Photonics Journal*, vol. 2, no. 3, pp. 490–499, Jun. 2010.

[57] M. Peters, J. C. Goldschmidt, T. Kirchartz, and B. Bläsi, "The photonic light trap—Improved light trapping in solar cells by angularly selective filters," *Solar Energy Materials and Solar Cells*, vol. 93, no. 10, pp. 1721–1727, Oct. 2009.

[58] C. Schuler, C. Wolff, K. Busch, and M. Florescu, "Thermal emission from finite photonic crystals," *Applied Physics Letters*, vol. 95, no. 24, p. 241103, 2010.

[59] M. Florescu, H. Lee, A. Stimpson, and J. Dowling, "Thermal emission and absorption of radiation in finite inverted-opal photonic crystals," *Physical Review A*, vol. 72, no. 3, p. 033821, Sep. 2005.

[60] J. Harris and T. Lenz, "Thermal performance of solar concentrator/cavity receiver systems," *Solar energy*, vol. 34, no. 2, pp. 135–142, 1985.

[61] a. Steinfeld and M. Schubnell, "Optimum aperture size and operating temperature of a solar cavity-receiver," *Solar Energy*, vol. 50, no. 1, pp. 19–25, Jan. 1993.

[62] M. Prakash, S. B. Kedare, and J. K. Nayak, "Investigations on heat losses from a solar cavity receiver," *Solar Energy*, vol. 83, no. 2, pp. 157–170, Feb. 2009.

[63] B. Ebihara, "Thermal radiation shielding," *US Patent 3,409,730*, pp. 5–7, 1968.

[64] J. Howell, "The Monte Carlo method in radiative heat transfer," ... *Of Mechanical Engineers Journal Of Heat Transfer*, vol. 120, no. August, 1998.

[65] F. L. Pedrotti, L. M. Pedrotti, and L. S. Pedrotti, *Introduction to Optics*, 3rd Editio. Boston: Addison-Wesley, 2006.

[66] H. C. Hottel, "Radiant heat transmission," *Heat Transmission*, vol. 3, 1954.

[67] A. S. Glassner, *Introduction to Ray Tracing*. Academic Press, 1989, p. 327.

[68] J. E. Freund and B. M. Perles, *Modern Elementary Statistics*, 12th Editi. Pearson, 2006.

[69] H. DeLorenzi and H. Nied, "Blow molding and thermoforming of plastics: finite element modeling," *Computers & Structures*, 1987.

[70] R. Winston, J. C. Minano, P. G. Benitez, N. Shatz, and J. C. Bortz, *Nonimaging Optics*. Burlington, MA: Elsevier Academic Press, 2005.

[71] A. Rabl, "Comparison of solar concentrators," *Solar Energy*, vol. 18, no. 2, pp. 93–111, Jan. 1976.

[72] F. L. Pedrotti, L. M. Pedrotti, and L. S. Pedrotti, *Introduction to Optics*, 3rd Editio. Boston: Addison-Wesley, 2006.

[73] W. T. Xie, Y. J. Dai, R. Z. Wang, and K. Sumathy, "Concentrated solar energy applications using Fresnel lenses: A review," *Renewable and Sustainable Energy Reviews*, vol. 15, no. 6, pp. 2588–2606, Aug. 2011.

[74] J. Palmer, "The measurement of transmission, absorption, emission, and reflection," *Handbook of optics*, pp. 1–25, 1995.